Spectroscopic Studies of Atmospheric Relevant Air-Aqueous and Air-Silica Interfaces

DISSERTATION

Presented in Partial Fulfillment of the Requirements for the Degree Doctor of Philosophy
in the Graduate School of The Ohio State University

By

Nadia Ninel Casillas Ituarte, M. Sc.

Graduate Program in Environmental Science

The Ohio State University

2010

Dissertation Committee:

Heather C. Allen, Advisor

Linda Weavers

Steven Lower

W. Berry Lyons

Copyright by

Nadia Ninel Casillas Ituarte

2010

Abstract

Great challenges exist in understanding how aerosols impact the chemistry of the atmosphere, mainly because of their complex chemical composition and their constant physical and chemical modification as they transit in the atmosphere. Marine aerosols and mineral oxides particles are the most abundant naturally emitted aerosols. In marine aerosols, Mg^{2+} and Cl^{-} play an active role in atmospheric chemistry, particularly in coastal urban regions. The study of the interactions of these ions with water molecules at the aqueous surface was conducted to help elucidate the role of inorganic cations and anions in atmospheric processes. In the case of mineral particles, not only do they affect atmospheric chemistry but they also have been related to human respiratory problems. Crystalline and amorphous SiO_2 particles are some of the most notoriously toxic particles in pulmonary diseases. In an attempt to elucidate the molecular effect of the adhesion of silica particles to cell membranes, the surface organization of dipalmitoylphosphatidylcholine (DPPC), as a model of biological membranes, at the air-water and the air-silica surfaces was examined. Additionally, the adsorption of gas-phase species onto the surface of solid and liquid particles is a common process in the atmosphere. As models of these phenomena, interfacial water vapor uptake by amorphous silica after the exposure to mid RH values and adsorption of gas-phase alkyl halides and alcohols to the air-water interface were examined.

Sum frequency generation (SFG), a surface specific technique that provides molecular level interfacial information, was employed as the main technique to investigate the interfaces and surfaces of the systems discussed in this dissertation. Complementary vibrational Raman and infrared spectroscopies were also used.

Aqueous solvation of Mg^{2+} as a function of $MgCl_2$ concentration in the bulk was investigated with Raman spectroscopy. The analysis of the $Mg—O_{water}$ hexaaquo stretch supports the absence of ion pairing in $MgCl_2$ through at least 0.06x (mole fraction). At a higher concentration, a change in the hydration environment of Mg^{2+} is observed and assigned to an increased number of solvent-share ion pairs. No contact ion pairs are clearly observed in aqueous solutions of $MgCl_2$. At the air-aqueous interface, the disturbance of the hydrogen bonding environment is dependent on the $MgCl_2$ concentration. At concentration lower than < 1 M minor changes are observed. At concentrations above 1 M the hydrogen bonding environment is highly perturbed. The 2.1 M intermediate concentration solution shows the largest SFG response relative to the other solutions including concentrations as high as 4.7 M. The enhancement of SFG signal observed for the 2.1 M solution is attributed to a larger SFG-active interfacial region and more strongly oriented water molecules relative to other concentrations. SFG studies of the dangling OH of the surface water reveal that the topmost water layer is affected structurally at high concentrations (> 3.1 M).

Interfacial studies of aqueous solutions of NaCl and a model seawater solution (composed of NaCl and $MgCl_2$) were also explored. The interfacial hydrogen bonding environment of the model seawater is highly perturbed. The presence of $MgCl_2$ in this model solution has a strong effect on water structure and on its electrostatic environment.

In a study related to solid-phase aerosols, the air-silica interface, before and after adsorption of water in the gas phase and in the liquid phase, was examined. Free silanol OH groups are observed after 72 h of exposure to mid RH conditions. The free silanol average orientation determined is $26 \pm 2°$ from the surface normal.

In order to study the interaction of mineral aerosols with cell membranes, interfacial hydration and orientation of the phosphate group of DPPC monolayers in the presence of sodium ions and calcium ions at air–aqueous and air-silica interfaces were investigated. Sodium ions affect the phosphate hydration subtly, while calcium ions cause a marked dehydration. Silica-supported DPPC monolayers reveal similar hydration behavior relative to that observed in the corresponding liquid subphase for the case of water and in the presence of sodium ions. However, in the presence of calcium ions the phosphate group dehydration is greater than that from the corresponding liquid subphase. The calculated average tilt angles from the surface normal of the PO_2^- group of DPPC monolayers on the water surface and on the silica substrate are found to be $63° \pm 3°$ and $74° \pm 3°$, respectively. The hydration environment and orientation of the phosphate moiety of DPPC monolayers are affected considerably at the silica surface compared to that with the aqueous subphase.

Finally, the adsorption of gas-phase alkyl halides and alcohols to the air-water interface was studied as a model of gas-phase uptake by liquid aerosols. Methanol and butanol are adsorbed into the aqueous solution as revealed by surface (SFG) and bulk (Raman) spectroscopies. Alkyl halides are not detected at the air-water interface, although methyl chloride is readily observed in the bulk. Orientation (disordered molecules) and low number density have been invoked to explain the absence of the methyl chloride signal in the SFG spectrum.

Dedication

To my family

Acknowledgments

All the work presented in this dissertation would not have been possible without the help of many people. To all them I want to express my gratitude. I especially thank my advisor, Prof. Heather C. Allen for her continuous support and guidance during this journey. During my graduate study, not only have I learned chemistry from her, but also how to become a researcher. Also I want to thank all of the Allen lab members, past and present, particularly Dr. Gang Ma, Dr. Lisa Van Loon, and Xiangke Chen who were a great source of help and support. I wish to thank my longtime friend and partner in crime Roxana Sierra for her continuous support and friendship inside and outside the lab. Also, during the last years of this journey, my husband Paul has been a continuous source of love and support, thank you.

Finally, I want to thank my parents for the education, support and love I have received from them. To them, I give my deepest gratitude.

Vita

April 1978	Born – Delicias Chih., Mexico
2000	B.S. Bacteriologist Parasitologist Chemist, Autonomous University of Chihuahua, Mexico
2005	M.Sc. Environmental Science, The Ohio State University
2005 to 2010	Graduate Teaching Associate, Department of Chemistry, The Ohio State University
2005 to 2010	Graduate Research Associate, Department of Chemistry, The Ohio State University

Publications

I. Nadia N. Casillas-Ituarte, Heather C. Allen. Water, chloroform, acetonitrile, and atrazine adsorption to the amorphous silica surface studied by vibrational sum frequency generation spectroscopy. Chemical Physics Letters, 2009, 483, 84-89.

II. Heather C. Allen, Nadia N. Casillas-Ituarte, M. Roxana Sierra-Hernández, Xiangke Chen, Cheng Y. Tang. Shedding light on water structure at air–aqueous interfaces: ions, lipids, and hydration. Physical Chemistry Chemical Physics, 2009, 11, 5538-5549.

III. Kandice Harper, Babak Minofar, M. Roxana Sierra-Hernandez, Nadia N. Casillas-Ituarte, Martina Roeselova, Heather C. Allen. Surface residence and uptake of methyl chloride and methyl alcohol at the air/water interface studied by vibrational sum frequency spectroscopy and molecular dynamics. Journal of Physical Chemistry A, 2009, 113 (10), 2015-2024.

Fields of Study

Major Field: Environmental Science

Table of Contents

List of Tables

List of Figures

List of Abbreviations

ATR	attenuated total reflection
A.U.	arbitrary units
CCD	charge-coupled device
ºC	degrees Celsius
cm^{-1}	wavenumber
DPPC	Dipalmitoylphosphatidylcholine
FTIR	Fourier transform infrared
FWHM	full width at half maximum
IR	infrared
fs	femtosecond
M	moles per liter
MD	molecular dynamics
μ m	micrometer
nm	nanometer
ps	picosecond
QE	Quantum efficiency
RH	relative humidity
SFG	sum frequency generation
Vis	visible

Chapter 1

Introduction

This dissertation encompasses interfacial studies of water and amorphous silica in the presence of ions and lipids. The main motivation behind the work presented here is to contribute to a better understanding of surface organization of water in the presence of magnesium, and the surface complexation of cations and lipids at the air-water and the air-silica interfaces.

The study of the interactions between inorganic salts and water molecules that occur during ion solvation is fundamental to understanding the role of ions in biological, geological, and environmental processes, in particular, in atmospheric aerosol processes.[1] The role played by atmospheric aerosol in environmental issues includes climate change, stratospheric ozone depletion and tropospheric air pollution. [2, 3]

Aerosols are ubiquitous in the troposphere, and thus represent an important component of the Earth's atmosphere. They represent the largest uncertainty in understanding how humans are changing the climate. [4] Because aerosols are composed of solid and liquid particles of varying chemical composition, size, and phase, great challenges exist in understanding how they impact the chemistry of the atmosphere. Primary aerosols are emitted by combustion sources (e.g. volcanic eruptions, biomass burning, and vehicle emissions) or by wind-driven processes such as the resuspension of marine particles and mineral dust. These wind-generated aerosols are the most abundant natural aerosols. [5]

Secondary particles are formed from photochemical reaction of gas-phase species emitted directly in to the atmosphere, producing more highly oxidized species which can form a new particle or condensed on exiting particles surfaces. [4]

The most abundant cations in seawater are sodium and magnesium, while chloride is the most prevalent anion. [6] Marine aerosols may undergo water evaporation as they transit in the atmosphere and thus an increased ion concentration is found. Experimental and theoretical studies have reported that aqueous surfaces of halide salt solutions are ion enriched, meaning the concentration of ions at the surface is greater than in the bulk. [7-24] These findings have atmospheric relevance particularly in the case of chloride. It has been reported that chloride ions participate in heterogeneous reactions to form chlorine gas in the atmosphere. [25] This gas is known to be photolized to produce chlorine radical that are involved in ozone depletion events. [26] In polluted areas, it reacts predominantly with alkanes and NO, resulting in ozone formation. [26, 27] The surface availability of chloride ions, and thus its readability to participate in heterogeneous reactions could be affected by the cation ability to form contact ion pairs (direct contact between the anion and cation) during ion solvation. The ability of magnesium to ion pair with chloride in aqueous $MgCl_2$ solutions as a function of concentration is discussed in Chapter 3. Interfacial water organization of aqueous $MgCl_2$ solutions and an aqueous model seawater solution composed of a mixture of NaCl and $MgCl_2$ are examined in Chapter 4 and Chapter 5, respectively. Experimental details can be found in Chapter 2 and subsequent chapters.

Mineral oxide particles can impact a number of global processes including Earth's climate through direct and indirect climate forcing. [28]. A direct effect of these oxide particles is observed when they scatter and absorb radiation [29], while and an indirect effect is present when they act as cloud condensation nuclei .[30] Additionally, these mineral particles can undergo heterogeneous reactions while in transit through the atmosphere, altering the physicochemical properties of the mineral dust aerosol itself. Some of these mineral particles surfaces act as sinks for gas-phase species, e.g gas phase adsorption of NO_2 *(g)* on hydrate silica particles to form HNO_3*(l)* has been reported. [31] The mineralogical composition of soils on the Earth's surface and therefore in the atmosphere is quite diverse. From the silt fraction (particles with 2-50 μm in diameter), quartz (SiO_2) is in average the most abundant mineral [32], although significant amounts are found in the clay fraction (particles with < 2 μm in diameter). [32] In Chapter 6, the surface hydroxylation of amorphous silica exposed to mid relative humidity values is discussed.

The scientific community's attention has also been brought to the study of mineral dust particles due to the health problems related to their exposure. [33] One of the most notorious toxic particles in pulmonary diseases is SiO_2 in its crystalline and amorphous forms. [33] The mechanism by which cell membranes in the human lungs degenerate upon adhesion to silica particles is not well understood. [34] The use of dipalmitoylphosphatidylcholine (DPPC) as a model of biological membranes is well documented. [35-39] Interfacial complexation of cations and the phosphate of DPPC monolayers i) spread on water and ii) supported on silica are discussed in Chapter 7.

As described above, aerosols can vary their chemical compositions as they transit in the atmosphere. One common mechanism is the uptake of gas-phase species into liquid aerosols. In Chapter 8, the adsorption of gas-phase alkyl halides and alcohols in liquid water is investigated. Finally in Chapter 9, the atmospheric implications of the results obtained from the studies described in this dissertation are asserted.

Chapter 2

Experimental Methods

In this Chapter, the theory and instrumentation details of sum frequency generation (SFG) spectroscopy used to characterize aqueous and silica interfaces are described. In addition, instrumentation details of Raman and infrared spectroscopies, which provide bulk vibrational information, are provided here.

2.1 Sum Frequency Generation

2.1.1.Theory

Since the first experimental demonstration of surface vibrational spectroscopy via sum frequency generation (SFG) conducted in 1987[40], SFG spectroscopy has become a highly versatile spectroscopic technique to study the structures of different kinds of surfaces and interfaces. [7, 23, 41-45] Detailed theoretical principles of the sum frequency process can be found elsewhere. [46, 47] Only a brief description of this process is presented here.

Being a second-order nonlinear process, SFG is forbidden under the electric dipole approximation in a medium with inversion symmetry, where molecules experience a centrosymmetric environment, but is allowed at a surface or interface where the inversion symmetry is broken namely in noncentrosymmetric environments. Also SFG is an optical technique involving photons, thus the study of liquid samples is possible. Solid and liquid samples can also be analyzed under a wide range of pressures including atmospheric.

Experimentally, when two laser beams, one visible beam (e.g. λ_{Vis}= 532 nm) and an infrared beam (e.g. λ_{IR} = 3000 nm), are overlapped in time and space at an interface and such that the energies and momenta (phase matching) of the incoming and outgoing photons are conserved, vibrational SFG photons are generated at a visible frequency (λ_{SFG}= 452 nm) as shown in Figure 2.1. SFG has been described as the coherent process of vibrational exciting surface molecules, and simultaneously exciting an anti-Stokes Raman scattering process from this infrared excited surface as shown in the energy diagram of Figure 2.2. The energy and momentum conservation (phase-matching condition) of the photons involved in the SFG process are shown in the relations:

$$n_{SF} k_{SF} \sin\theta_{SF} = n_{Vis} k_{Vis} \sin\theta_{Vis} \pm n_{IR} k_{IR} \sin\theta_{IR} \qquad (2.1)$$

In equation 2.1, *n* is the index of refraction of the medium through which the indicated beam travels, *k* is the wave vector of the beam and is equal to *ω/c (ω* is the frequency and *c* is the speed of light in vacuum), and *θ* is the angle of the beam to the surface normal. The sign between the two terms of the right side of equation 2.1 depends on the geometry of the SFG system, the sign is positive for experimental geometries with a co-propagating visible and infrared beam (e.g. Figure 2.1), and negative in case of counter-propagating geometries.

Under the irradiation of two optical fields $\mathbf{E_1}$ and $\mathbf{E_2}$ with frequencies ω_{Vis} and ω_{IR}, respectively, a second order polarization $\boldsymbol{P}^{(2)}(\omega_{SFG} = \omega_{Vis} + \omega_{IR})$ is generated in the interfacial layer as shown in equation 2.2

$$P^{(2)}(\omega_{SFG} = \omega_{Vis} + \omega_{IR}) = \chi^{(2)}_{eff}(\omega_{SFG} = \omega_{Vis} + \omega_{IR}) : E_1(\omega_{Vis}) E_2(\omega_{IR}) \qquad (2.2)$$

where $\chi_{eff}^{(2)}(\omega_{SFG}=\omega_{Vis}+\omega_{IR})$ is the effective second order nonlinear susceptibility tensor of the interface. For IR-visible SFG, ω_{Vis} is in the visible range and ω_{IR} in the IR range. The nonlinear polarization generated in media 1 and 2 must vanish due to inversion symmetry under the electric dipole approximation. The sum frequency intensity in the reflected direction is given by

$$I_{SFG}=\frac{8\pi^3\omega_{SFG}^2\sec^2\beta}{c^3 n_1(\omega_{SFG})n_1(\omega_{Vis})n_1(\omega_{IR})}\left|\chi_{eff}^{(2)}\right|^2 I(\omega_{Vis})I\omega_{IR}) \qquad (2.3)$$

In equation 2.3, n is the refractive index of medium 1 at frequency ω, β is the reflection angle of the sum frequency field, $I(\omega_{Vis})I\omega_{IR})$ are the intensities of the two input fields. The effective nonlinear susceptibility $\chi_{eff}^{(2)}$ takes the form of

$$\chi_{eff}^{(2)}=\left[\hat{e}(\omega_{SFG})\cdot L(\omega_{SFG})\right]\cdot\chi^{(2)}:\left[L(\omega_{Vis})\cdot\hat{e}(\omega_{Vis})\right]\left[L(\omega_{IR})\cdot\hat{e}(\omega_{IR})\right] \qquad (2.4)$$

With $\hat{e}(\omega)$ being the unit polarization vector and $L(\omega)$ the Fresnel factor at frequency ω.

In the case of azimuthally isotropic interface, there are only four independent nonvanishing components of $\chi^{(2)}$. With the lab coordinates chosen such that *z* is along the interface normal and *x* in the incident plane as shown in Figure 2.1, they are $\chi_{xxz}=\chi_{yyz}$, $\chi_{xzx}=\chi_{yzy}$, $\chi_{zxx}=\chi_{zyy}$ and χ_{zzz}. These four components can be deducted by measuring SFG with four different input and output polarization combinations, namely, ssp, (where the sum frequency, visible, and the infrared beams are *s*-polarized, *s*-polarized, and *p*-polarized, respectively), sps, pss, and ppp. The effective nonlinear susceptibilities under these four polarization combinations can be expressed as

$$\chi_{eff}^{(2)},ssp = L_{yy}(\omega_{SFG})L_{yy}(\omega_{Vis})L_{zz}(\omega_{IR})\sin\beta_{IR}\chi_{yyz} \tag{2.5a}$$

$$\chi_{eff}^{(2)},sps = L_{yy}(\omega_{SFG})L_{zz}(\omega_{Vis})L_{yy}(\omega_{IR})\sin\beta_{Vis}\chi_{yzy} \tag{2.5b}$$

$$\chi_{eff}^{(2)},pss = L_{zz}(\omega_{SFG})L_{yy}(\omega_{Vis})L_{yy}(\omega_{IR})\sin\beta_{SFG}\chi_{zyy} \tag{2.5c}$$

$$\begin{aligned}\chi_{eff}^{(2)},ppp = &-L_{xx}(\omega_{SFG})L_{xx}(\omega_{Vis})L_{zz}(\omega_{IR})\cos\beta_{SFG}\cos\beta_{Vis}\sin\beta_{IR}\chi_{xxz}\\ &-L_{xx}(\omega_{SFG})L_{zz}(\omega_{Vis})L_{xx}(\omega_{IR})\cos\beta_{SFG}\sin\beta_{Vis}\cos\beta_{IR}\chi_{xzx}\\ &+L_{zz}(\omega_{SFG})L_{xx}(\omega_{Vis})L_{xx}(\omega_{IR})\sin\beta_{SFG}\cos\beta_{Vis}\cos\beta_{IR}\chi_{zxx}\\ &+L_{zz}(\omega_{SFG})L_{zz}(\omega_{Vis})L_{zz}(\omega_{IR})\sin\beta_{SFG}\sin\beta_{Vis}\sin\beta_{IR}\chi_{zzz}\end{aligned} \tag{2.5d}$$

where $L_{xx}(\omega)$, $L_{yy}(\omega)$ and $L_{zz}(\omega)$ are the Fresnel factors at frequency ω, and $\beta\ (\omega)$ are the incident angles of the optical fields.

The intensity of the sum frequency radiation emitted from an interface may be also described in terms of the contributing resonant and nonresonant components. In equation 2.6 it is shown that the macroscopic second order nonlinear susceptibility, $\chi^{(2)}$, is comprised of a nonresonant term $\chi_{NR}^{(2)}$ and a sum of resonant terms $\chi_{\nu}^{(2)}$

$$I_{SFG} \propto \left|\chi^{(2)}\right|^2 \propto \left|\chi_{NR}^{(2)} + \sum_{\nu}\chi_{\nu}^{(2)}\right|^2 \tag{2.6}$$

$\chi_{\nu}^{(2)}$ of a single resonant component is described by

$$\chi_{\nu}^{(2)} \propto \frac{A_{\nu}}{\omega_{\nu} - \omega_{IR} - i\Gamma_{\nu}} \tag{2.7}$$

in which A_v, is the amplitude of the SFG transition moment of the v vibrational mode and includes both the Raman and infrared transition moments of the vibration, ω_v is the frequency of the transition, and Γ_v represents the natural line width of the transition. When the frequency of the incident infrared radiation ω_{IR}, is resonant with the a vibrational mode ω_v of an interfacial molecule, the ω_v- ω_{IR} term approaches zero and the value of the $\chi^{(2)}$ increases, resulting in an intensity increase of the SFG signal as shown in equation 2.6.

Being a third-rank tensor with 27 individual elements, $\chi^{(2)}$ can be denoted as $\chi^{(2)}_{IJK,v}$, where I, J, K represent Cartesian coordinates in the laboratory reference frame. $\chi^{(2)}_{IJK,v}$ is related to the number density of the interfacial molecules N_s and to the molecular hyperpolarizability $\beta_{IJK,v}$ as shown below

$$\chi^{(2)}_{IJK,v} = N_s \left\langle \beta^{(2)}_{IJK,v} \right\rangle \tag{2.8}$$

where $\langle\ \rangle$ represents an average over the orientational distribution of the molecules. To convert the laboratory reference frame (denoted by the subscripts J, K, and L) to the molecular reference frame (denoted by the subscripts l, m, and n) an Euler angle transformation is conducted and represented by the following equation

$$\beta_{IJK,v} = \sum_{lmn} \mu_{IJK:lmn} \beta_{lmn,v} \tag{2.9}$$

The molecular hyperpolarizability $\beta_{IJK,\nu}$ explicitly demonstrates the selection rules for the sum frequency process as shown below

$$\beta_{lmn,\nu} = \langle g|\alpha_{lm}|\nu\rangle\langle\nu|\mu_n|g\rangle \qquad (2.10)$$

where $\langle g|\alpha_{lm}|\nu\rangle$ represents the Raman tensor for the transition, and $\langle\nu|\mu_n|g\rangle$ describes the IR transition moment, *g* refers to the ground vibrational state and *v* refers to the excited vibrational state. The molecular hyperpolarizability is nonzero only when the Raman and infrared transition moments are nonzero. Thus, a vibrational mode must be both Raman and infrared active in order for the vibration to be sum frequency active.

2.1.2. Instrumentation

Two different SFG spectrometers were used to examine the interfacial region of the samples analyzed in this dissertation, a scanning and a broad bandwidth SFG spectrometers. The main difference between these two SFG systems is the bandwidth of the infrared beam. In the scanning SFG system, a spectrally narrow infrared beam is scanned over a spectral range to generate a spectrum, while in the broadband SFG a single infrared pulse is sufficient to cover a spectral region. More details of both SFG systems are provided below.

In the scanning SFG system (Figure 2.3), a 1064 nm beam from solid state Nd:YAG laser system with 29 ps pulse duration and 10 Hz repetition rate (ESKPLA, PL 2143A/SS) pumps a KTP-KTA based optical parametric generator/amplifier (OPG/OPA, LaserVision) to generate the visible and infrared laser beams. The 532 nm visible beam with an energy of ~550 μJ/pulse is generated by doubling the frequency (second harmonic) of the 1064 nm pump beam. The mid-infrared beam generated is tunable from 2500 cm^{-1} to 4000 cm^{-1} with a bandwidth of 4-8 cm^{-1} and energy of 200-500 μJ/pulse, depending on the spectral region. The input angles are set to 45° and 53° from the surface normal for the 532 nm and infrared beams, respectively. The scattered 532 nm beam in the detection pathway of the SFG beam is removed with an iris, a Schott glass filter (BG25, 2 mm thickness, CVI Laser) followed by a short pass filter (SPF500, CVI Laser) and two holographic notch plus filters (Kaiser Optical System, Inc). The SFG beam is collected in a back illuminated and thermoelectrically cooled EMCCD camera with QE>90% at 600nm(Andor Technology, DV887ECS-BV) with a 512 x 512 pixel array, 16 μm^2 square pixel size. The CCD temperature was set at -80°C during the experiments. The incoming infrared beam is calibrated with a polystyrene thin film placed in the infrared beam pathway. The resulting infrared energy is measured as a function of wavenumbers in the CCD camera. The known infrared absorbances (or dips in the CCD counts) of the polystyrene are used to calibrate the infrared beam. Stability of the scanning SFG system was verified with the reproducibility of the spectra of neat water /RecNum> an aqueous solution of 8.0 mM sodium dodecyl sulfate (SDS). SFG spectra were normalized to IR profiles detected in real time. SFG spectra with a disrupted temporal overlap of the visible and infrared were also obtained to ensure that the detected SFG signal was truly sum frequency photons. More details of the instrument can be found elsewhere. [17]

In the broad bandwidth sum frequency generation spectrometer, two 1 kHz regenerative amplifiers (Spectra Physics, Spitfire, femtosecond and picosecond version) are seeded by a titanium:sapphire oscillator (Spectra Physics, Tsunami, centered at 792 nm) and pumped by a Q-switched all solid state Nd;YLF laser (Spectra Physics, Evolution 30 at 527 nm). The femtosecond and picosecond amplifiers produce 85 fs pulses and 2 ps pulses, respectively at 792 nm. The femtosecond output pumps an optical parametric amplifier (Light Conversion, TOPAS) to generate a broadband infrared beam of ~ 150 cm^{-1}. The output infrared beam is temporally and spatially overlapped with the 792 nm beam from the picosecond amplifier at the surface of the sample to generate the broadband sum frequency beam. The input energy of the 792 nm is 300 μJ. The infrared beam energies were 3 μJ and 6 μJ for the low and the high frequency region, respectively. A propagating geometry is used in this SFG system where the incident angles of the infrared and visible from the surface normal are 68º and 53º, respectively. The reflected sum frequency beam is dispersed in a monochromator (Acton Research, SpectraPro 500i) using a 1200 g/mm diffraction grating blazed at 750 nm, and then collected in a CCD detection system (Roper Scientific, LN400EB, 1340 x 400 pixel array back illuminated). More details of this spectrometer can be found in previous publications.[39, 48] SFG spectra were normalized to the nonresonant signal from a GaAs crystal.

2.2 Raman Instrumentation

Raman spectra were obtained using 150 mW or 100 mW from a 532-nm continuous wave laser (Spectra-Physics, Millennia II). The beam was focused ~2 mm inside the sample vial using a 5 mm focusing Raman probe (InPhotonics). The Raman scatter was focused with a BK7 lens at the entrance slit of a 500 mm monochromator (Acton

Research, SpectroPro SP-500) in a 90˚ configuration. The residual 532 nm light was removed with a long-pass 535 nm filter (Omega Optical) before entering the monochromator. The Raman scatter was dispersed by a 1200 groove/mm grating blazed at 1 μm and collected on a liquid-nitrogen cooled CCD camera. The slit width was set to 100 μm. Calibration of the monochromator was completed by using the 435.833 nm Hg line of a fluorescent light, and was verified by comparison to the Raman spectrum of crystalline naphthalene. For acquiring polarized Raman spectra, two polarizer films (Edmund Industrial Optics) were used; one to select the polarization coming out of the optic fiber and other film was placed after the sample and before the entrance to the detection system.

A variation of the set up described above was employed to obtain unpolarized spectra in spectral regions above 500 cm^{-1}. In this case, the backscattered radiation was collected by the fiber optic probe (Acton Research, FC-446-030) coupled to the entrance slit of a 500 mm monochromator (Acton Research, SpectroPro SP-500).

2.3 FTIR Instrumentation

A Thermo Nicolet Fourier transform infrared (FTIR) spectrometer (Thermo Electron Corporation, Avatar 370) was employed to acquire attenuated total reflection Fourier transform infrared (ATR-FTIR) spectra. A 45º single-bounce ZnSe crystal mounted on an accessory (Thermo Electron Corporation, Smart SpeculATR) was employed to collect spectra with a spectral resolution of 4 cm^{-1}.

IR spectra in transmission mode were obtained using a Spectrum Spotlight 300 FT-IR Microscope (Perkin Elmer). The sample solutions were placed in-between two CaF_2 windows. Spectral resolution was determined to be 4 cm^{-1}.

2.4 Langmuir -Blodgett (LB) Films

The transfer of a floating lipid monolayer to a solid surface was first described by Langmuir in 1920. [49] The most common method of monolayer transfer used is Langmuir's original method, but because of its extensive application by Blodgett [50] this technique is usually referred as the Langmuir-Blodgett technique. In this method a solid is placed in water before a Langmuir monolayer is spread, and then drawn up through the surface after formation of the film.

Langmuir phospholipid films were acquired with a minimicro LB-trough from KSV Instruments (Monroe, CT). This trough comprises a dipping well and a linear dipper to transfer the Langmuir film from the water subphase onto the solid substrate. A clean substrate was clamped onto the dipper and was partially immersed in the dipping well full of water prior to spreading the phospholipid film. In the Teflon coated film trough a known volume of a 1 mM solution of phospholipid in chloroform was spread dropwise on the surface of the water subphase (pH ~ 6) or aqueous solution. After 10 min to allow for complete solvent evaporation, the compression of the two hydrophilic barriers was initiated. The surface pressure was measured using a Wilhelmy plate composed of Whatman ashless paper. The films were compressed at a constant speed of 5 mm/min. Films were transferred onto the solid substrate by compressing the phospholipid film to the desired surface pressure (i.e. 40 mN/m) followed by withdrawing the solid substrate vertically through the interface into the air. The withdrawing speed was 1 mm/min. The surface pressure was maintained at the desired value throughout the deposition process.

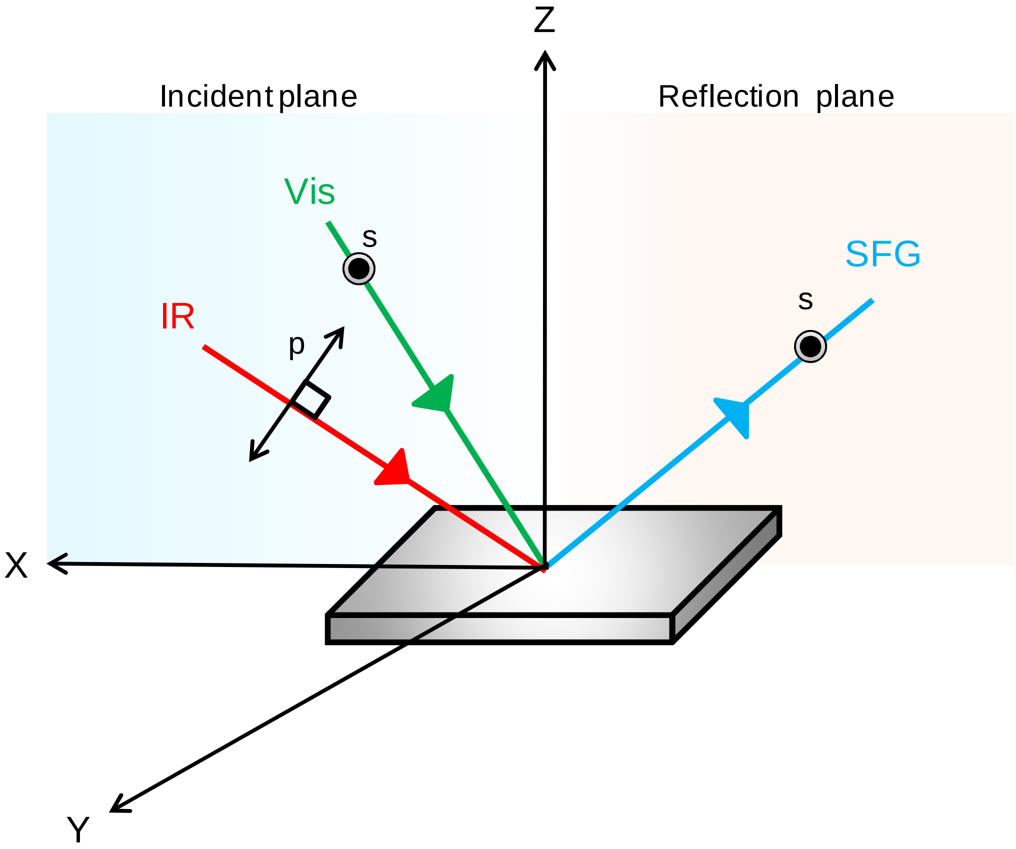

Figure 2.1. Schematic of the SFG experiment at an interface in a co-propagating geometry. The polarization combination represented is ssp.

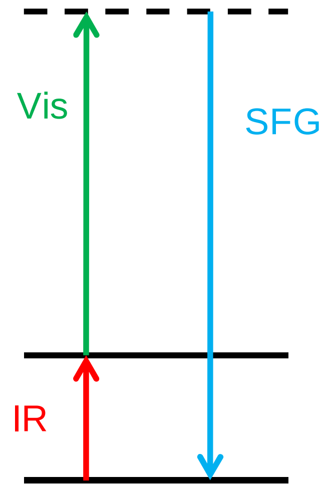

Figure 2.2. Energy level diagram of the sum frequency process.

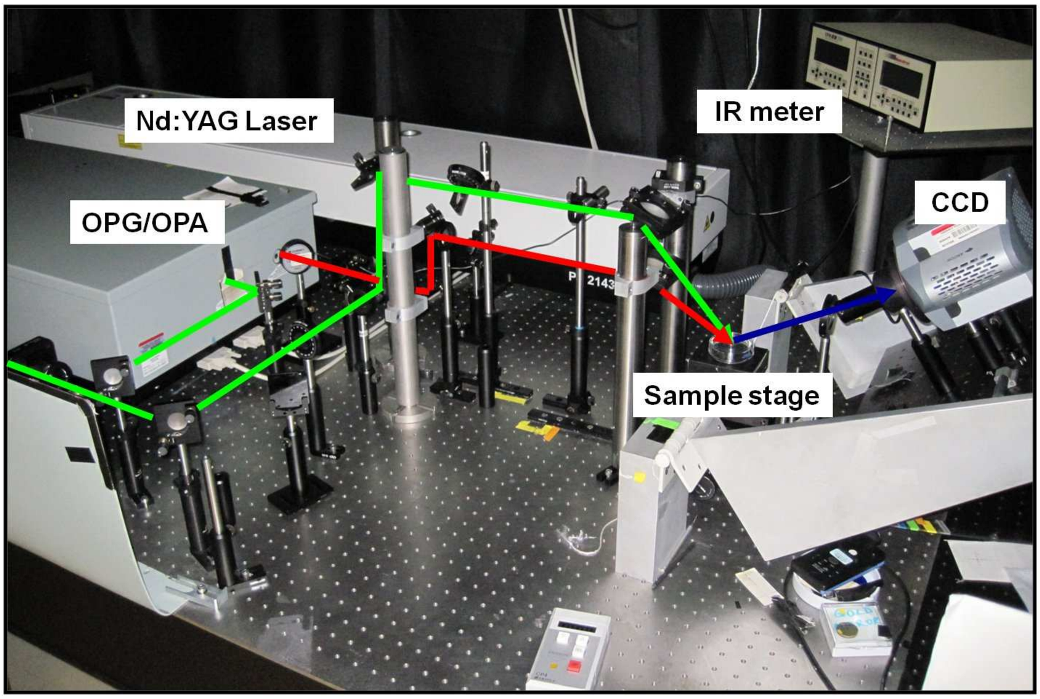

Figure 2.3. Scanning 10 Hz SFG system layout.

Chapter 3

Solvation of Magnesium Dication

Understanding the mechanism of solvation of ionic species has been an important quest in many fields where this phenomenon has a relevant role including biology, and environmental and atmospheric chemistry. [51-54] Magnesium dication is available to the environment from ocean waters and earth's crust [6, 55], its roles in environmental and atmospheric chemistry are still relatively unknown.

In biological systems aqueous Mg^{2+} is important in a wide range of processes. In several instances magnesium is used to stabilize structures, such as cell membranes, proteins, DNA, and RNA.[56-59] The involvement of Mg^{2+} in biological functions occurs not only through direct interactions with biological molecules, but also in interactions through the solvent shell of fully hydrated magnesium dications. [56-59]

Mg^{2+} is the second most common cation in seawater (after sodium)[6], making its effects on sea spray and aged sea salt aerosols an issue of atmospheric relevance. Experimental evidence suggest that contact ion pairing may not exist at ambient conditions in solutions of magnesium chloride up to saturation concentrations.[60-63] This is not typical of most ions. There has been disagreement in the molecular dynamics literature concerning the existence of contact ion pairing in magnesium chloride solutions.[64, 65] In this Chapter, we seek a fundamental understanding of the solvation structure of magnesium in aqueous solutions. To this aim, a concentration dependent Raman spectroscopic study of the

Mg—O$_{water}$ hexaaquo stretch is presented in this Chapter. Chloride was chosen as the anion because of its prevalence in atmospheric marine aerosols.

3. 1 Materials

Magnesium chloride hexahydrate ($MgCl_2 \bullet 6H_2O$; ACS certified) was obtained from Fisher Scientific (PA, USA). Deionized water was obtained from a Barnstead Nanopure filtration system with a minimum resistivity of 18.2 MΩ·cm. A saturated aqueous solution of magnesium chloride was prepared and then filtered through a Whatman Carbon-Cap activated carbon filter to remove organic contaminants. The concentration of the filtered solution was determined by the Mohr method.[66] This solution was then diluted in deionized water to the final concentration. To prepare the two highest concentration solutions, the filtered solution was partially evaporated for several hours at 70 °C to the final concentrations. The $MgCl_2$ mole fraction concentrations used were 0.02x, 0.04x, 0.06x and 0.09x. Mole fractions were calculated using densities from the literature. [67]Because our experimental temperature was lower than that reported by Phang et al., our mole fractions are overestimated and therefore reported to the 2nd decimal. Concentrations of the $MgCl_2$ aqueous solutions expressed in molarity, mole fraction, and the calculated number of water molecules per $MgCl_2$ molecule are listed in Table 3.1

3. 2 Experimental details

Raman spectra for Figure 3.1 were obtained with 150 mW from a 532-nm continuous wave laser (Spectra-Physics, Millennia II). The sample solution was contained in a 2 mL glass vial. The beam was focused ~2 mm inside the vial using a 5 mm focusing Raman probe (InPhotonics). Raman spectra were acquired with 10 min of exposure time and at ~ 22 °C. The average of two Raman spectra is shown. For Figure 3.2, error bars show ± one standard deviation derived from the spectral fits (IgorPro 4.05).

For Figure 3.4, Raman spectra were obtained with a Raman Microscope (Renishaw inVia; Ohio State Department of Chemistry microscope facility) using 60 microwatts from a 785-nm continuous wave laser and a 1200 lines/mm grating resulting in a 3 cm^{-1} resolution at 555 cm^{-1}. The samples, solution drops or solid, were placed on a clean gold-coated glass slide and exposed to the laser radiation for 60 seconds at ~ 22 °C.

3. 3 Results and Discussion

Ab initio and density functional theory (DFT) calculations as well as molecular dynamics simulations show that the first solvation shell of magnesium coordinates six water molecules. [64, 68-75] Both theory and experiments also show that the water molecules in the first solvation shell around magnesium are arranged in a distinct octahedral pattern. Contact ion pairs occur when a cation and anion are adjacent to each other, whereas solvent-shared ion pairs occur when a cation and anion are separated by a water molecule that is in the first solvation shell of both ions.

Raman spectra of aqueous $MgCl_2$ solutions of 0.02x, 0.04x, 0.06x and 0.09x were acquired in the Mg^{2+}—O_{water} stretching region as shown in Figure 3.1. A neat water spectrum is included for comparison. The intermolecular Mg^{2+}—O_{water} peak is observed at ~ 355 cm^{-1}. This peak has been referred to as the hexaaquo $Mg(H_2O)_6{}^{2+}$ stretch. [76-78] The peak area obtained by curve-fitting increases with increasing concentration as shown in Figure 3.2. The analysis reveals a linear correlation between the peak area of the Mg^{2+}—O_{water} band and concentration up to the 0.06x $MgCl_2$ aqueous solution. This linearity suggests that Mg^{2+} cation maintains the six water molecules in its first hydration shell. At 0.09x $MgCl_2$ there is a deviation from linear behavior suggesting a different solvation environment for Mg^{2+} where the primary solvation shell of Mg^{2+} is perturbed, likely due to the fewer number of water molecules available per $MgCl_2$ (Table 3.1; 10 water molecules per $MgCl_2$). In addition, the Raman spectrum of the 0.09x aqueous solution reveals a 6 cm^{-1} red shift, 354 cm^{-1} to 348 cm^{-1}, consistent with a perturbed Mg^{2+} hydration environment as shown in Figure 3.3. While this shift is attributed to a change in hydration environment, it is not assigned to the formation of contact ion pairs. To further evaluate the 0.09x solution and to confirm lack of contact ion pairing, additional Raman spectra lower in frequency were obtained and compared to the spectra from the 0.09x and 0.06x solutions to that of the solid $MgCl_2{\cdot}6H_2O$ as shown in Figure 3.4. A broad band was observed from 190 to 250 cm^{-1} in the 0.09x solution spectrum which is not evident in the 0.06x spectrum, nor from neat water. Although from previous work the appearance of a peak at ~240 cm^{-1} and 230 cm^{-1} was attributed to Mg^{2+}—Cl^- contact ion pairs from melts[79, 80] and from aqueous mixtures of Na^+, Mg^{2+}, Cl^- and $SO_4{}^{2-}$ at 25°C, [81] and from

$MgCl_2$ thin films, [82] we observe resonances in this spectral region from the solid $MgCl_2 \cdot 6H_2O$ as shown in Figure 3.4. These bands from the solid sample arise from the fully hydrated Mg^{2+} ion without contact ion pairing between Mg^{2+} and Cl^- ions and are attributed to a phonon band arising from some long range order[42] in the high concentration solution and are observed here in a fully hydrated Mg^{2+} scenario. The crystalline structure of $MgCl_2 \cdot 6H_2O$ has been confirmed using X-ray diffraction. [83] The observed resonance centered at ~ 230 cm^{-1} and the observed frequency shift of the 355 cm^{-1} peak from the 0.09x $MgCl_2$ solution are therefore consistent with a perturbed hydration environment of fully hydrated Mg^{2+} ions in the 0.09x solution. Hence, there is no clear spectral evidence that contact ion pairing is occurring in the solutions studied here, even for the high concentration solution of 0.09x (4.7 M) $MgCl_2$.

By analyzing the number of water molecules available for solvation at each concentration studied here (Table 3.1), and recognizing that Mg^{2+} is more efficient at attracting hydration water relative to Cl^-, we find that in the lower concentration solutions (0.02x, 0.04x and 0.06x), it is likely that a large portion of the ions have a complete first and even the second solvation shell. For the 0.09x $MgCl_2$ solution, there are insufficient numbers of water molecules available to fill the second solvation shell of Mg^{2+}, or to complete the first solvation shell of all the ions; therefore, substantial solvent-shared ion pairing is unavoidable. A change in the hydration environment of Mg^{2+} at the highest concentration can be easily envisioned when considering that at 0.06x there are 10 water molecules in addition to the 6 water molecules of the first solvation shell for each Mg^{2+}.

According to previous research, the remaining 10 (at 0.06x) water molecules are sufficient to complete a second hydration shell around Mg^{2+} and/or to solvate the Cl^{-} ions.[77, 84, 85] However, some solvent-shared ion pairs are still expected, even at low concentrations. The portion of ions in solvent-shared ion pairs is expected to increase with concentration. Additionally, as concentration increases, some chloride ions will form solvent-shared ion pairs with more than one hydrated magnesium ion simultaneously. At 0.09x there are only 4 water molecules in addition to the first solvation shell for each Mg^{2+} ion. Therefore, there are a large number of solvent-shared ion pairs at this higher concentration.

It has been established by *ab initio* and DFT calculations as well as NMR, Raman spectroscopy, and X-ray absorption spectroscopy (XAS) experiments that magnesium interactions with water molecules in the first solvation shell are far stronger than most other cations.[64, 77, 86-89] Recent molecular simulations of aqueous $MgCl_2$ solutions with similar concentrations to those used in this study have shown that the initial configuration of the simulation plays a critical role in the final pairing condition. [90]To determine if contact ion pairs were present at the initial conditions, the authors performed potential of mean force calculation in which the Helmholtz free energy required to move a chloride ion or water molecule towards magnesium was obtained as a function of distance from magnesium. The results suggested omitting contact ion pairs from the initial conditions. In the same report Callahan *et al.* [90] compared radial distribution function (RDF) obtained from X-ray diffraction of 0.0802x $MgCl_2$ by Caminiti *et al.*[61] with those calculated from molecular dynamics simulations of magnesium chloride, with and without ion pairing in a 0.0888x bulk $MgCl_2$ system. They showed that no contact ion pairs between chloride and magnesium were present in a 0.0802x solution.

3. 4 Conclusions

We have established that Raman spectra of the Mg^{2+}—O_{water} stretch show that contact ion pairing is very unlikely at or below 0.06x, though there are definite changes to the environment of these bonds in the 0.09x $MgCl_2$ solution that complicate the interpretation of the spectra at high concentrations. Theoretical studies of similar concentrations have shown that it is unlikely that aqueous $MgCl_2$ forms contact ion pairs at ambient pressure and temperature even at concentrations approaching saturation.[90] The strong hydration, lack of contact ion pairing to chloride, and ability to strongly orient water, as observed through vibrational spectroscopic techniques, makes magnesium dication unique among cations in its effects on the solution environment.

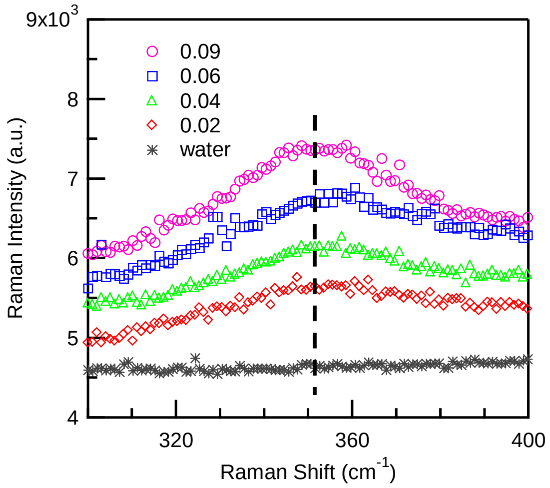

Figure 3.1. Raman spectra of the (Mg^{2+}—O_{water}) stretching vibration for aqueous solutions of $MgCl_2$ at different mole fraction concentrations. Neat water spectrum is included for reference.

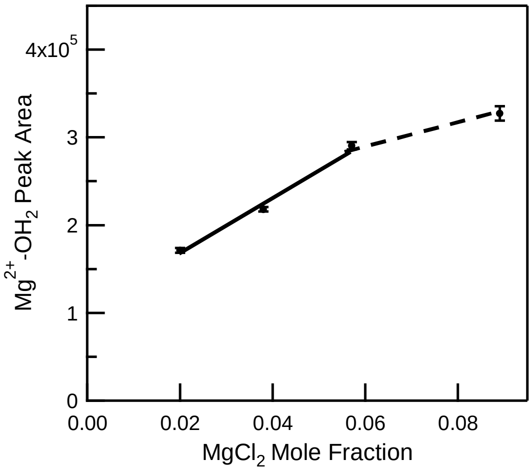

Figure 3.2. Area under the (Mg^{2+}—O_{water}) peak as a function of $MgCl_2$ concentration.

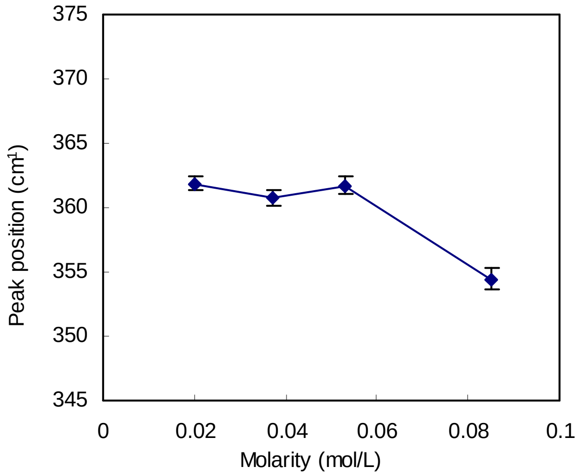

Figure 3.3. Peak position of the intermolecular Mg^{2+}-OH_2 band at different concentration of $MgCl_2$ aqueous solutions

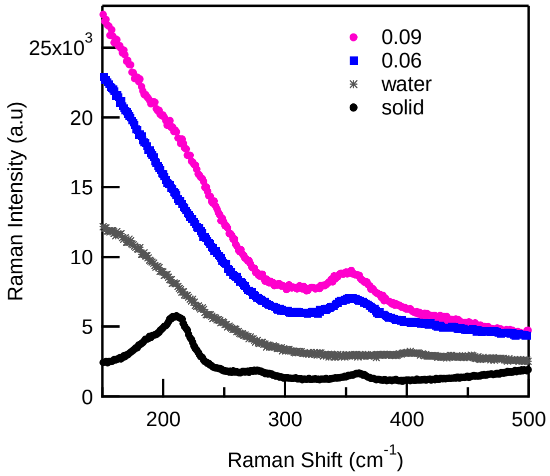

Figure 3.4. Lower frequency Raman spectra of the two highest concentration $MgCl_2$ solutions and the solid $MgCl_2 \cdot 6H_2O$. Also the spectrum of neat water is included for reference.

Molarity (moles/L)	Mole fraction (x)	Number of water molecules per $MgCl_2$
1.1	0.02	49
2.1	0.04	25
3.1	0.06	16
4.7	0.09	10

Table 3.1. Concentrations of the $MgCl_2$ aqueous solutions.

Chapter 4

Water Structure at the Air-Aqueous Interface of $MgCl_2$ Solutions

Inorganic salts in marine aerosols play an active role in atmospheric chemistry, particularly in coastal urban regions. The study of the interactions of these ions with water molecules at the aqueous surface helps to elucidate the role of inorganic cations and anions in atmospheric processes. Inorganic salts present in marine boundary layer (MBL) aerosol originate from turbulent wave action at the surface of the ocean. [91] These aerosols, typically of the micron size range and smaller, travel over continental regions by being entrained in the air mass in which they were created, and have been detected more than 900 km inland. [92] Aerosols play a key role in the modification of global climate through their effect on cloud condensation nuclei prevalence, radiative balance, and level of precipitation. [3, 93] Aerosol composition and size have also been correlated to thunderstorm severity. [94] Alkali metals (Na, K, Li, Rb), alkaline earth metals (Mg, Ca), and ammonium (NH_4^+) make up the majority of cationic species, and halides (F, Cl, Br, and I) and oxidized sulfur and nitrogen ions make up the majority of inorganic anionic species found in MBL aerosol. [6, 95, 96] While calcium and magnesium are the most prevalent divalent cations in seawater and MBL aerosols, chloride anion is the dominant halide species. [6] Although recent cloud drop measurements in the MBL show that calcium concentrations are about 4 times higher than magnesium concentrations, [95] the small size and high charge density of Mg^{2+} gives rise to a strongly hydrated complex in aqueous solution, contributing to its limited ability to form contact ion pairs with anions such as nitrate and chloride. [90, 97, 98] This trait may also result in an unusual impact on surface and subsurface physical properties of MBL aerosol.

Within the MBL, halide chemistry is of global importance because of its crucial role in ozone creation and alternatively, ozone depletion events. [26] For example, chlorine radical reacts faster with hydrocarbons than hydroxyl radical. When chlorine radical and NO_x concentrations reach threshold values, ozone production is dominated by chlorine radical chemistry. [99] This has a major impact on air quality in many coastal urban regions of the world. Recent modeling studies suggest that the formation and self-reaction of surface $OH\cdots Cl^-$ complexes is an important route to molecular chlorine which then photochemically produces two chlorine radicals, and that large and polarizable halide anions like chloride play a significant role at the surfaces of aqueous particles. [25, 26, 99]

There are many unanswered questions concerning MBL aerosols. How do environmentally available ions organize at the surface of MBL aerosols? How do counter cations affect the chemistry of MBL aerosols, for example chloride availability and reactivity? While most environmentally available cations readily ion pair to chloride, the unique size and high charge density of Mg^{2+} allow it to remain hydrated by 6 waters, so that it does not form a contact ion pair with Cl^- even at high concentrations as discussed in Chapter 3. [90] Could this unusual behavior perturb the surface and subsurface of atmospheric aerosols and play a role in chloride activity and availability? Given the strong ability of magnesium to hold onto water, how does concentration affect the interfacial region of aqueous solutions with magnesium?

In this Chapter we address these fundamental interactions and resulting surface perturbations to surface aqueous structure. We present surface vibrational sum frequency generation (SFG) spectroscopic studies of aqueous surfaces relevant to understanding the perturbation caused by marine aerosol concentrations of $MgCl_2$.

4. 1 Materials

A saturated aqueous solution of $MgCl_2$ was prepared and then filtered through a Whatman Carbon-Cap activated carbon filter to remove organic contaminants. The concentration of the filtered solution was determined by the Mohr method.[66] This solution was then diluted in deionized water to the final concentration. To prepare the high concentration solutions (3.1 M and above) the filtered solution was evaporated at 70 °C for several hours to reach the final concentration. The $MgCl_2$ concentrations used were 0.1 M, 0.3 M, 1.1 M, 2.1 M, 3.1 M and 4.7 M.

4. 2 Experimental details

The SFG spectra shown in this Chapter were obtained with the broadband SFG spectrometer. The broadband SFG instrument incident angles for the IR and visible beams from the surface normal were 68º and 53º, respectively. The FWHM bandwidth of the infrared beam was typically 200 to 300 cm^{-1} between 3000 and 3800 cm^{-1}. To cover the OH stretching region from 3000 to 3800 cm^{-1}, four spectral regions were used. SFG spectra were normalized to the nonresonant signal from a GaAs crystal for each spectral region. Overlap of the spectral regions as plotted in the figures was completed through a rigorous analysis of the SFG intensity above a threshold value. In some regions, only the top 30% energy maximum spectral region was used in the spectral stitching as determined by additional spectral analysis through varying the central IR peak as determined by the GaAs SFG spectral profile. SFG spectra were obtained under the ssp (s for the SFG, s for the 800 nm, and p for the infrared beam) and ppp polarization combination (at 3700 cm^{-1}, Figure. 4.6). An average of two replicate spectra is shown in the Chapter and error bars show ± one standard deviation. In the free OH region at 3700 cm^{-1}, the data markers are plotted every 5 data points to improve clarity of the spectra.

Raman spectra were obtained with 100 mW from an unpolarized 532-nm continuous wave laser (Spectra-Physics, Millennia II). Raman spectra were acquired with 2 min of exposure time and at ~ 22 ± 1 °C. The average of two Raman spectra is shown.

IR spectra were obtained using a Spectrum Spotlight 300 FT-IR Microscope (Perkin Elmer) in transmission mode. The salt solutions were placed in-between two CaF_2 windows. A total of 124 scans were acquired for each sample. Because variations in the thickness of the solutions are unavoidable, the spectra were normalized to the intensity of the 2200 cm^{-1} band as described in detail in Appendix A.

4. 3 Results and Discussion

We report surface water organization and structure from interpretation of aqueous $MgCl_2$ SFG spectra. SFG ssp spectra of 0.1 M, 0.3 M, 1.1 M, 2.1 M, 3.1 M, and 4.7 M aqueous $MgCl_2$ are shown in Figure 4.1a and b. Before $MgCl_2$ addition, the spectrum of neat water reveals a broad continuum that spans from 3000 to 3600 cm^{-1} and is assigned to the OH stretching modes of hydrogen bonded water molecules. The assignments within this continuum are controversial and still under discussion [7, 100-106] however, as the frequency of the OH stretching modes increases, the strength of the hydrogen bonds between water molecules decreases. [7, 10] This spectral region is also affected by coupling [106] and the collective nature of the vibrations. [10] At 3700 cm^{-1} a narrow peak is observed and is assigned to the free OH of water molecules that straddle the air-aqueous interface with one OH bond uncoupled and oriented toward the gas phase and the other OH interacting through hydrogen bonding with the water molecules in the liquid phase. [107]

$MgCl_2$ concentrations less than 1.0 M (Table 4.1) are shown in Figure 4.1a. These SFG spectra reveal only minor changes relative to water. For the 0.1 and 0.3 M aqueous solutions, a slight spectral narrowing is observed at the edges of the hydrogen bonding region at 3000 and 3600 cm^{-1}. In the 0.3 M solution spectrum, a small intensity enhancement is observed around 3300 cm^{-1}. The free OH region at 3700 cm^{-1} shows no change relative to water. For $MgCl_2$ concentrations of 1.1 M, 2.1 M, 3.1 M, and 4.7 M (Table 4.1), the SFG spectra in Figure 4.1b show a significant intensity enhancement around 3300 cm^{-1} accompanied by an increase in the narrowing of the low and high frequency edges of the hydrogen bonding region as one increases the $MgCl_2$ concentration. By analyzing the spectra in Figure 4.1a and b using parameters identified through phase analysis of aqueous salt solutions by Shen and coworkers[108], one band at ~3200 cm^{-1} with positive phase and a second band at ~3400 cm^{-1} with negative phase fit the spectra rather well (Table 4.2). Additionally, peaks at ~ 3650, 3700, and 3750 cm^{-1}

were used, all with positive phase. We have also tested the band amplitudes by increasing the nonresonant term (as expressed in equation 2.6). [109, 110]Through the analysis, we observe that the apparent narrowing of the hydrogen bonding region can also be interpreted as a blue shift of the ~3200 cm^{-1} band and a red shift of the ~3400 cm^{-1} band with increasing salt concentrations. Although spectral narrowing may be associated with an increase in lifetime of the hydrogen bonds in the hydrogen bonding network, it is difficult to ascertain here.

The spectral intensity at ~3300 cm^{-1} increases in the order of 0.1 M, 0.3 M, 1.1 M, 2.1 M, and then decreases with concentration above 2.1 M; the 4.7 M spectrum nearly overlaps with the 1.1 M spectrum in the hydrogen bonding region. Noncentrosymmetric hydrogen bonding structures may extend deeper below the surface of the 2.1 M solution relative to the other solutions studied here. Application of the SFG selection rule, lack of inversion symmetry requirement for SFG activity, provides indirect data on concentration gradients in the interfacial region up until the SFG coherence length upon reflection. However, an increase in the ordering of the water dipole will also increase the intensity since SFG is highly sensitive to orientation.

Contrary to the maximum 3300 cm^{-1} intensity observed in the hydrogen bonding region for the 2.1 M solution in Figure 4.1b, the intensity of the free OH peak centered at 3700 cm^{-1} for neat water is reduced in accordance with decreasing water content (increasing salt concentration), as expected, although the intensity reduction is rather modest. The 3700 cm^{-1} peak is discussed later with respect to polarization analysis of SFG spectra.

A small broad peak at 3650 cm^{-1} in the SFG spectra of Figure 4.1b is observed and becomes more easily discernable because of the narrowing of the hydrogen bonding region at higher concentrations. To determine whether this peak belongs to vibrational modes of water molecules hydrogen bonded or from free OH modes, a temperature study was conducted and shown in Figure 4.2. In this Figure SFG spectra of aqueous $MgCl_2$ solutions of 4.7 M at 295 K and 285 K and spectral fits are shown. While, the hydrogen bonding region below 3550 cm^{-1} decreases with decreasing temperature, the 3650 cm^{-1} shoulder and the 3700 cm^{-1} peak are not affected, confirming that the shoulder at 3650 cm^{-1} is a dangling OH bond that is not involved in hydrogen bonding with neighboring water molecules. Therefore, a free OH of interfacial water molecules with their oxygens interacting with Mg^{2+} or with the Mg^{2+} solvation shell contributes to this band. [111]A peak in this spectral region was also observed by others and assigned to the symmetric stretch of the decoupled free OH and donor-bonded OH of three-coordinate water molecules [108] and weakly hydrogen bonded water molecules. [102]

Comparison of the data in Figure 4.1a and b to previously published surface water structure spectra of other salts reveals some interesting differences. SFG spectra of aqueous sodium halide [7, 10], ammonium and sodium sulfate [10], and divalent-cation nitrate salt solutions [7] reveal enhancements in the 3400 cm^{-1} region, although the aqueous ammonium chloride salt spectrum [10] showed enhancement at 3300 cm^{-1} as is observed here for $MgCl_2$. Also different than observed in Figure 4.1, a significant loss in intensity in the 3200 cm^{-1} region was observed in SFG spectra of aqueous alkaline earth (Mg^{2+},

Ca^{2+}, and Sr^{2+}) nitrate solutions, and a relatively unperturbed 3400 cm^{-1} band frequency was observed in SFG spectra of aqueous $Mg(NO_3)_2$. [7]

In this study, the necessary Raman and infrared vibrational spectra from the same bulk solutions were acquired (Figure 4.3 and 4.4) as were used in the SFG studies. SFG spectral component peaks can be related to the parallel-polarized Raman (Figure 4.3a) and IR (Figure 4.4) component peaks (Table 4.2 and 4.3) because of the mathematical relationship between SFG intensity and Raman multiplied by the IR transition moments as shown in equation 2.10 in Chapter 2.

As expected, the free OH peak observed so clearly in the SFG spectra at 3700 cm^{-1} is not observed in the Raman or IR spectra. Just as in the SFG spectral analysis, the details associated with the spectral assignment of the hydrogen bonding region remains somewhat controversial. [7] The controversy mainly attends to arguments against assigning underlying bands to specific water populations since there are strong intermolecular interactions and coupling that play a role in the shape of the spectra in Raman [105] and IR.[100, 112-114] This controversy disallows specific inference to structural details of water coordination and microstructures from vibrational spectra, but this is not addressed in this dissertation. We are mainly interested in comparing the parallel-polarized Raman and IR with the ssp-polarized SFG component band intensities in the hydrogen bonding region to gain insight into the question about the extent that the hydrogen bonding environment is different at the air-aqueous interface relative to the bulk.

In Figure 4.3a, the parallel-polarized Raman spectrum of neat water is affected upon addition of $MgCl_2$. As the concentration is increased, the spectra narrow with the 3200

cm^{-1} band decreasing in intensity whereas the 3400 cm^{-1} band increases. The increase in the 3400 cm^{-1} band is significantly larger than the decrease in the 3200 cm^{-1} band. It has previously shown [7, 10, 17]that halides strongly perturb the OH stretching region in the Raman spectrum and coined the 3400 cm^{-1} band as the "solvation shell band" because the polarizability of the water molecules in the solvation shell of a halide become significantly affected by the polarizability of the halide anions. [7, 10, 17] Additionally observed, the frequency of the 3400 cm^{-1} band progressively changes as the concentration is increased. Perpendicular-polarized Raman and unpolarized Raman and of the same aqueous $MgCl_2$ solutions were acquired and are shown in Figure 4.3b and c for reference. Also interesting to note is that the parallel-polarized Raman spectra and the unpolarized Raman spectra follow the same trend.

In the transmission IR spectra (Figure 4.4), an increase in both the 3200 and 3400 cm^{-1} band is revealed. We also observe a larger enhancement of the 3400 cm^{-1} band relative to the 3200 cm^{-1} band consistent with the Raman spectra, although not as dramatic as that which is observed in the Raman. Interesting, but not yet explainable, the 4.7 M $MgCl_2$ IR spectrum is enhanced more than expected from the observed enhancement levels of the lower concentration solutions. However, the solution is highly concentrated at 4.7 M $MgCl_2$, and a large portion of the water molecules are in primary solvation shells of the Mg^{2+} ions. In Chapter 3[90], we have shown that Mg^{2+} retains its six solvation shell water molecules in these low water conditions. In the analysis of the intensity trends of the band at ~3400 cm^{-1}, the Raman and IR show that the intensity increases with increasing

$MgCl_2$ concentration; but as stated previously, the SFG intensity increases up until 2.1 M and then decreases with further addition of $MgCl_2$.

In accordance with equations 2.6 to 2.10, we have analyzed in Figure 4.5 the parallel-polarized Raman and transmission IR spectra acquired from the bulk solutions to compare to the ssp polarized SFG spectra from the air-aqueous interfaces for intensity and frequency trends. In Figure 4.5, comparison plots (left-hand y axis) show the ratio of the 3400 to the ~3250 cm^{-1} band from the SFG ssp, parallel-polarized Raman, and transmission IR spectra. This comparison sheds light on the differences between the surface (SFG) and the bulk solvation environments (Raman and IR). Although we observe only a small variation in the SFG data, the Raman and IR data reveal a substantial increase in this ratio with increasing $MgCl_2$ molarity, especially in the Raman data. The 3400 cm^{-1} band positions determined by component peak analysis (Table 4.3, 4.4) are shown on the right-hand axis of the plots. Opposing trends are observed for the SFG relative to the Raman. Although the Raman and IR frequency trends are not completely consistent with each other, there is an observed red shift from the 4.7 M solution for both. The SFG spectra have a minimum in the peak position plot for the 2.1 M $MgCl_2$ solution that suggests a different hydrogen bonding structure for the 2.1 M air-solution interface relative to the lower and higher $MgCl_2$ concentrations. In the bulk phase Raman and IR spectra there is an overall increase in intensity of the 3400 cm^{-1} peak with the addition of $MgCl_2$, while in the Raman the 3200 cm^{-1} peak is greatly diminished with increasing concentration. This is most noticeable at 4.7 M.

Radial distribution functions of water around magnesium [42] show increasing order beyond the second solvation shell of Mg^{2+} as the $MgCl_2$ concentration increases, both in the bulk and at the interface. As the concentration increases, a larger fraction of the water molecules are directly interacting with ions. Ab initio calculations on ion-water clusters suggested that an OH oscillator donating to Cl^- experiences a large increase in intensity. [115] This has been observed for aqueous halide solutions from Raman spectra. [116] These previous studies strongly suggest that the increase in intensity of the IR and Raman spectra are at least in part due to increasing interactions of water molecules with ions.

Unlike the bulk hydrogen bonding region where the spectral intensity increases with $MgCl_2$ concentration, the spectral intensity of the air-aqueous solution interface does not follow a linear concentration trend. At low concentrations, increasing salt concentrations do increase the SFG spectral intensity in the hydrogen bonding region as with other salts, in agreement with the idea that addition of salt increases the width of the SFG-active interfacial layer. However, reported MD density profiles of $MgCl_2$ aqueous solutions of similar concentrations have shown vertical compression of the stratified layers of salt enhancements with increasing concentration.[42] At low concentrations this could cause the water to orient more strongly with increasing concentration. However, as higher concentrations are reached, this compression reduces the width of the non-centrosymmetric SFG-active environment, eventually causing the spectral intensity to start decreasing with increasing concentration (~2.1 M). The effect is considerable at 4.7 M.

Spectral narrowing in both the Raman and SFG spectra has been observed at every concentration of $MgCl_2$ considered here, and previously in NaCl solutions. [7] The spectral narrowing, which has also been viewed as a red-shifting of the 3400 cm^{-1} peak and a blue shifting of the 3200 cm^{-1} peak in both Raman and SFG spectra, suggests a change in the hydrogen bonding network. Water-water interaction energy distributions have shown that the addition of salt ($MgCl_2$ or NaCl) in neat water results in a loss of water-water hydrogen bonds.[42] While addition of either salt is expected to disrupt water-water hydrogen bonds, it is clear that Mg^{2+} has a much greater disruptive influence on water-water hydrogen bonds than Na^+ at the same concentration.[42] Therefore, spectral narrowing may be linked to loss of water-water hydrogen bonds, corresponding to negative interaction energies, while shifting of the 3400 cm^{-1} peak may be loosely related to the less typical hydrogen bond interactions induced by ions. Dynamics and therefore changes of the vibrational lifetime may also account for some of the apparent spectral narrowing.

The free OH stretch at 3700 cm^{-1} was investigated in a separate set of SFG experiments to elucidate intensity and frequency changes of the aqueous $MgCl_2$ surfaces relative to neat water. In Figure 4.6, ssp polarized and ppp polarized SFG spectra are shown. A 5 cm^{-1} blue shift of the free OH is observed from the lowest to the highest $MgCl_2$ concentration: however, the 3700 cm^{-1} component peak of the spectral fits is observed to red shift with an increase in the magnitude of the nonresonant term. Therefore, due to the complexity of these spectra, we refrain from assigning the observed shift to a specific interfacial structure.

Upon further inspection of Figure 4.6, a signal reduction with $MgCl_2$ concentration is revealed. This reduction is also observed after sensitivity testing of the nonresonant term in the fitting procedure (Table 4.2). Orientational analysis of the free OH stretch of neat water has been reported previously. [117, 118] Briefly, the ratio of different second order nonlinear polarization tensor elements (χ_{ijk}), in this case ssp ($\chi_{xxz}=\chi_{yyz}$) and ppp (χ_{zzz}, χ_{yyz}, χ_{yzy}, and χ_{zyy}), is related to the mean orientational angle (θ). Orientation analysis reveals that the ssp to the ppp intensity ratios do not change except in the case of the 3.1 M and 4.7 M solutions. For these higher concentrations the average orientation of the free OH is determined to be 31 ± 2°, whereas the free OH from neat water is determined to be 33 ± 2°. The angles are within the error of the orientation calculation where the main contributor is the spectral fits. Therefore, we assign the intensity reduction to a reduced number of free OH oscillators assuming that the free OH bandshape is not strongly affected by a change in the vibrational lifetime. The number density reduction of free OH of $< 10\%$ based on the SFG spectra is smaller than one might expect by subtracting surface waters displaced by surface Cl^-.

Although a small decrease in SFG intensity with increasing concentration of $MgCl_2$ for concentrations up to 2.1 M was observed in Figure 4.6, molecular dynamics simulations of the same solutions have shown an increase in the number of free OH as the concentration increases. [42] This discrepancy has been previously attributed to red-shifting of free OH in the first solvation shell of Mg^{2+} out of the peak attributed to other free OH contributions, as well as to perturbations of the intensity of free OH stretches by ions. [119, 120] For 3.1 M and 4.7 M $MgCl_2$, a larger decrease in SFG intensity of the free OH peak is observed relative to the lower concentrations. The free OH orientational distributions show that with increasing concentration, layers of free OH with opposing orientations appear. [42] This generates stratification of the net orientation of the free OH. The SFG signal from these layers of free OH with opposing orientation would be expected to interfere destructively, leading to a loss in SFG intensity in the free OH region in addition to that expected from frequency and intensity changes due to water-ion interactions.

4. 4 Conclusions

Spectroscopy results reveal that the disturbance of the hydrogen bonding environment of the air-aqueous interface is dependent on the $MgCl_2$ concentration. At low concentrations (< 1 M) minor changes are observed. At concentrations above 1 M the hydrogen bonding environment is highly perturbed. The 2.1 M intermediate concentration solution shows the largest SFG response relative to the other solutions including concentrations as high as 4.7 M. The enhancement of SFG signal observed for the 2.1 M solution is attributed to a larger SFG-active interfacial region and more strongly oriented water molecules relative to other concentrations. MD simulations reported in the literature[42] reveal concentration dependent compression of stratified layers of ions and water orientation differences at higher concentrations of $MgCl_2$. SFG studies of the dangling OH of the surface water reveal that the topmost water layer is affected structurally at high concentrations (> 3.1 M).

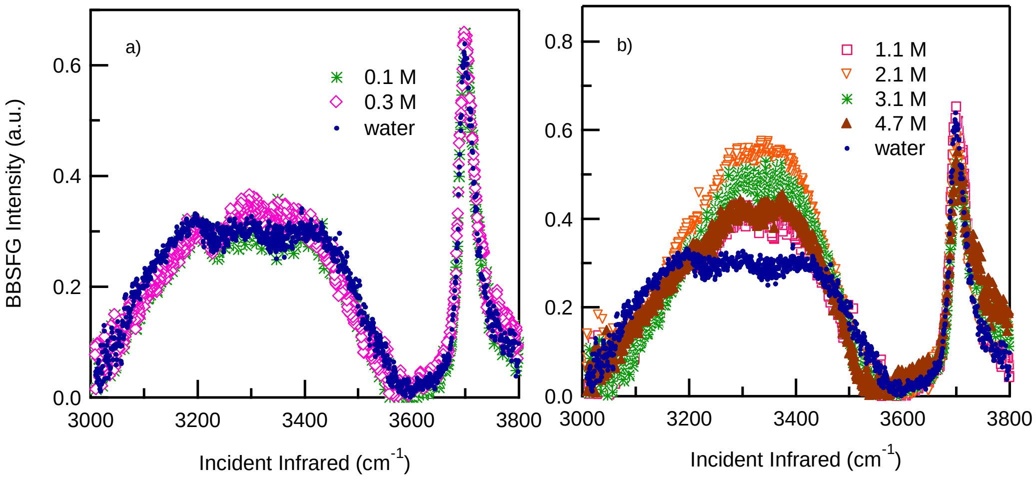

Figure 4.1. SFG spectra of aqueous $MgCl_2$ solutions of a) 0.1 M and 0.3 M and b) 1.1 M, 2.1 M, 3.1 M and 4.7 M. Neat water spectrum is also shown for reference.

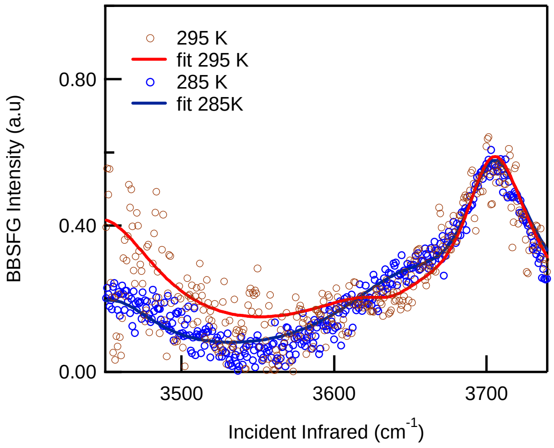

Figure 4.2. Spectra of aqueous 4.7 M $MgCl_2$ solutions at 295 K and 285 K.

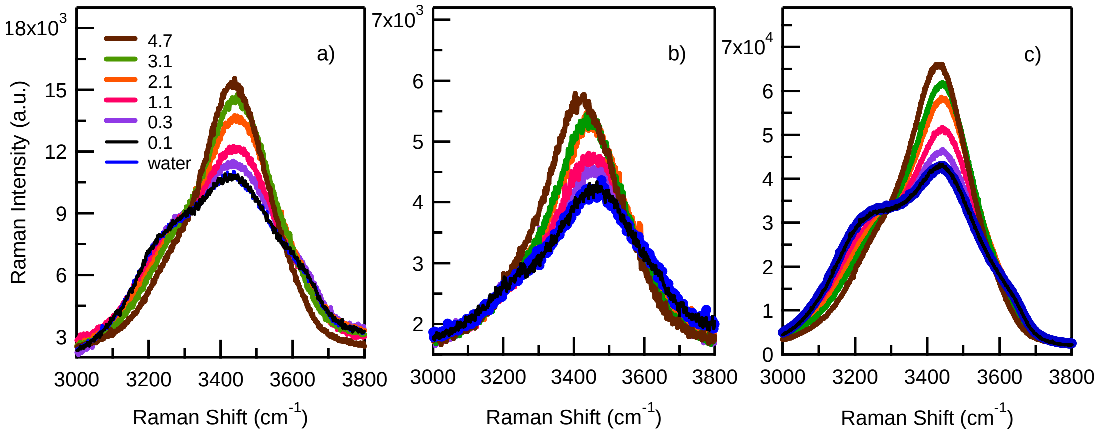

Figure 4.3. a) Parallel-polarized Raman, b) perpendicular-polarized Raman, and c) unpolarized Raman spectra of aqueous $MgCl_2$ solutions of 0.1 M, 0.3 M, 1.1 M, 2.1 M, 3.1 M and 4.7 M in the OH stretching region. Neat water spectra are included for reference.

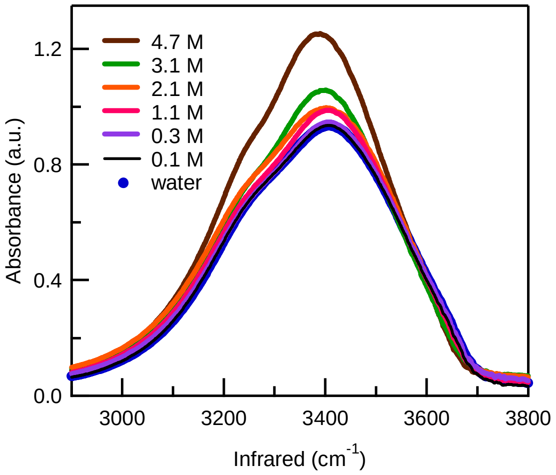

Figure 4.4. Transmission-infrared spectra of aqueous $MgCl_2$ solutions of 0.1 M, 0.3 M, 1.1 M, 2.1 M, 3.1 M and 4.7 M in the OH stretching region. Neat water spectra are included for reference.

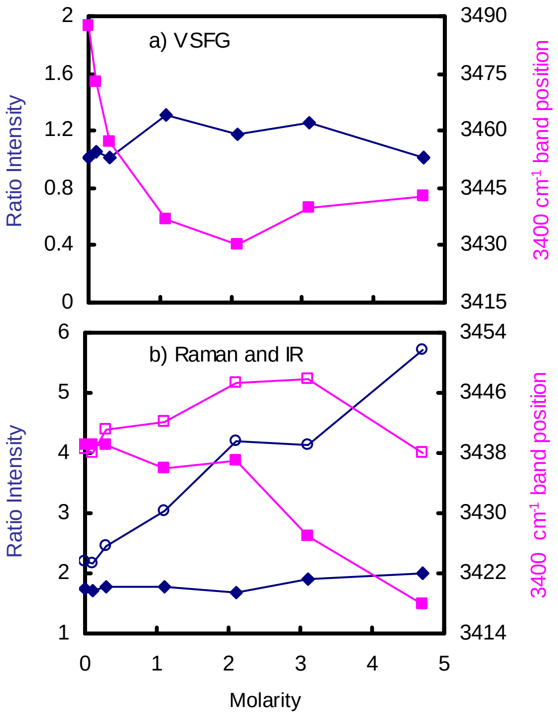

Figure 4.5. a) SFG, b) parallel-polarized Raman (open symbols), and IR (solid symbols) ratios of the 3400/3250 cm^1 bands (dark blue diamonds), and the peak position of the ~3400 cm^{-1} band (pink squares).

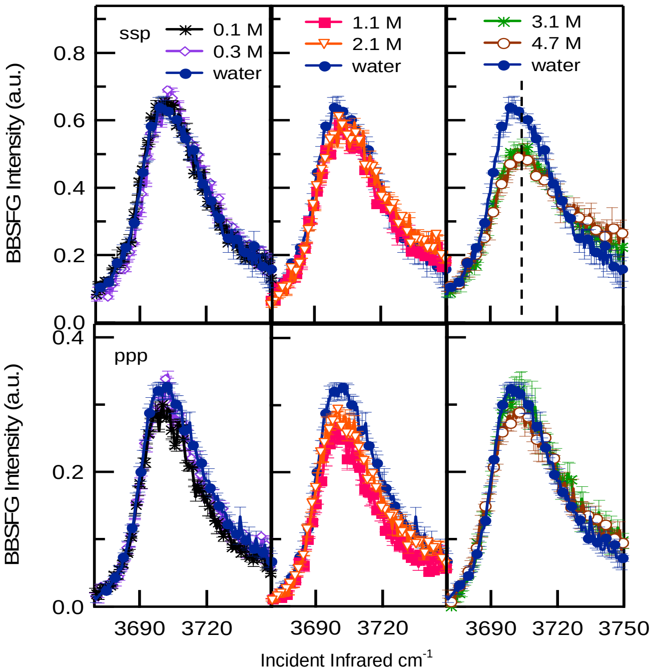

Figure 4.6. SFG spectra of aqueous $MgCl_2$ solutions using ssp (top row) and ppp (bottom row) polarization combinations. Neat water spectra are also shown for reference.

Molarity (Moles/L)	Mole fraction (x)	Number of water molecules per $MgCl_2$	Number of water molecules per ion (third column/3)*
0.1	0.002	558	186
0.3	0.005	185	62
1.1	0.02	49	16
2.1	0.04	25	8
3.1	0.06	16	5
4.7	0.09	10	3

Table 4.1. Concentration of the $MgCl_2$ aqueous solutions in molarity, mole fraction, and number of water per $MgCl_2$ and per ion.

	Peak position cm^{-1}	Phase	Amplitude	FWHM	Area (a.u)	Amplitude*	FWHM *	Area (a.u.) *
Water	3118	+	48.0	240	41.3			
	3488	-	48.6	200	63.9			
	3645	+	2.0	40	0.6			
	3700	+	13.0	34	30.2			
	3750	+	6.0	110	1.8			
0.1 M $MgCl_2$	3125	+	48.3	250	40.2			
	3474	-	50.6	210	65.5			
	3645	+	2.0	40	0.6			
	3701	+	13.1	33.7	31.1			
	3755	+	6.0	110	1.8			
0.3 M $MgCl_2$	3128	+	51.3	264	43.3			
	3457	-	52.1	210	69.4			
	3645	+	2.0	40	0.6			
	3702	+	12.5	32.5	29.4			
	3755	+	6.0	110	1.8			
1.1 M $MgCl_2$	3160	+	49.21	240	46.5			
	3437	-	64.33	220	100			
	3638	+	1.5	40	0.4			
	3702	+	12.64	35.5	27.3			
	3755	+	8	110	3.2			
2.1 M $MgCl_2$	3187	+	62	250	73.1	44	260	34.7
	3430	-	73.3	210	137	60	220	87
	3630	+	1.5	40	0.3	5	60	2.5
	3703	+	13.8	38.4	29.7	12.7	40	24.6
	3755	+	8	80	5.1	1	80	0.07
3.1 M $MgCl_2$	3185	+	53.54	230	59.8			
	3440	-	67.33	210	115.6			
	3645	+	0.2	44	0.005			
	3704.4	+	10.5	36.4	18.4			
	3744	+	14.5	110	10.4			
4.7 M $MgCl_2$	3174	+	58.6	250	63.7	37	250	25.4
	3449	-	59	182	104.7	47	182	66.5
	3630	+	2	60	0.3	10	80	7.3
	3705	+	12.05	48	18	10.52	43.2	15.4
	3770	+	26	180	18.3	7	180	1.3

Table 4.2. Parameters for the SFG spectral fits of 0.1 M, 0.3 M, 1.1 M, 2.1 M, 3.1 M and 4.7 M $MgCl_2$ aqueous solutions. Spectral fits were calculated with constant nonresonant terms of 0.019 - 0.03*i*, except the columns denoted by *. Those parameters were obtained with nonresonant terms of 0.35 -0.03*i*.

	Peak position cm^{-1}	Amplitude	FWHM	Area (a.u)
Water	3232.2	3535.4	230	188236
	3438.6	7714.8	320	419562
	3630.0	1527.6	180	81378
0.1 M $MgCl_2$	3230.7	3576.9	230	190630
	3438.0	7742.6	320	421152
	3630.0	1661.7	180	88558.7
0.3 M $MgCl_2$	3232.6	3440.6	230	183081
	3441.0	8414.8	320	457377
	3630.0	1639.7	180	90297
1.1 M $MgCl_2$	3219.9	3023.2	230	161957.7
	3442.1	9149.7	320	497011.5
	3630.0	759.2	180	40449.4
2.1 M $MgCl_2$	3229.3	2447.5	230	130555.9
	3447.3	10360.6	320	561700.7
	3630.0	428.3	180	22809.4
3.1 M $MgCl_2$	3239.3	2748.5	230	158447
	3446.9	11329.7	290	563956
	3630.0	1008.2	180	53730
4.7 M $MgCl_2$	3228.3	2157.6	230	115160
	3438	12342.5	280	606778
	3630	450.5	180	28190.7

Table 4.3. Parameters for the parallel polarized Raman spectral fits of 0.1 M, 0.3 M, 1.1 M, 2.1 M, 3.1 M and 4.7 M $MgCl_2$ aqueous solutions.

	Peak position cm^{-1}	Amplitude	FWHM	Area (a.u)
Water	3239	0.43	338.1	14.9
	3439	0.76	316.8	21.0
	3596	0.10	146	4.8
0.1 M $MgCl_2$	3238	0.44	337.3	15.4
	3439	0.77	310.9	22.7
	3596	0.10	141.4	3.1
0.3 M $MgCl_2$	3237	0.43	342.7	14.8
	3439	0.76	314	22.5
	3593	0.10	140.3	2.9
1.1 M $MgCl_2$	3234.7	0.44	357.8	15.5
	3436.6	0.79	313.8	23.3
	3589	0.08	135.8	2.6
2.1 M $MgCl_2$	3234.3	0.47	348	16.5
	3436.7	0.79	312.3	23.3
	3579.7	0.08	120	2.4
3.1 M $MgCl_2$	3233	0.44	346	15.3
	3427	0.83	304	24.7
	3582	0.08	121.1	2.4
4.7 M $MgCl_2$	3233	0.50	350	18.1
	3418.7	1.0	308	29.6
	3576	0.097	118.1	2.8

Table 4.4. Parameters for the IR spectral fits of 0.1 M, 0.3 M, 1.1 M, 2.1 M, 3.1 M and 4.7 M $MgCl_2$ aqueous solutions.

Chapter 5

Water Structure at the Air-Aqueous Interface of a Model Seawater Solution

Seawater is composed of a combination of inorganic salts.[6] After sodium the next most prominent cation of seawater is magnesium, with one Mg^{2+} for every eight Na^{+}, while the most abundant anion is chloride. Experimental and theoretical studies have shown that chloride anions are present at the air-solution interface of halide salt solutions.[7-10, 12-15, 17-24, 121] This observation has been important for the development of a mechanism for the heterogeneous production of molecular chlorine gas from chloride ions in sea salt aerosol.

The addition of alkaline earth salts in previous studies of the chloride enhancement at interfaces is limited. [122] In this chapter, an interfacial vibrational spectroscopic technique was used to investigate the effect of magnesium dication in a model seawater solution aerosol. We use salt solutions that are more concentrated than seawater in the ocean, since it corresponds to seawater aerosols that have had a chance to undergo evaporation while spending time in the atmosphere.

5. 1 Materials

Magnesium chloride hexahydrate ($MgCl_2 \cdot 6H_2O$; ACS certified) and sodium chloride (NaCl; ACS certified) were obtained from Fisher Scientific. For the sodium chloride solutions, the NaCl salt was placed in a muffle oven (Fisher Scientific, Isotemp Muffle Furnace) at 700 °C for 4 hours to eliminate any organic contaminants prior to mixing with Nanopure water (18.2 MΩ·cm) to obtain the final concentration. For magnesium chloride, a saturated aqueous solution of $MgCl_2$ was prepared and then filtered through a Whatman Carbon-Cap activated carbon filter to remove organic contaminants. The concentration of the filtered $MgCl_2$ solution was determined by the Mohr method.[66] The concentrated $MgCl_2$ solution was then diluted to the final concentration using Nanopure water. The final concentrations of the salt solutions employed were 2.1 M for $MgCl_2$, 4.5 M of NaCl plus 0.3 M of $MgCl_2$ for the model seawater solution, and 4.9 M for NaCl.

5. 2 Experimental details

SFG spectra of the air-liquid interface were acquired using the scanning (SSFG) and the broad bandwidth (BBSFG) spectrometer. Details of these two SFG systems are described in Chapter 2. SFG spectra were obtained under the ssp in the SSFG spectrometer, and ppp polarization combinations in the BBSFG spectrometer. For the SSFG spectra, each data point was acquired using 30 s of exposure time. SSFG spectra were normalized by the infrared energy, which was measured in real time with the SFG intensity. BBSFG spectra were normalized to the nonresonant signal from a GaAs crystal.

An average of at least two replicate spectra is shown in all cases and error bars show ± one standard deviation. In the case of the BBSFG spectra, the data markers were plotted every 5 data points to improve clarity. Spectra were acquired at ~ 22 ° C and in a range from 40 to 50% relative humidity. The SSFG spectra of water and the 2. 1 M $MgCl_2$ solution discussed in this Chapter have been previously acquired with the BBSFG spectrometer and reported in Chapter 4. Both spectra reveal similar shape, although the SSFG spectra present better signal to noise ratio in all regions.

Raman spectra were obtained with 150 mW from an unpolarized 532-nm continuous wave laser. Raman spectra were acquired with 1 min of exposure time and at ~ 22 ± 1 °C. The average of two Raman spectra is shown. Unpolarized Raman spectra were acquired instead of parallel-polarized spectra in view of the fact that the spectral trend is conserved in both conditions as shown in Figure 4.3.

IR spectra were obtained using a Spectrum Spotlight 300 FT-IR Microscope in transmission mode. The salt solutions were placed in-between two CaF_2 windows. A total of 124 scans were acquired for each sample.

5. 3 Results and Discussion

In Figure 5.1 a-c, the ssp polarized SFG spectra of aqueous solutions of magnesium chloride, the model seawater, and sodium chloride are shown. The spectrum of neat water is provided with each for reference. There are three spectral regions that we will compare: 3000-3200 cm^{-1}, 3200-3600 cm^{-1}, and 3600-3800 cm^{-1}. Addition of chloride salts leads to changes in all three spectral regions compared to the spectrum of neat water.

Before analyzing these changes, a description of the neat water SFG spectrum is necessary. This spectrum shows an identical shape to that obtained with the BBSFG spectrometer shown in Figure 4.1 (Chapter 4). As described early, the broad band that extends from 3000 to 3600 cm^{-1} is assigned to the OH stretching modes of hydrogen-bonded water molecules, although the precise assignment within this spectral region is controversial as discussed in Chapter 4. Also seen and previously assigned is the free OH peak at 3700 cm^{-1}.[107] The SFG spectrum of aqueous $MgCl_2$, and to a lesser extent the model seawater SFG spectrum, show a depletion of signal relative to that of the water spectrum in the 3000 cm^{-1} to 3200 cm^{-1} region. This spectral region is generally ascribed to highly structured water or modes of strongly hydrogen-bonded water molecules. Several reasons can be proposed for the observed depletion of signal in the SFG spectrum as discussed later.

The region around 3400 cm^{-1} (3200 cm^{-1} to 3600 cm^{-1}) shows a signal enhancement relative to that of pure water in the SFG spectra of all the salt solutions. This region is typically assigned to less strongly or asymmetrically hydrogen-bonded water molecules of varying strengths and geometries. Also this band has been referred to as the solvation shell band (Chapter 4). The largest intensity enhancement is observed in the $MgCl_2$ solution spectrum (Figure 5.1a). In addition, this enhancement seems to be red shifted by ~50 cm^{-1} relative to the NaCl solution spectrum (Figure 5.1c). If the signal enhancement in the 3400 cm^{-1} region was caused only by the presence of chloride, one would expect the largest signal enhancement in the seawater solution where the total molarity is the highest. In fact, the opposite trend is detected. This suggests that the signal intensity is highly influenced by the nature (valence) and concentration of the cation. That is, the resultant intensity will depend on the relationship between the local fields of both the anion and cation in the aqueous environment. Although, the bulk concentration of the Mg^{2+} cation is half of that of the Na^+ cation the highest intensity is observed for the $MgCl_2$ solution spectrum. This suggests that Mg^{2+} has a larger local field effect on the signal intensity relative to Na^+ at the surface. More importantly, the noncentrosymmetric hydrogen bonding structures and hence SFG-active areas generated by concentration gradients in the interfacial regions could differ in the different salt solutions. This would lead to differences in SFG-active region below the interfacial region among the salt solutions, and consequently, differences in signal intensity would be observed.

Raman and IR spectroscopy can be utilized to obtain insight into the bulk hydrogen bonding. Unpolarized Raman and IR spectra of aqueous solutions of $MgCl_2$ 2.1 M, the model seawater (NaCl 4.5 M plus $MgCl_2$ 0.3 M), and NaCl 4.9 M were acquired and are shown in Figure 5.2. Raman and IR spectra of neat water are also included. The presence of high concentration of chloride salts in water in both the Raman and IR spectra clearly reveals a signal enhancement in the ~ 3450 cm^{-1} band (which is referred as the solvation shell). Additionally, this band is shifted ~15 cm^{-1} to a lower frequency in the $MgCl_2$ solution, while the seawater and NaCl solutions reveal a frequency shift to the blue. Raman and IR spectra show a substantial intensity decrease in the low frequency band ~ 3200 cm^{-1} (assigned to strongly hydrogen-bonded water molecules) for all salt solutions, except for the IR spectrum of $MgCl_2$, which shows higher signal intensity than that of water. The difference in the Raman and IR spectra is attributed to the different selection rules of these spectroscopic techniques.[17] So Mg^{2+} presumably increases the strength of the dipole but decreases the polarizability. In summary, the strong hydrogen bonding network of pure water is highly perturbed by the presence of the chloride anions and cations, resulting in an intensity loss of the 3200 cm^{-1} band in the Raman and IR spectra. Meanwhile, there is a rearrangement into solvation shells that results in a weakening of the hydrogen bonded network after the chloride salt addition. This gives rise to an intensity gain and a frequency shift to the ~ 3450 cm^{-1} band. The frequency shifts in this region are consistent with the observed frequency changes in the SFG spectra. In previous Raman spectra of aqueous salt solutions, it is generally reported that as the concentration of the salt increases the intensity of the ~ 3450 cm^{-1} band increases.[10, 17, 42] Additionally, this band shifts to a higher frequency and the bandwidth decreases.[123-127] In the case of different salts the intensity of this peak is associated not only with concentration, but also with size and polarizability of the anion ($I^- > Br^- > Cl^-$).[10, 17, 125, 127]

Historically, the identity of the anion has been related to changes in water spectra (SFG, Raman and IR), although most studies have used monovalent cations. [10, 17, 18, 109, 125, 128]However, very recent publications show that an increase in intensity in the high frequency region (3400 cm^{-1}) accompanied by a decrease in the low frequency region (3200 cm^{-1}) is characteristic of several doubly charged cations such as Mg^{2+}, Ca^{2+}, and Sr^{2+}, lending support to the hypothesis that these changes in intensity are related to strong water-cation interaction. [127, 129]

SFG spectra at air-aqueous interfaces provide information about the interfacial effect of chloride salts on the hydrogen bonding network of water. SFG transition moments are related to the Raman and IR transition moments. [47, 125, 130, 131] Therefore, the intensity enhancement observed in the 3400 cm^{-1} region in the SFG spectra in all chloride salt solutions was somewhat expected. Moreover, the red shift of ~50 cm^{-1} observed in this region of the $MgCl_2$ solution relative to the NaCl solutions was also observed in the Raman and IR spectra as discussed above. The intensity loss in the 3000-3200 cm^{-1} region of the SFG spectrum of the $MgCl_2$ solution, however, cannot be explained by these means and other possible reasons are proposed and discussed later.

The vibrational spectra of salts solutions, particularly the comparison of solutions of divalent salts to monovalent salts and neat water is very complicated. There are effects from the presence of the ions on interruption of the water structure, and effects of the ions on the dipoles and polarizability of the water in the first solvation shell. Additionally, for the case of magnesium is very likely that contributions from additional solvation shells that influence absorption and scattering cross-sections, and overall field effects from the layering of the ions, and other basic selection rules, such as the averaging of net orientation in SFG would have an impact in the resulting SFG signal. Several points needed to be discussed in more detail.

While the signal from 3000 – 3200 cm^{-1} is noticeably less than water for Raman and SFG of the $MgCl_2$ solution, there is an enhancement in signal in the IR spectrum in this region, showing that oscillators vibrating in that frequency range do exist in the solution. In fact, in the $MgCl_2$ solution enhancement is observed for the entire OH stretching region up to 3550 cm^{-1}. The overall increase in intensity of the IR spectrum of aqueous $MgCl_2$ could be due to Mg^{2+} inducing a stronger dipole in water not only in its first solvent shell water molecules, which are somewhat covalently bonded, but to some extent the water molecules beyond this as well. This would be in agreement with the work by Krekeler et al., in which they determined from molecular simulations that Mg^{2+} borrows electron density from the oxygen atoms of the solvating water, giving the first shell water molecules a net charge that is seen by outside water molecules as being a similar charge density to sodium. [132]

Sodium would have a much weaker effect on water dipoles, primarily because it has a lower charge and would likely only affect the first solvation shell of water. However, the formation of ion pairs would not only reduce the number of water molecules sodium interacts with directly by occupying neighbor positions, but it would also reduce the strength of sodium-water interaction. This would be in addition to the added disorder of the water structure from the presence of the ions, which one would naturally expect to cause an increase in the water stretching region around 3450 cm^{-1}, and a decrease at lower frequencies, which is observed. The Raman shifts of aqueous salt solutions is the consequence of strong electric fields exerted by the anion on adjacent hydroxyl groups, but those contributions cancel out in SFG because the solvation of ions tends to be symmetrical.[101] Additionally, differences at the interface result from ion-specific spontaneous layering of charges at the interface.[101]

Another important point involves the surface concentration of cations. Differences in the surface concentration among the solutions are expected. Additionally, each Mg^{2+} is certain to interact directly with 6 water molecules (unlike Na^{+}, which forms contact ion pairs with Cl^{-}), so the water structure surface may be more disrupted than it was in the bulk. In addition, differences in the overall orientation of the water molecules between systems are also expected.

The free OH region, which corresponds to water hydrogen atoms that are not hydrogen bonded or directly interacting with chloride anion or either cation, occurs roughly from 3600 cm^{-1} to 3800 cm^{-1}. The frequency of the free OH is affected by the hydrogen bonding configuration that the bonded OH take.[133] The free OH at 3700 cm^{-1} is mainly attributed to three-coordinate water molecules in neat water[108]although this peak is rather broad and likely contains two-coordinate species at higher frequencies.[111, 134] In the three solutions the intensity of the free OH stretch peak at 3700 cm^{-1} is slightly reduced in comparison with that of neat water.

Generally, the intensity of this peak is used to compare the number of free OH oscillators; however, if the salt present affects the dipoles and polarizability of the water molecule this comparison becomes more complex. Also, differences in the nonresonant background magnitude (see equation 2.6) from each solution could lead to variation in the measured SFG intensity. Additionally, sum frequency intensity is not only proportional to the number density, but also to the orientation of the molecules. Therefore, if the interfacial water molecules change their mean orientation, a difference in the intensity may also be observed for the ssp polarization combination. To determine if the reduction in the ssp intensity was due to a change in the average orientation or a reduction of the free OH oscillators, a molecular orientation analysis was conducted using an additional polarization combination. SFG spectra using ssp and ppp polarization combinations of all the chloride salt solutions were acquired with the SSFG and BBSFG spectrometers and are shown in Figure 5.3a-c, respectively. The ssp polarized SSFG and BBSFG spectra reveal a small reduction in the SFG intensity for all salt solutions compared to that of water. The scanning SFG spectrometer provides slightly improved signal to noise in this spectral region, and we resolve a clearer spectral decrease in the corresponding spectra of Figure 5.3a. (The lower S/N in the BBSFG ssp spectra was a consequence of optimizing the ppp intensity for the BBSFG system.) The ppp polarized BBSFG spectra of $MgCl_2$ and the model seawater solutions show no significant change in the intensity relative to that of neat water. However, the BBSFG ppp spectrum of the NaCl solution reveals a very slight intensity enhancement compared to that of neat water (Figure 5.3c) inferring a possible orientation change. Additionally, in both ssp and ppp polarized BBSFG spectra a small blue shift of the free OH relative to that of water is observed. This blue shift increases from 2 cm^{-1} in the $MgCl_2$ solution to 4 cm^{-1} in the NaCl solution. In the ssp polarized SSFG spectra this blue shift is not as obvious due to the fact that in the SSFG system the infrared frequency is scanned every 5 cm^{-1}. However, as discussed earlier we refrain to assign this shift to a specific interfacial water structure.

Orientational analysis of the SFG free OH stretch peak has been discussed in detail in Chapter 4. In the case of the free OH stretch peak, the orientation angle from neat water is calculated to be 33 ± 2° which is consistent to the value reported by Gan *et al.*[117]The calculated mean orientational angles for the $MgCl_2$ and seawater solutions are within the range of that obtained for neat water. In the case of the NaCl solution the average angle is calculated to be 29°. However, the error associated with the SFG intensity (see error bars of Figure 5.3a and b) reveals that the orientational calculation, which is based upon the intensity ratios, overlaps. Thus, within statistical error, the free OH calculated angles are not differentiable from that of neat water for all of the chloride solutions. Therefore, the reduction in the ssp spectra of Figure 5.3a and b, would seem to point to a small decrease in the free OH number density at the surface of the chloride solutions relative to that from the neat water surface. It is important to note that with lower concentration (1 M) aqueous NaCl solutions, a decrease in free OH peak intensity was not observed.

5. 4 Conclusions

Vibrational spectra of the surface and the bulk of aqueous magnesium chloride, aqueous sodium chloride and model seawater systems were explored. We conclude that magnesium has a strong effect on water structure and electrostatic environment in general, including the interfacial environment. Since chloride experiences less contact ion pairing in the seawater and $MgCl_2$ simulations this may affect its surface reactivity.

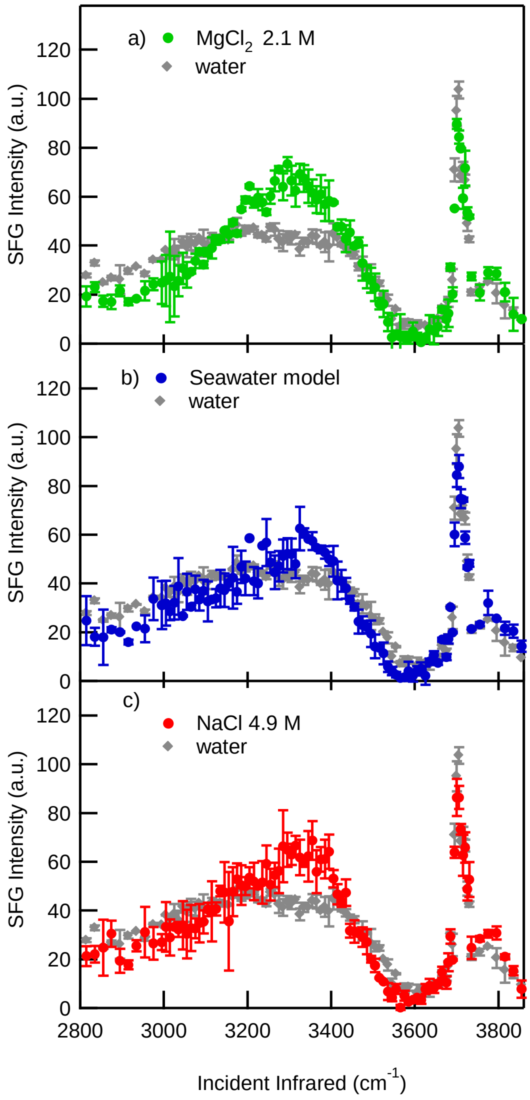

Figure 5.1. Sum frequency spectra of aqueous MgCl$_{2,}$ a model seawater, and NaCl. A spectrum of neat water is provided as a reference in each.

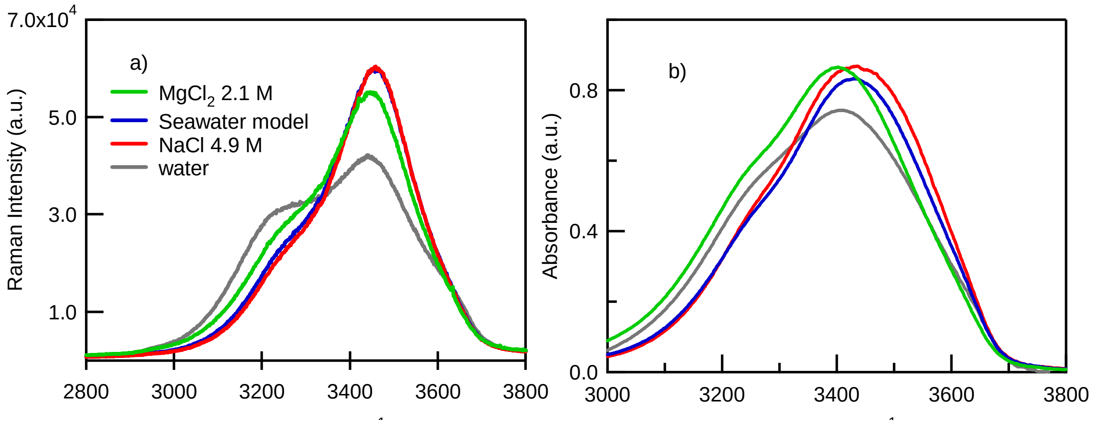

Figure 5.2. a) Raman and b) IR spectra of aqueous solutions of $MgCl_2$, seawater model and NaCl. Neat water spectra are also included.

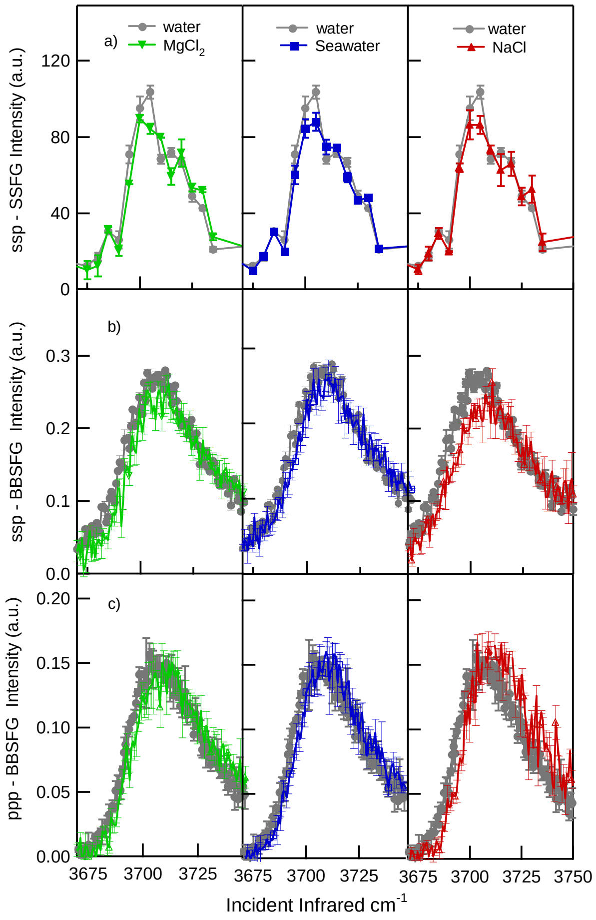

Figure 5.3. Sum frequency spectra of aqueous 2.1 M $MgCl_2$, model seawater (4.5 M of NaCl plus 0.3 M of $MgCl_2$), and 4.9 M NaCl in the free OH region using (a,b) ssp polarization combination for the SSFG and the BBSFG systems, respectively, and (c) ppp polarization combination using the BBSFG system. SFG spectrum of neat water is shown for comparison.

Chapter 6

Silica Hydroxylation

Mineral dust particles originate from windblown soils and deserts are one of the most abundant natural aerosol species. These particles are second in emitted mass only to sea salt. [5]Mineral dust particles serve as cloud condensation nuclei (CCN), thereby influencing the formation and properties of clouds. [30] Anthropogenic activities including land use, coal mining, stone crushing and incineration processes have been reported to contribute to the emission of mineral oxide particles to the atmosphere. REF The study of mineral oxides surfaces exposure to mid-relative humidity values is of atmospheric relevance due to their direct and indirect effects on the surface albedo. [135]These particles also have been related to respiratory distress in humans.

SiO_2 is a major component in earth's crust [55] and consequently is frequently detected in natural and engineered particles. Amorphous silica has been studied extensively [136, 137], including second harmonic spectroscopy studies pioneered by the Eisenthal and Geiger groups [138-141]; however there are few studies at the air-solid interface under ambient conditions with mid-range (~45 %) relative humidity (RH). [45] Silica is fully hydroxylated in water-saturated conditions [142]; yet in non water-saturated conditions (depending on the RH), there are a number of monolayers of water adsorbed on the surface. [137] Surface silanol groups [143]act as adsorption sites for adsorbates capable of undergoing donoracceptor interactions. Thus, surface silanol groups play a key role in sorption processes involving physical (including hydrogen bonding) and chemical bonding forces. The surface charge of a mineral is the consequence of the protonation-deprotonation of surface functional groups, mostly OH. [144] Far from the point of zero charge (PZC) at low or high pH, the surface charge is dependent on the pKa's of the oxide surface in addition to the solution ionic strength and the nature of the electrolyte in the solution. Ong *et al*. [140] studied the silica surface and measured the two pKa's using second harmonic generation. The pH at the point of zero charge (pH_{pzc}) reported for amorphous silica ranges from 2 to 3.5. [136, 145, 146] The surface is positively charged at a $pH < pH_{pzc}$, and negatively charged at a $pH > pH_{pzc}$.

6.1 Materials

Infrared-grade fused (amorphous) silica plates of 1.00 inch diameter and 0.188 inch thickness were obtained from Quartz Plus Inc. All glassware used was cleaned with $(NH_4)_2S_2O_8$ in H_2SO_4 solution (0.08 M) to eliminate trace organics and rinsed with Nanopure water (18.2 MΩ·cm).

The silica plates were annealed in a muffle oven (Fisher Scientific, Isotemp Muffle Furnace) at 900 °C for 12 h to eliminate adsorbed organic substances. They were then cooled to room temperature for 30 min. Then spectra of the air-solid interface were acquired. These spectra are referred to as clean silica. Several silica plates were exposed to the laboratory RH conditions and stirred in water to monitor water (gas and liquid) adsorption prior to spectral acquisition in an open cell. Spectra of the air-solid interface of these silica plates were obtained at different exposure times (vapor adsorption) and after water evaporation. Spectra obtained in this way were highly reproducible.

6. 2 Experimental details

SFG spectra of the air-silica interface were acquired from 2800 to 3900 cm^{-1} using the scanning SFG spectrometer. The free silanol region (~3750 cm^{-1}) was also probed using the broad bandwidth SFG spectrometer. Details of these two SFG systems are described in Chapter 2. The polarization combinations used for the scanning SFG experiments was s, s, and p for the VSFG, 532 nm, and infrared beams respectively. Additional spectra were acquired under ssp and ppp for the free silanol orientation calculation with the broad bandwidth SFG spectrometer. All the spectra were acquired in ~45 min, unless otherwise indicated. The scanning spectra were normalized by the infrared profile, which was detected in real time with the SFG intensity. The broadband spectra were normalized to the nonresonant signal from a GaAs crystal. Power dependence experiments were conducted to ensure that the SFG intensity was linearly correlated to the input energy of the visible and infrared beams. All the spectra were acquired at ~23 °C and at 47 ± 8 % RH.

6.3 Results and Discussion

Water vapor adsorption at the silica surface was investigated at ambient conditions (~40% RH) to monitor the silica hydroxylation. Several spectra series of the air-silica interface exposed to water vapor were acquired as a function of exposure time. In Figure 6.1 and its inset one such series is shown. A strong peak at 3750 cm^{-1} is observed and assigned to the free silanol stretch vibration (≡SiO–H). [147]This peak intensity decreases over time. These results indicate that water vapor molecules interact with the surface silanol groups. The free silanol peak continues to be observed after 72 h (inset of Figure 6.1). Additionally, a small shoulder is observed at ~3735 cm^{-1}, and is attributed to water weakly bound to silanol groups [148], somewhat similar to a "silica-gel" structure. [149]

After 24 h a broad band at 3000–3600 cm^{-1} is also observed and assigned to hydrogen bonded OH stretching modes. The precise assignment within this broad band remains controversial as previously discussed. [7] This region intensity increases with increasing exposure time. The interfacial structure of adsorbed water on a surface can be found by the analysis of the two spectral bands at ~3200 and 3400 cm^{-1} corresponding to the stretching modes of the ordered, and the less ordered hydrogen bonded water, respectively. [23]These bands have also been reported as strongly and weakly hydrogen bonded water molecules, respectively. [23, 150] After 24 h both bands are observed. Further exposure results in an increase in the intensity of only the 3400 cm^{-1} band. Others have observed using FTIR a combination of ordered and disordered layers with a dominance of ordered water on silicon dioxide and oxide surfaces after adsorption of water vapor at ~40% RH. [31, 151]Others, using SFG, also observed a slight dominance of the 3200 cm^{-1} band at neutral pH indicative of an ordered interfacial water structure at the liquid water—silica (and quartz) interface; the ordering was highly dependent on surface ionization and therefore pH. [43, 44]In our study the pH was ~6.5, at which the surface is negatively charged ($pH>pH_{pzc}$), although the majority of the surface groups are expected to be *SiOH* groups.[144]We observe a combination of ordered and disordered hydrogen bonded water after 24 h as shown in Figure 6.1. However, we observe a small enhancement of the 3400 cm^{-1} band after 72 h that suggests disordered hydrogen bonded water molecules are adsorbed with subsequent water exposure. The intensity enhancement of the 3400 cm^{-1} band suggests that water adsorbs to silanol-bound water and forms clusters rather than a uniform film. [137, 152]Adsorption of water to water is more energetically favorable relative to adsorption of water to silica.[153, 154]Cluster formation is typical of surfaces that are partially hydrophobic. [136, 137, 152, 153] This surface structure is rather stable as evidenced by the highly reproducible spectra.

The square root of the VSFG intensity is proportional to the number of oscillators at the interface. The reduction in the free silanol intensity shown in the inset of Figure 6.1 could be assigned to a reduction in the number density if the average orientation of the free silanols is relatively constant over time. To determine the cause of the intensity reduction the ssp and ppp spectra of the free silanol over time were acquired with the broad bandwidth spectrometer and are shown in Figure 6.2. The orientational analysis of other vibrational modes is well documented. [39, 155] Briefly, the ratio of different second order nonlinear polarization tensor elements (χ_{ijk}), in this case ssp ($\chi_{xxz}=\chi_{yyz}$) and ppp (χ_{zzz}, χ_{yyz}, χ_{yzy}, and χ_{zyy}), is related to the mean orientational angle (θ). The bond polarizability used was that reported for the free OH of water ($r = 0.32$). [107]Detection efficiency differences between the *s* and *p* SFG signal were avoided by changing the *p*-SFG signal to *s*-SFG signal with a wave plate. The calculated free silanol average orientation at 3750 cm^{-1} was 26 ± 2° from the surface normal. These free OH groups are more perpendicular oriented to the surface than those free OH from liquid water with an average orientation of 33 ± 2° from the surface normal.

Figure 6.3 shows the relative free silanol percentage as a function of time (h). To determine the free silanol percentage, it was assumed that at time zero (Figures 6.1 and 6.2, “0 h” spectrum) 100% of the silanol groups were free. Error bars show the standard deviation in the calculated percentage from different silica plates. The water adsorption follows two regimes, a fast component (< 20 h) and a linear component (> 20 h). In the fast regime, the formation of clusters occurs. [152]

The 3000–3600 cm^{-1} intensity can be modified by hydroxylation of the siloxane (Si–O–Si) groups. These are generated by the cleaning procedure of the silica plates, which includes heat treatment at 900 ºC in air. The hydroxylation of surface siloxane groups generates an increased number of silanol groups that could subsequently interact with water vapor. Under our experimental conditions, complete hydroxylation to regenerate the initial silica surface is not expected. [156]

To examine further the time dependency of water adsorption to the surface, spectra of the air-silica interface after addition of liquid water (exposure <1 min), and stirring in water (exposure ~30 min) were obtained as shown in Figure 6.4. A clean air-silica spectrum is also shown. Upon liquid water dropwise addition, the spectrum reveals a pronounced decrease of the silanol peak, and an enhancement in the hydrogen bonded OH region (3000–3600 cm^{-1}). This spectrum is similar to the spectra of water vapor adsorption shown in Figure 6.1. The spectrum obtained after stirring in water shows a decrease in the 3650 cm^{-1} region, and an increase in the 3400 cm^{-1} region relative to the water dropwise addition spectrum. The intensity of the 3200 cm^{-1} band in both spectra is similar. As described earlier, the higher intensity of the 3400 cm^{-1} band is the result of the incorporation of more disordered hydrogen bonded water molecules. Both spectra show an increase in the 3650–3740 cm^{-1} region which we assign to water weakly bound to silanol groups and vicinal pairs of isolated silanol. [148, 157]There is also a possible contribution from the free OH stretch of water (observed at 3700 cm^{-1}), water dimers, and weakly hydrogen bonded water. [108, 158] The silica surface hydration evolves over time. In the environment, mineral surfaces tend to hydrolyze resulting in the dissolution of the surface species to form bulk silicic acid and therefore exposing new silicon atoms. [136]

6.4 Conclusions

Vibrational sum frequency generation spectroscopy was used to examine the air-silica interface before, and after adsorption of water in the gas phase and in the liquid phase. Free silanol OH groups are observed after 72 h of exposure to mid RH conditions. Silica hydroxylation from water molecules in the gas phase follows a rapid and slow regime which is characteristic of cluster formation. The free silanol average orientation determined was 26 ± 2° from the surface normal.

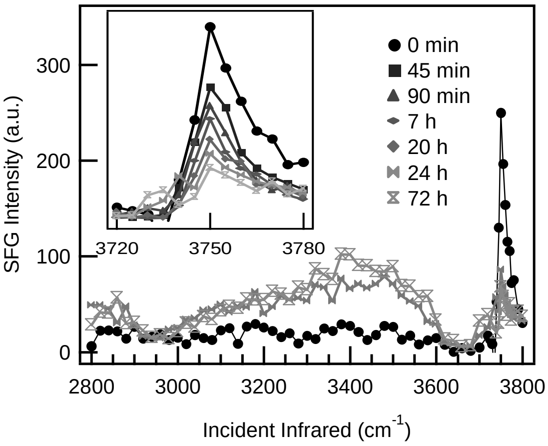

Figure 6.1. SFG spectra of silica at the air-solid interface at time intervals of exposure to ambient conditions (RH ~40%, 23 °C).

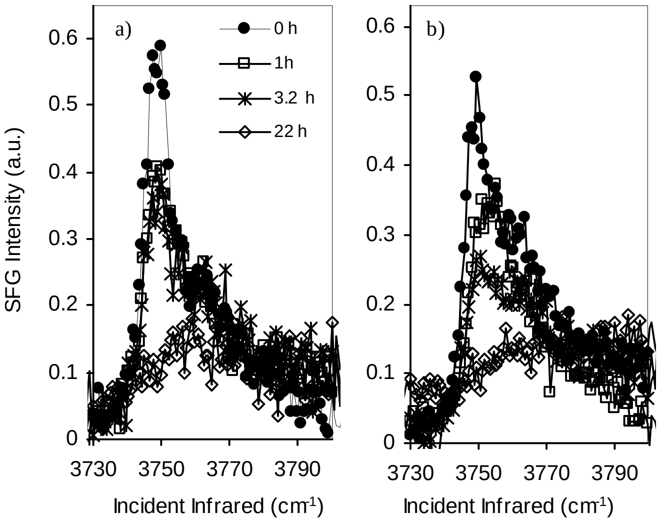

Figure 6.2. a) ssp and b) ppp polarized SFG spectra of silica at the air-solid interface at time intervals to exposure to ambient conditions (RH ~ 44 RH, 23 °C).

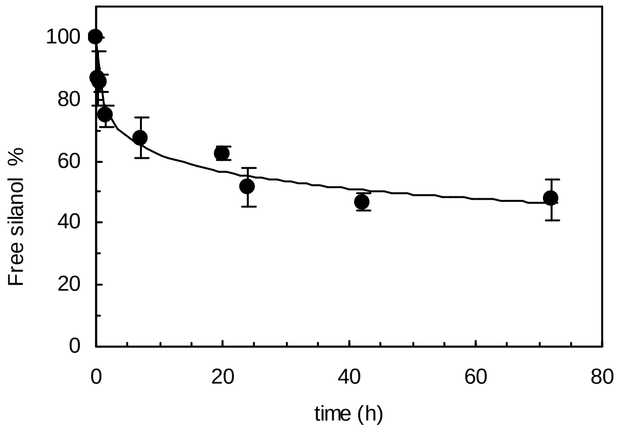

Figure 6.3. Free silanol percentage as a function of time (hours). The error bars are ± 1 standard deviation from the free silanol percentages obtained from different samples.

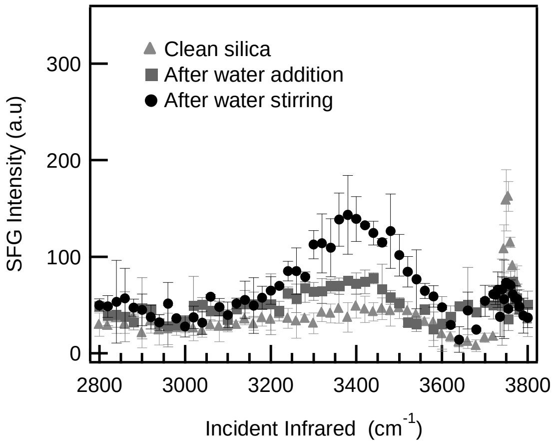

Figure 6.4. SFG spectra of silica at the air-solid interface after liquid water exposure.

Chapter 7

Na^+ *and* Ca^{2+} Effect on the Hydration and Orientation of the Phosphate Group of DPPC at Air−Water and Air−Silica Interfaces

Water is critically important in the functioning of biological molecules and their assemblies including membranes. Water-membrane interfaces play a role in fundamental biochemical functions such as the transport of nutrients, protein synthesis, and DNA replication. [159, 160] Biological membranes consist of a lipid matrix in which membrane proteins are embedded. These lipids, mainly phospholipids in eukaryotic organisms, are charged entities that are surrounded by an aqueous environment containing ionic species. The properties of these membranes are affected by the electrostatic character of their chemical environment, which includes ionic strength and pH. The interactions between phospholipid membranes and ions play a central role in many biological processes such as neural signal transduction [161] and membrane fusion. [162]

Cations are attracted to the carbonyl groups and the PO_2^- of the phosphate group of phospholipids. [163-167] The interaction between acidic lipids and cations is favored according to the Gouy-Chapman theory of the electrical double layer. [168] The interactions of cations with the headgroups of phospholipids are expected to be stronger for negatively charged lipid monolayers such as phosphatidylglycerol compared to those of zwitterionic phosphatidylcholine (PC) monolayers such as dipalmitoylphosphatidylcholine (DPPC). Binding constants of calcium ions to glycerol and PC headgroups were found to be similar in magnitude when corrections for the difference in electric surface potentials were carried out. [169] Moreover, small changes in the headgroup orientation after ion binding was shown to alter the electrical properties of the membrane surface, having an impact on the physiological and biochemical properties of the membrane. [170, 171]

The predominant ions surrounding biological membranes include Na^+, K^+, Ca^{2+}, Mg^{2+} and Cl^-.[172] The interactions between monovalent ions and zwitterionic lipids are generally assumed to be somewhat weak. Yet, the knowledge of the interaction between monovalent ions and phospholipids is less detailed apart from theoretical work. [172-176] Divalent cations such as calcium ions are known to interact strongly with charged lipids, but only moderately with zwitterionic lipids. [177] Although calcium binding to charged and zwitterionic lipids has been previously investigated,[163, 164, 167, 169, 170, 178, 179] it is still not well understood. Spectroscopic molecular investigations of the binding site, the phosphate group, are required to further elucidate the binding event.

As an alternative to studying monolayers at the air-water interface, these same monolayers can be transferred to solid supports at different surface pressures. The interactions between membranes and solid surfaces are the subject of study for several industrial and biomedical processes. For instance, there have been studies in toxicity reduction of pyrite [180], and in cell recognition and adherence. [181] These interactions are also important in cell rupture caused by inhaled mineral dust particles in the lungs. [34]

Crystalline and amorphous SiO_2 particles are notoriously toxic and pose serious risk to human health. [33] The molecular mechanism by which cell membranes degenerate upon adhesion of silica particles to the cell surface is still not well understood.[34, 182, 183]

In this chapter we analyze the macroscopic differences from monolayers of DPPC, the most abundant of the pulmonary surfactants [184], spread on water, NaCl solutions, and $CaCl_2$ solutions using compression isotherms obtained from surface pressure measurements. To study the microscopic differences, a surface selective vibrational spectroscopic technique, sum frequency generation (SFG) spectroscopy, was used to examine the hydration and the orientation of the phosphate group of DPPC monolayers at the air-aqueous interface of these three different subphases. Additionally, in an attempt to elucidate the molecular effect of the adhesion of silica particles to cell membranes, we probed the phosphate group of DPPC monolayers supported on silica as a planar membrane model system. The silica-supported DPPC monolayers were transferred from aqueous subphases containing NaCl and $CaCl_2$. Orientation information of the phosphate group of DPPC monolayers at the air-aqueous and air-silica interfaces was also examined.

7.1 Materials

1,2-dipalmitoyl-*sn*-glycerol-3-phosphocholine (DPPC), with > 99 % purity was obtained from Avanti Polar Lipids Inc. (Alabaster, AL) and used without further purification. Spectral grade acetone and chloroform were purchased from Sigma-Aldrich (PA, USA). Hellmanex II solution was obtained by Hellma Cells, Inc. (Plainview, NY).

Infrared grade fused (amorphous) silica plates of 1.00 inch diameter and 0.188 inch thickness were obtained from Quartz Plus, Inc. (Brookline, NH). All glassware used was cleaned with $(NH_4)_2S_2O_8$ in H_2SO_4 solution (0.08 M) to eliminate trace organics and rinsed with Nanopure water from a Barnstead system with a resistivity of (18.2 MΩ•cm).

Sodium chloride (NaCl; ACS certified) and calcium chloride dihydrate ($CaCl_2 \cdot 2H_2O$; ACS certified) were obtained from Fisher Scientific (Pittsburgh, PA). For the sodium chloride solutions, the NaCl salt was placed in a muffle oven (Fisher Scientific, Isotemp Muffle Furnace) at 700 °C for 4 hours to eliminate any organic contaminants prior to mixing with Nanopure water to obtain the final concentration. For $CaCl_2$, a saturated aqueous solution was prepared and then filtered through a Whatman Carbon-Cap activated carbon filter to remove organic contaminants. The concentration of the filtered $CaCl_2$ solution was determined by the Mohr method.[66] The concentrated $CaCl_2$ solution was then diluted to the final concentration using Nanopure water.

7.2 Experimental details

Substrate cleaning. Amorphous silica plates were cleaned by a series of sonication steps. [185] First, they were sonicated for 15 min in acetone, rinsed in nanopure water, then sonicated for 15 min in 2 % Hellmanex II solution which is an alkaline solution specifically designed to clean quartz cuvettes, then rinsed in nanopure water. Then the plates were sonicated in water for 15 min. Finally, the silica plates were dried in an oven at 70º C for 10 min. Clean silica plates were analyzed by SFG spectroscopy to verify the absence of CH resonances attributed to organic contaminants.

Langmuir Films. The surface pressure-area isotherms were obtained with a KSV minimicro (KSV, Finland) described in detail elsewhere. [39] The procedure followed to obtain the isotherms has been described previously. [39] All the isotherms were collected at 22 ºC± 1.

***Langmuir - Blodgett (LB) Films*.** Langmuir DPPC films were acquired with a minimicro LB-trough from KSV Instruments (Monroe, CT). This trough comprises a dipping well and a linear dipper to transfer the Langmuir film from the water subphase onto the solid substrate. A clean silica plate was clamped onto the dipper and was partially immersed in the dipping well full of the aqueous phase prior to spreading the DPPC film. In the Teflon coated film trough a known volume of a 1 mM solution of DPPC in chloroform was spread dropwise on the surface of the water subphase (pH ~ 6) or aqueous solution. After 10 min to allow for complete solvent evaporation, the compression of the two hydrophilic barriers was initiated. The surface pressure was measured using a Wilhelmy plate composed of Whatman 41 ashless paper. The films were compressed at a constant speed of 5 mm/min. Films were transferred onto the silica substrate by compressing the DPPC film to 40 mN/m followed by withdrawing the silica plate vertically through the interface into the air. The withdrawing speed was 1 mm/min. The surface pressure was maintained at 40 mN/m throughout the deposition process. The temperature for all of the procedures was 22 ºC ± 1. The average transfer ratio measured was ~ 1.03 during the transfer process. This film quality parameter is the ratio of the coated area of the solid substrate to the area occupied by the monolayer on the liquid substrate. [186]Silica coated plates (and uncoated as a control) were analyzed within an hour after film transfer by SFG spectroscopy.

Broad Bandwidth Sum Frequency Generation Spectroscopy. Spectra were obtained under the ssp (s for the SFG, s for the 792 nm, and p for the infrared beam) and ppp polarization combinations. SFG spectra were normalized to the nonresonant signal from a GaAs crystal. Detection efficiency differences between the s and p SFG signal were avoided by changing the p-SFG signal to s-SFG signal with a half wave plate just prior reaching the CCD camera. Spectra calibration was conducted with the absorption bands from a polystyrene film placed in the output port of the OPA when acquiring the nonresonant SFG spectrum of a GaAs crystal. This calibrated SFG system is able to resolve a 1 cm^{-1} peak shift. Fresnel factors are considered in the orientation analysis of the ν_s PO_2^-. An average of at least two replicate spectra is shown in all cases. Spectra were acquired at 22 °C ± 1 and in a range from 30 to 40 % relative humidity.

7.3 Results and Discussion

In our initial studies, DPPC monolayers spread on aqueous solutions with a range in concentration of 0.1 M to 0.5 M of NaCl and $CaCl_2$ were examined. Preliminary results showed that the effect of calcium on the DPPC isotherms was more pronounced than that of sodium. From the aqueous NaCl solutions tested, the greater concentration is presented here to show that even at relatively high concentration of sodium, only a modest effect on the surface organization of phospholipids is observed compared to that of lesser concentrations of calcium.

Isotherms of DPPC

Pressure-area isotherms of Langmuir DPPC monolayers on water, 0.5 M NaCl, and 0.4 M $CaCl_2$ subphases are shown in Figure 7.1. The isotherms reveal distinct phases that have been previously identified. [39, 186] Although differences among the isotherms in Figure 7.1 are observed, with the increase of surface pressure (obtained from the difference between the surface tension of the pure subphase and with the spread monolayer) the liquid expanded (LE), the coexistence regions between LE and liquid condensed (LC) and the pure LC phases are observed on all the subphases. The gas phase (G) is only observed from the water and the NaCl isotherms.

Investigation of the monolayer on the 0.5 M NaCl solution reveals that the isotherm shifts to slightly higher mean molecular areas (MMAs) in both the LE and the LE−LC regions consistent with other studies. [187, 188] The shift has been assigned to the interactions of the sodium ions with the headgroup of the phospholipids inducing disorder in the lipid chains. [187-189] Previously, it has been suggested that the chloride anions are excluded from the headgroup region, particularly around the phosphate group [172, 174, 190], and are therefore not discussed in this analysis.

With calcium ions in the subphase, a more pronounced shift to higher MMA of the DPPC isotherm is observed at all surface pressures, consistent with previous studies. [188] In the LE phase, similar to the DPPC isotherm with sodium ions, this shift could be the result of calcium ions binding to the headgroup of the phospholipids, providing additional surface area for each DPPC molecule. [188] It has been suggested that at higher surface pressures (~ 16 mN/m) 1:1 phospholipid/Ca^{2+} complexes are formed leading to a larger MMA by ~ 4 $Å^2$/lipid. This change in MMA corresponds to the Ca^{2+} ion cross sectional area. [188] Above 16 mN/m the change in MMA is reduced by half (~ 2 $Å^2$/ lipid) suggesting the formation of 2:1 phospholipid/Ca^{2+}complexes. [163, 167, 188]

In comparing the results for the Ca^{2+} and the Na^+ subphases in the LC region, the phospholipid organization is more affected by Ca^{2+} ions than Na^+ ions, consistent with previous findings. [163, 167, 188] Surface charge density of Ca^{2+} is approximately twice that of Na^+ given that the ionic radii of Ca^{2+} and Na^+ are similar (100 and 102 pm). [191] Above 16 mN/m in the LC phase, the isotherm from the NaCl subphase overlaps with the purely water subphase. It could be that the Na^+ ions are being squeezed out from the headgroup region. Contrary to the NaCl subphase isotherm, that of the $CaCl_2$ subphase is clearly shifted to larger MMA suggestive of ionic binding to the headgroup.

DPPC monolayers at air-aqueous interface

Molecular level information of the interaction and binding of the cations with the phospholipid phosphate headgroups was obtained with SFG spectroscopy. Phosphate groups are likely the most hydrated moiety of the phospholipid molecule within the monolayer. Water molecules also interact with the carbonyl groups. [192-194] The water molecules that solvate these groups form strong hydrogen bonds. [166, 195-197] Therefore a direct interaction of the cations with the phosphate groups would require the removal one or more of these solvating water molecules from the cation and the phosphate group. The ability of these ions to lose a portion of their solvation shell ultimately determines the strength of the ion-phosphate interaction.

To elucidate the extent of the cation-phosphate interaction, SFG spectra were obtained from the phosphate group of DPPC monolayers in the presence of sodium and calcium chloride salts. SFG spectra of DPPC monolayers on water, 0.5 M NaCl, and 0.4 M $CaCl_2$ at three surface pressures 4 mN/m, 12 mN/m, and 40 mN/m phases are shown in Figure 7.2 a, b, and c, respectively. These spectra were acquired under the ssp polarization combination. The phases of the DPPC monolayer correspond to the LE at 4 mN/m and to the LC at 12 mN/m and 40 mN/m as shown in Figure 7.1. Two peaks at ~ 1070 cm^{-1} and 1100 cm^{-1} are observed in all the spectra and are assigned to the phosphate ester stretch C−OP and the symmetric stretch of the PO_2^- (ν_s PO_2^-) respectively. [198, 199] The ν_s PO_2^- peak is clearly asymmetric towards the low frequency side, suggesting a third component peak at ~ 1090 cm^{-1} which is assigned to the vibration of the R−O−P−O−R. [200]

After compression from 4 mN/m to 40 mN/m of the DPPC monolayers on the three different subphases, a ~ 2 cm^{-1} blue shift of the C−OP and the R−O−P−O−R peaks is observed. A significantly larger blue shift of the ν_s PO_2^- peak at ~1100 cm^{-1} is observed upon compression; yet the extent of this frequency shift is highly dependent on the subphase composition. The blue shift of all these peaks is generally attributed to a difference in the hydration state of the phosphate group from different surface pressures. The smaller shift in frequency observed in the C−OP and the R−O−P−O−R peaks relative to that observed in the ν_s PO_2^- peak is attributed to the fact that the former moieties are solvated more weakly than the PO_2^- moiety. [166] Therefore, to follow the hydration state and ion coordination of the phosphate group in DPPC monolayers we focus our discussion on the ν_s PO_2^- peak at ~1100 cm^{-1}. Detailed analysis of these spectra from the DPPC monolayers of the three different subphases is described below and spectral data is summarized in Table 7.1.

On water, the compression of the DPPC monolayer from 4 mN/m to12 mN/m results in a blue shift of the ν_s PO_2^- peak from 1098 cm^{-1} to 1103 cm^{-1}. Further monolayer compression to 40 mN/m results in an additional frequency shift to 1104 cm^{-1}. This blue shift has been previously attributed to a difference in the hydration state of the phosphate moiety in different structural phases (LE vs. LC), where a blue shift is synonymous with dehydration. [39] The reorganization and resultant dehydration of the phosphate has been commonly referred to as a squeezing out of the water molecules. In the LE phase the loosely packed phosphate groups of the DPPC molecules are well solvated; however as the DPPC molecules are compressed to the LC phase the water molecules of the phosphate's hydration shell reorganize and decrease in number and, hence, dehydration of the phosphate group occurs. Even within the LC phase (at 12 and 40 mN/m), different hydration states of the phosphate are observed. This is due to the fact that at 12mN/m the DPPC molecules are not totally condensed since further compression of the monolayer is possible. A shift in frequency attributed to a change in the hydration state of the phosphate moiety has also been reported in IR spectroscopic studies of DPPC. [201-203] From the perspective of hydration, theoretical studies of the PO_2^- moiety of methylphosphocholine have shown that upon hydration there is a loss of electron density of the P−O bonds due to strong hyperconjugation with the O−H antibonding orbital of water that then weakens the P−O bond resulting in a red shift. [204] This finding is consistent with our compression studies showing a blue shift with dehydration. In addition to the shift, we also observe a change in the full width half maximum (FWHM) of the ν_s PO_2^- peak, which decreases as a result of the monolayer compression. From peak fitting, the FWHM of the ν_s PO_2^- peak at 4 mN/m, 12m N/m, and 40m N/m is determined to be 40 cm^{-1}, 36 cm^{-1}, and 34 cm^{-1}, respectively.

In the presence of sodium in the aqueous subphase (0.5 M NaCl), SFG spectra obtained upon compression of the DPPC monolayer also reveals shifts of similar magnitude to the water subphase spectra. Therefore, it is likely that in addition to dehydration, the sodium ions are not affecting the electronic structure of the phosphate moiety to a significant extent, suggesting that the ions are not binding strongly to the PO_2. However, upon examination of the FWHM, we observe significant differences for the spectra of aqueous sodium vs. purely water subphases. Unlike on the water subphase where narrowing of the spectra is observed with compression, the FWHM of the ν_s PO_2^- peak remains constant at ~ 44 cm^{-1}, indicating a broader distribution of solvation environments for the sodium subphase monolayers. This may be also due to a broader distribution of the orientation of the phosphate moieties in the presence of sodium as well as to vibrational relaxation effects and therefore changes in the lifetime of the transition. Although we do not observe a frequency shift with sodium, the significant changes in the FWHM indicate that sodium ions do perturb the phosphate group and therefore the monolayer. This perturbation may include an alteration of the ordered water molecules adjacent to the DPPC headgroup [205] due to the concentration gradient of ions [172, 174, 190] near the DPPC monolayer.

The findings presented in this study are consistent with recent molecular dynamics studies of DPPC bilayers that have shown that sodium interacts with the phosphate group creating complexes with several DPPC molecules at surface pressures of ~ 10 mN/m. [174-176] It has been suggested that the sodium ions lose part of their first solvation shell water molecules to interact with the unperturbed hydrated phosphate group. [174-176] However, the binding constants of Na^+ and Cl^- to the phosphate and choline group have been estimated to be relatively weak in a range from 0.15 M^{-1} to 0.61 M^{-1} for sodium and 0.16 M^{-1} to 0.28 M^{-1} for chloride [174, 206, 207] , suggesting ion exclusion at high surface pressures.

In brief, from the studies presented here, the presence of sodium chloride in the subphase causes a perturbation of the phosphate group of the DPPC monolayers. At lower surface pressures binding of the sodium ion to the phosphate group is suggested. As the DPPC monolayer is compressed the interaction of the water molecules and the sodium ions with the phosphate group is weakened, and a slight perturbation of the phosphate group is observed.

The SFG spectra of the DPPC monolayer in the presence of calcium (0.4 M $CaCl_2$) are remarkably different than those observed in the absence of ions (neat water) and in the presence of sodium as shown in Figure 7.2. The hydration environment of the phosphate moiety is affected by the monolayer organization in different structural phases, and also by the binding of calcium to the phosphate group. In the LE phase as shown in Figure 2a, a similar peak position of the ν_s PO_2^- peak is observed from all the subphases, although clear differences in the FWHM are revealed. With calcium present, the larger FWHM of the ν_s PO_2^- peak is partially assigned to calcium ions binding to the phosphate group. Upon compression of the DPPC monolayer to 12 mN/m in the presence of calcium, the ν_s PO_2^- peak is ~ 6 cm^{-1} blue shifted with respect to the peaks observed in water and in the presence of sodium. This suggests that calcium binding results in phosphate group dehydration. This is consistent with exclusion of the water molecules from both the phosphate group and the calcium hydrate upon binding. [209] This is in stark contrast to the sodium cations that bind to hydrated phosphate groups, as shown here and discussed by others. [174-176] The stronger attraction between calcium and the phosphate groups compared to that between sodium and the phosphate groups is consistent with the reported binding constants for these ions to the phosphatidylcholine groups. The binding constant for calcium was estimated to be in a range from 12 M^{-1} to 37 M^{-1} [169, 170, 206], which is two orders of magnitude larger than that reported for sodium (see above). At higher surface pressure (40 mN/m) the ν_s PO_2^- peak is 2 cm^{-1} blue shifted relative to that obtained at 12 mN/m suggesting a larger exclusion of water molecules from the phosphate group as more calcium ions are bound. These results are in agreement with previous reports that suggest that the binding constant of calcium ions to the phosphate moiety is sensitive to the phase state of the lipid bilayers in the order of gel state > pretransition state > liquid state. [208]

Larger FWHM values of the ν_s PO_2^- peaks compared to those on water and with sodium present were calculated at all surface pressures. With calcium present, the FWHM of the ν_s PO_2^- peak changes from 53 cm^{-1} in the LE phase to 61 cm^{-1} in the LC phase at 12 mN/m and 40 mN/m as observed in Figure 2. These larger FWHM are partially attributed to a broader distribution of the orientation of the phosphate group in all phases upon calcium binding.

The observed spectral blue shift of the ν_s PO_2^- peak is consistent with theoretical studies on dimethyl phosphates in the presence of water and calcium that have shown that as the calcium cation approaches the anionic oxygens, a blue shift of both the symmetric and antisymmetric modes of the PO_2^- is observed. [209] The internal geometry of dimethyl and dihydrogen phosphates has been reported to be sensitive to the counterion position. [210] Then it is expected that upon direct calcium binding the symmetry of the phosphate group is modified to some degree. This argument could also be applied when sodium ions are present in the subphase; however the extent of this perturbation is expected to be smaller because water molecules mediate the coordination between the phosphate group and the sodium ions.

The hydration environment of the phosphate group may be also affected by the calcium concentration available in the subphase. In Figure 7.3, the SFG spectra of the DPPC monolayers at 40 mN/m in the presence of 0.1 M and 0.4 M $CaCl_2$ in the subphase are shown. The SFG spectra of a DPPC monolayer spread on water is also shown for reference. These spectra reveal that as the Ca^{2+} concentration increases a larger blue shift of the ν_s PO_2^- peak is observed. This suggests that a larger number of the phosphate groups are bound to Ca^{2+} with the increased availability of Ca^{2+} in the aqueous phase. Also observed is a difference in the signal intensity of the ν_s PO_2^- peak in both calcium solutions relative to the purely water subphase. This intensity decrease is likely due to a convolution of two factors: a change in the average orientation of the phosphate group as Ca^{2+} cations are bound, and a variation of the extinction coefficient of the PO_2^- group when the PO_2^-−Ca complex is formed.

In the analysis of the spectra presented in Figures 7.2 and 7.3, a clear increase in the signal intensity is observed as the DPPC monolayers are compressed in all the three subphases. However, sum frequency intensity is proportional not only to the number density (N^2), but also to the mean molecular orientation. Below, the orientation of the phosphate group of a DPPC monolayer spread on neat water in the LC phase is analyzed in detail.

The orientation of the DPPC phosphocholine headgroup, which is related to the structure of the interfacial phospholipid monolayer, has been the subject of study in previous reports. [167, 174, 176, 211-216] Nonetheless, these studies are mainly theoretical efforts. Because of the lack of experimental techniques able to determine the headgroup orientation, there is a dearth of experimental evidence to support or refute the theoretical data. An SFG polarization study could offer headgroup orientation because of its capability of providing quantitative orientation values given certain theoretical treatments. To this aim the ppp polarized spectra of a DPPC monolayer on water at 40 mN/m surface pressure was obtained in the phosphate region (~ 1100 cm^{-1}) after an improvement of the IR energy output and a modification in the geometrical configuration of the input laser beams. This SFG ppp spectrum, and under the ssp polarization for reference, are shown in Figure 7.4.

The experimentally measured SFG intensity in different polarization combinations is related to macroscopic orientational average $\chi_v^{(2)}$, through the microscopic molecular polarizability tensor beta β_v (as shown in Eq. 2.8) and the symmetry of the group. The PO_2^- moiety on the DPPC headgroup can be treated as having C_{2v} symmetry. Hence the macroscopic susceptibilities in ssp and ppp polarization combinations are expressed as follows [130]:

$$\chi_{xxz} = \chi_{yyz}$$

$$\begin{aligned} &= \frac{1}{2}N[(\cos^2\psi)\beta_{aac} + (\sin^2\psi)\beta_{bbc} + \beta_{ccc}](\cos\theta) \\ &+ \frac{1}{2}N[(\sin^2\psi)\beta_{aac} + (\cos^2\psi)\beta_{bbc} - \beta_{ccc}](\cos^3\theta) \end{aligned}$$

$$\begin{aligned} \chi_{zzz} &= N[(\sin^2\psi)\beta_{aac} + (\cos^2\psi)\beta_{bbc}](\cos\theta) \\ &- N[(\sin^2\psi)\beta_{aac} + (\cos^2\psi)\beta_{bbc} - \beta_{ccc}](\cos^3\theta) \end{aligned} \tag{7.1}$$

θ is the average tilt angle of PO_2^- group to the surface normal, ψ is the average twist angle of the PO_2^- group about its molecular *c* axis as shown in Figure 5a. When the PO_2^- group is allowed to rotate about its *c* axis freely, the value of $<\sin^2\psi>$ and $<\cos^2\psi>$ can be integrated to 1/2. In many cases, as here in the DPPC headgroup, this rotation is hindered and therefore the value of twist angle needs to be assumed. In the present study, the value of ψ is assumed to be zero.

Given the value of molecular polarizability tensors, the average orientation of the PO_2^- group is obtained through the SFG intensity ratio of ssp to ppp. Previous SFG studies have demonstrated that the ratio of β can be determined through the experimentally measured Raman depolarization ratio ρ. For C_{2V} symmetry, it is described by:

$$\rho = \frac{3}{4 + 20\dfrac{(1+2r)^2}{(1-r)^2(1+3\cos^2\tau)}} \tag{7.2}$$

Where r is the single bond polarization derivative ratio and τ is the angle between the two bonds (angle O−P−O) in C_{2V} symmetry. Based on bond polarization derivative ratio model, the ratio of β can be expressed as:

$$\frac{\beta_{aac}}{\beta_{ccc}} = \frac{(1+r)-(1-r)\cos\tau}{(1+r)+(1-r)\cos\tau}$$

$$\frac{\beta_{bbc}}{\beta_{ccc}} = \frac{2r}{(1+r)+(1-r)\cos\tau} \tag{7.3}$$

With the value of the measured Raman depolarization ratio 0.05 with a τ of 120° reported for dimethyl phosphate [217], we calculate the ratio of the molecular polarizability tensors, hence the average tilt angle, θ, of PO_2^- was obtained. The calculated tilt angle of the PO_2^- of DPPC monolayers in the water surface is found to be 63° ± 3° from the surface normal. A variation of ± 10% of the Raman depolarization ratio (RDR) value leads to a change in the tilt angle of the PO_2^- of ± 8% showing the sensitivity of the tilt angle to the RDR used. Our tilt angle value is in reasonable agreement with previous results from IR studies of DPPC bilayers that reported 56°. [199, 218] SFG studies of bilayers of DSPC (distearoyl-*sn*-glycero-3-phosphocholine) on D_2O have determined the tilt angle of the choline group, specifically, the angle of $N-(CH_3)_3^+$ to be 66° ± 4° with respect to the surface normal. [219] With this tilt angle value and the values of the angles reported for the P−O, O−C, C−C, [204] the tilt angle of the PO_2^- of the phosphocholine group was determined to be 70º to78º which is also in good agreement to the estimated value reported here.

In the presence of sodium and other divalent cations, the angle of O−P−O in dimethyl and dihydrogen phosphates is affected [210], similar changes would be expected in the phosphate moiety of DPPC. As shown in equations 7.2 and 7.3, a variation in τ would have an impact in the determination of the PO_2^- tilt angle. However, if one assumes that the change in τ is negligible, and that the symmetry of the phosphate group has not been modified, the PO_2^- tilt angle of DPPC on the salt solutions can be determined as was done here from the spectra shown in Figure 7.4b and 7.4c. The PO_2^- tilt angle on the sodium subphase was calculated from the surface normal to be 66º ± 3º as compared to that on water, 63 º ± 3º. However, the calculation for DPPC on the $CaCl_2$ solution did not provide a physically reasonable ratio, confirming that the assumptions in this case were flawed.

The orientation of the headgroup of phosphatidylcholine is usually referred to as the angle between the vector connecting the phosphorus atom and the nitrogen atom (P−N vector, Figure 5b) with respect to the surface normal. [167, 174, 176, 212-216] Theoretical studies of DPPC bilayers have shown that the angle of the P−N vector changes in the presence of halide salts compared to that in pure water. [167, 172, 216, 220] Calcium ions were shown to have a larger effect on the angle of the P−N leading to smaller angles. In general, the presence of both sodium and calcium ions leads the P−N vector to lie more outward from the membrane (smaller angles from the surface normal). Although the PO_2^- tilt angle, as calculated here, provides information on the DPPC headgroup, the headgroup itself is better described by the P-N vector. Additionally, changes in the conformation of the headgroups of DPPC bilayers and monolayers have been described in theoretical and experimental studies in different phases. [211, 215] These studies have shown that the P-N dipole of the DPPC headgroup exhibits an in-plane orientation with respect to the monolayer in the LE phase (liquid crystal in the bilayer), and a more tilted orientation is found in the LC phase (gel phase in the bilayer).

DPPC monolayers at air-silica interface

To examine the interactions of the headgroup of DPPC monolayers with the silica surface, Langmuir-Blodgett (LB) films deposited on amorphous silica were obtained and then analyzed by SFG spectroscopy. SFG spectra of the air-silica interface after the deposition of DPPC monolayers in the phosphate region were acquired under the ssp polarization combination and are shown in Figure 7.6. These DPPC films were transferred at a surface pressure of 40mN/m from water, 0.5 M NaCl, and 0.4 M $CaCl_2$ subphases.

Similarly to the air-aqueous SFG spectra shown in Figure 7.2c, the SFG spectra at the air-silica interface in Figure 7.6 reveal three main peaks which have spectral positions that are highly dependent on the composition of the subphase where the monolayers were transferred from. Spectra from clean silica plates were also acquired (spectra not shown) as control experiments and no SFG signal was detected.

In the SFG spectra from the silica-supported DPPC monolayer transferred from a water subphase, the C−OP and the R−O−P−O−R peaks are observed at 1073 cm^{-1} and 1090 cm^{-}

^{1}, respectively. These peak positions are almost identical to those obtained from the water subphase at 40 mN/m (Figure 7.2c) at 1072 cm^{-1} and 1090 cm^{-1}. The ν_S PO_2^- peak is found at 1106 cm^{-1} which is 2 cm^{-1} blue shifted relative to that on water suggesting a slightly different hydration state of the phosphate group of DPPC at the silica surface; the peak position from aqueous sodium/silica versus aqueous sodium is the same. Whereas the peak position differs by 9 cm^{-1} for the aqueous calcium/silica (1120 cm^{-1}) versus the aqueous calcium (1111 cm^{-1}) subphases. Also different are the FWHM values of the PO_2^- peak from the silica-supported DPPC monolayers where the FWHM value is 10 – 35 cm^{-1} smaller than that found on the aqueous subphases when going from the water/silica to the aqueous calcium/silica subphases, indicating a different hydration environment of the phosphate group and possibly a narrowing of the orientation distribution on the silica-supported subphases. Although, differences in the signal intensity of the PO_2^- peak in the aqueous and solid support are observed, this is likely due to differences in the Fresnel factors of both surfaces. Organization of the alkyl chains in both the water subphase and the silica substrate revealed minimal differences at this surface pressure (spectra not shown). To summarize, as shown by the peak position and the FWHM values, the phosphate moiety of DPPC is significantly affected by the presence of the silica surface.

As previously described, the phosphocholine head group is sensitive to the electric surface charge and dipole fields. [171] The surface charge on silica emanates from the protonation-deprotonation of surface silanol groups and has already been studied in great detail. [136, 137] The pH at the point of zero charge (pH_{pzc}) reported for amorphous silica ranges from 2 to 3.5 [136, 221] Therefore, the amorphous silica surface is negatively charged under the experimental condition of this study since the water pH > pHpzc. Even on a negatively charged surface the majority of the surface groups expected are the neutral silanol groups, that is, Si−OH. [144] Precisely, these silanol groups could form hydrogen bonds with the phosphate groups causing a perturbation of the hydration environment of the phosphate moiety seen as a blue shift of the ν_s PO_2^- peak. This hydrogen bond formation has been previously suggested by Chunbo et al. in NMR studies of DPPC liposomes and silica particles. [222] Yet for the formation of these hydrogen bonds, it is the water molecules present between the silica surface and the headgroup of DPPC [223, 224] that are responsible for maintaining the membrane fluidity in solid supported systems [225] that would need to be displaced.

At this near-neutral pH, there is a relative absence of orientational order of water molecules induced by the surface charge of silica as shown by our earlier work [226] and by others [41, 43, 44] The dipole potential of the headgroup of the DPPC molecules leads to an ordering of adjacent water molecules. [205] Consequently, the trapped thin water layer is likely to be highly structured which can alter the headgroup hydration (studies are underway in our laboratory). [227] In fact, recent molecular dynamics simulations of 1-palmitoyl-2-oleoyl-*sn*-glycero-3-phosphocholine (POPC) bilayers interacting with amorphous silica have shown that this water layer lacks bulk like properties, and is thin enough to consist only of bound waters hydrating the lipid head groups and the hydrophilic silica surface. [35] Then the interaction of the phosphate group of the DPPC monolayers with the silica surface take place through highly structured water molecules adjacent to the silica surface leading to a relatively dehydrated headgroup.

The interaction of the silica surface with the headgroup of DPPC could also involve electrostatic interactions between the positively charged choline groups with negatively charged Si−O$^-$ groups. Studies of bulk adsorption isotherms of DPPC vesicles on quartz at 55 ºC have suggested that the electrostatic interactions between these groups are negligible compared to interaction between the phosphate group and the silica surface. [228] This was attributed to the lower positive charge density associated to the choline group compared to the negative charge density associated to the phosphate moiety. [228] The lipid adsorption affinity to the silica surface is not modified or altered by the phase of the lipid. [229] NMR studies have reported that the choline group mobility of DPPC decreases after interacting with quartz [230] suggesting a weak electrostatic interaction between the quartz surface and the headgroup of DPPC.

In the presence of sodium (Figure 7.6), the SFG spectrum of the silica-supported DPPC monolayer shows an identical spectral position of the C−OP and the R−O−P−O−R peaks as those of the DPPC monolayer transferred from a water subphase. As stated above, the ν_s PO_2^- peak is found at 1104 cm^{-1} which is 2 cm^{-1} red shifted relative to that from water, and the FWHM of the ν_s PO_2^- peak in the presence of sodium is ~ 10 cm^{-1} smaller than that found from a water subphase suggesting a perturbation of the phosphate group in the presence of sodium as previously observed in the aqueous subphases (Figure 7.2). The sodium ions are known to interact electrostatically with the negatively charged Si−O$^-$ groups [231] screening its surface charge, and also promoting negative surface charge density by deprotonating the Si−OH groups. [232] Induced orientational order of water molecules near the silica surface in the presence of NaCl has been reported at the pH of these studies. [233, 234] As discussed above, the headgroup dipole potential leads to an ordering of the solvating water molecules. [205] As a result, the trapped thin aqueous layer between the silica surface and the headgroup of the DPPC monolayer is likely to be structured as described for the case in the absence of salts. Interestingly the ν_s PO_2^- peak in the silica supported monolayer exhibits the same spectral position as that found in the 0.5 M NaCl solution subphase (Figure 7.2c), suggesting a similar hydration environment of the phosphate group. It is suggested that in general the phosphate group hydration is not strongly affected by the surface charge of the silica surface in the presence of sodium ions.

The SFG spectrum of the silica supported DPPC monolayer in the presence of calcium ions reveals similar peak positions of the C−OP and the R−O−P−O−R peaks as those found in the absence of ions (pure water/silica subphase, Figure 7.6). The PO_2^- peak however reveals a significant blue shift of 12 cm^{-1} relative to that found on pure water/silica. This peak is 9 cm^{-1} blue shifted relative to that found from the 0.4 M $CaCl_2$ subphase (Figure 7.2c), suggesting a different hydration environment of the phosphate moiety in both subphases (aqueous Ca^{2+} vs. aqueous Ca^{2+}/silica). Differences in the FWHM values in the presence of calcium and in neat water are observed on the silica supported DPPC monolayers, as observe in the case of the aqueous solutions (Figure 7.2). Similar to the case of sodium, water orientation near the silica surface and promotion of the negative surface charge density are expected when calcium ions are present. [232, 235] This surface charge increment is greater compared to that induced by sodium, [232], consequently the induced order of the water molecules by the surface charge is expected to be greater. Upon calcium binding to the phosphate groups the zwitterionic nature of the DPPC molecules is perturbed and the generation of a positive charge is expected on the monolayer surface, similar to the increase in the zeta potential observed on DPPC liposomes studies in the presence of calcium. [206] The water layer hydrating the silica surface, the headgroups and the calcium ions, is believed to be more structured than that observed in the presence of sodium ions and in the absence of ions is consistent with our work (SFG spectra not shown). This results in dehydrated phosphate moieties in the proximity of the silica surface under these experimental conditions.

Orientation of the PO_2^- moiety of the headgroup of silica supported DPPC monolayers was obtained using the SFG intensity ratio of ssp to ppp as previously described. SFG spectra of a silica-supported DPPC monolayer are shown in Figure 7.7. The refractive indices of silica at 1100 cm^{-1}, 795 nm, and 731 mn were obtained from the literature. [236] The calculated average tilt angle from the surface normal of the PO_2^- of DPPC monolayers supported on silica is found to be 74º ± 3º which is 11º larger than that from the water subphase. This indicates that the PO_2^- vector is oriented more in the plane of the silica surface when the DPPC monolayer is supported on that surface. As indicated above, by making assumptions, in the case of the aqueous Na^+/silica and the Ca^{2+}/silica subphases, the PO_2^- tilt angle is calculated to be 49º and 26º, respectively. The calculation from the intensity ratio from the Ca^{2+}/silica subphase produced a physically reasonable tilt angle, in contrast to the aqueous Ca^{2+} subphase. Because of the assumptions made, we are cautious about these estimated numbers; however, the change in PO_2^- tilt angle from water/silica to aqueous Na^+/silica to aqueous Ca^{2+}/silica subphases is consistent with the picture of more and more ions being bound to the phosphate moiety, modifying the PO_2^- tilt angle relative to the surface normal.

Differences in the orientation angle of the $N-(CH_3)_3^+$ of the choline group of 1,2-distearoyl-*sn*-glycero-3-phosphocholine (DSPC) bilayers in contact with the silica surface and in contact with the aqueous phase have been reported by Liu et al. [219] In the Liu study the choline group vector was shown to be oriented more in the bilayer plane when the DSPC bilayer was in contact with the silica surface. Additionally, other effects have been described in computational studies. For instance, ab initio calculations performed by Murashov et al [237] revealed that dihydrogen and dimethyl phosphate anions show a reduction of the COPO torsion angle upon coordination with orthosilicic acid. Also molecular dynamic simulation of 1-palmitoyl-2-oleoyl-*sn*-glycero-3-phosphocholine (POPC) bilayers showed that diffusion of lipids in the monolayer having direct contact with the silica surface is substantially reduced even under conditions where no structural change of the alkyl chains is observed. [35] The same conclusion was drawn from NMR studies of DPPC bilayers supported on silica. [238] From the studies presented here, we find that that both the hydration environment and the orientation of the phosphate moiety of a DPPC monolayer is affected considerably at the silica surface compared to that in contact with the aqueous subphase.

7.4 Conclusions

Results from hydration and orientation studies of the phosphate moiety from DPPC monolayers on water, aqueous Na^+, and aqueous Ca^{2+} subphases were compared to each other and to studies from DPPC monolayers on water/silica, aqueous Na^+/silica, and aqueous Ca^{2+}/silica subphases. The PO_2^- moiety from the DPPC headgroup was observed to undergo dehydration with increasing surface pressure and additional dehydration environments from the interactions with Na^+ and Ca^{2+} ions. Ca^{2+} was observed to bind effectively to the PO_2^- of the phosphate group for the purely aqueous and the aqueous/silica studies, although Na^+ also showed some evidence of binding. Significant differences in FWHM from the spectra of the hydrated silica surface were observed, revealing varied hydration environments in the silica supported systems, particularly in the case of the aqueous Ca^{2+}/silica subphase. Moreover, the larger differences in the PO_2^- tilt angles from the water and aqueous salt versus the water/silica and the aqueous salt/silica subphases reveal influence of the silica support Modified strongly by the presence of salt. This finding additionally provides information that may be relevant with respect to understanding the pathogenicity of silica in pulmonary systems.

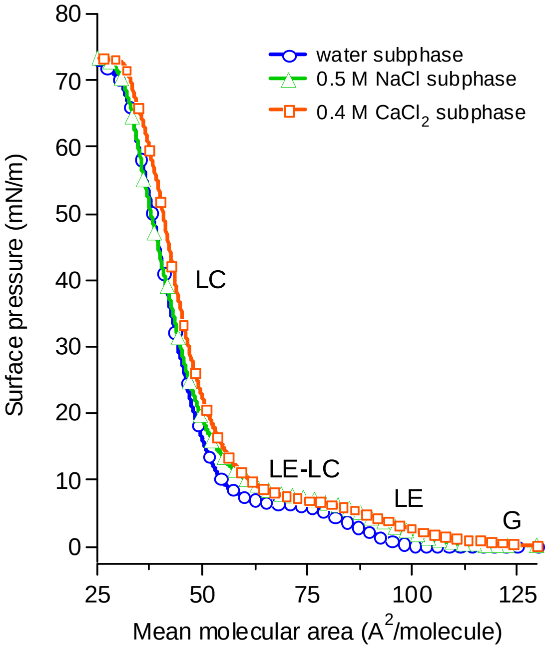

Figure 7.1. Pressure-area isotherm of DDPC on different subphases; neat water (blue), 0. 5 M NaCl (green) and 0.4 M CaCl$_2$ (orange).

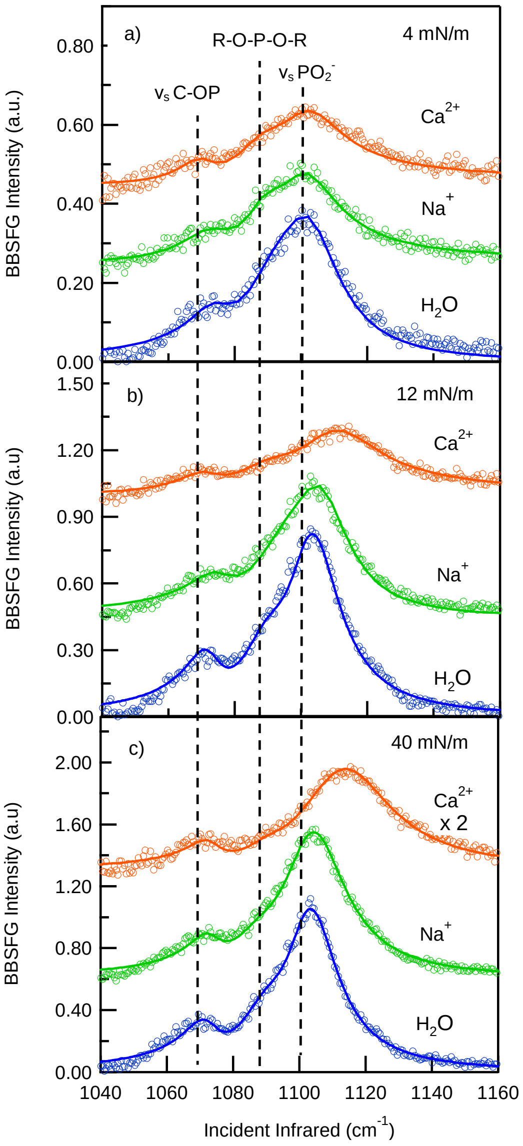

Figure 7.2. SFG spectra of DPPC monolayers on 0.4 M $CaCl_2$, 0.5 M NaCl and neat water subphases at a) 4 mN/m (LE phase), b) 12 mN/m (LC phase) and c) 40 mN/m (LC phase) surface pressures.

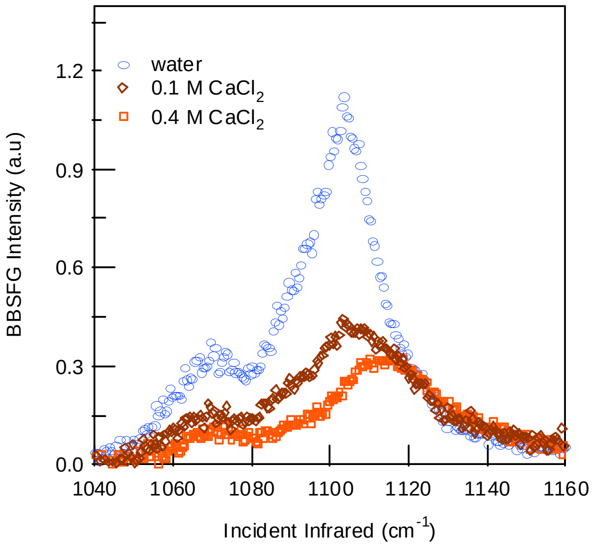

Figure 7.3. SFG spectra of DPPC monolayers on 0.1 M and 0.4 M $CaCl_2$ obtained at 40 mN/m. SFG spectra of a DPPC monolayer on water at 40 mN/m is also shown for reference.

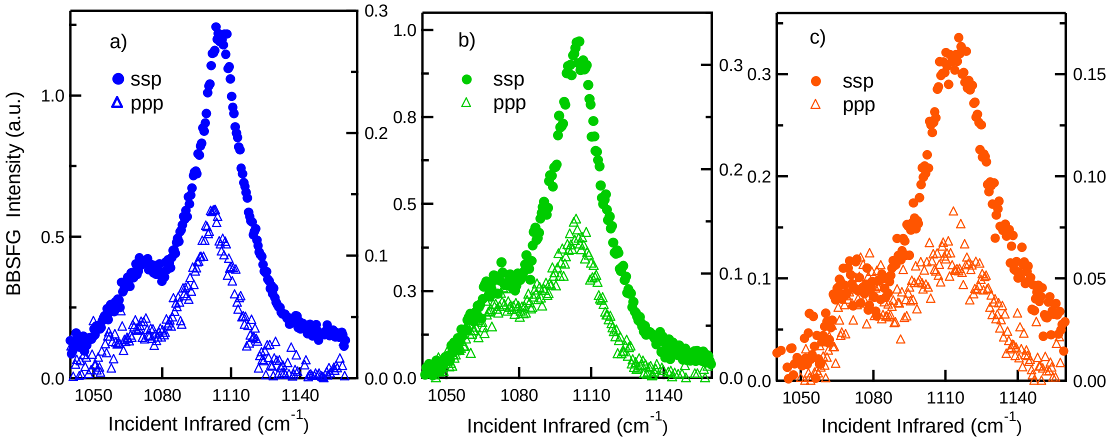

Figure 7.4. SFG spectra under ssp and ppp polarization combinations of DPPC monolayers on a)water, b)).5 M NaCl, and c) 0.4 M $CaCl_2$ subphases at 40 mN/m surface pressure (LC phase).

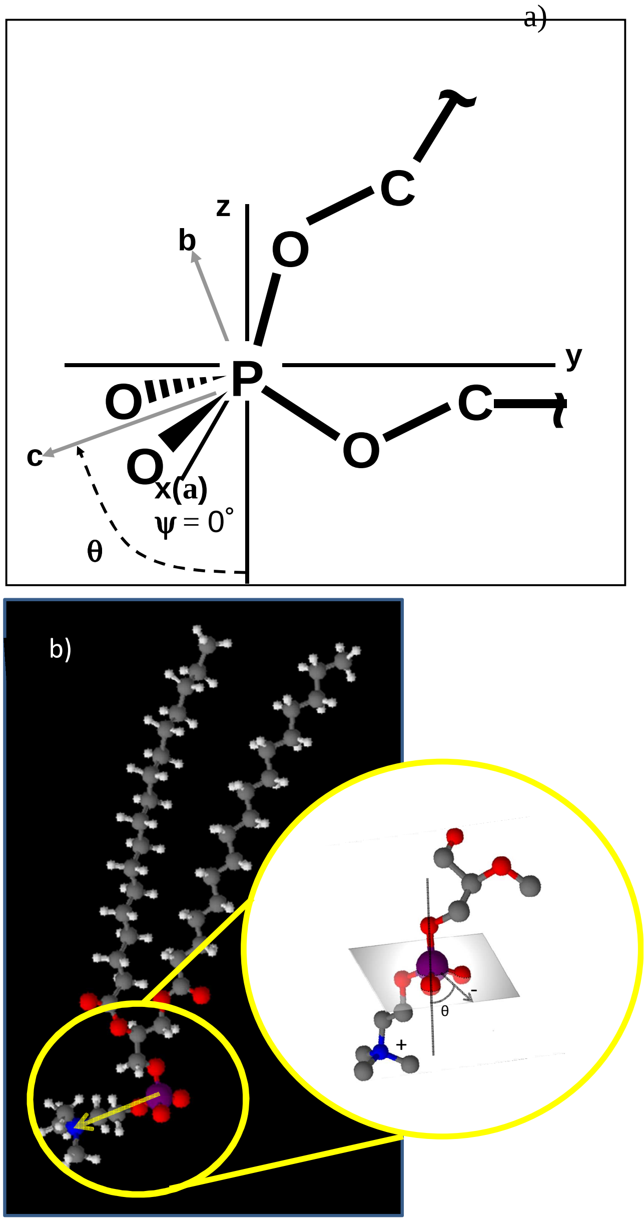

Figure 7.5. Graphical representation of a) the molecular and laboratory axes, *a,b,c* and *X*, *Y*, *Z*, respectively of the phosphate group where the *a* and *X* axes are chosen to be overlapped. The tilt angle, θ which is considered to be between *Z* and *c*, and the twist angle,Ψ which is considered to be zero, are also shown. In b) the DPPC molecule showing the phosphate-nitrogen vector with a yellow arrow and the tilt angle, θ of the phosphate group in the inset is shown with a smaller grey arrow. The carbon, oxygen, phosphorous, nitrogen, and hydrogen atoms are represented by gray, red, purple, blue, and white spheres, respectively.

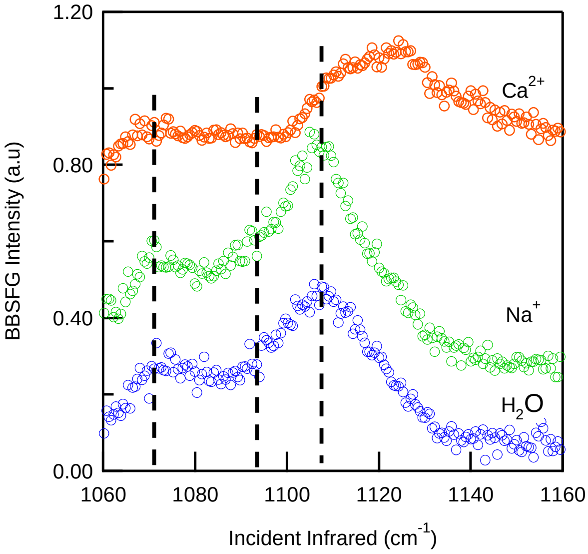

Figure 7.6. SFG spectra of DPPC monolayers on silica at 40mN/m transfer pressure from water, NaCl, and $CaCl_2$ subphases.

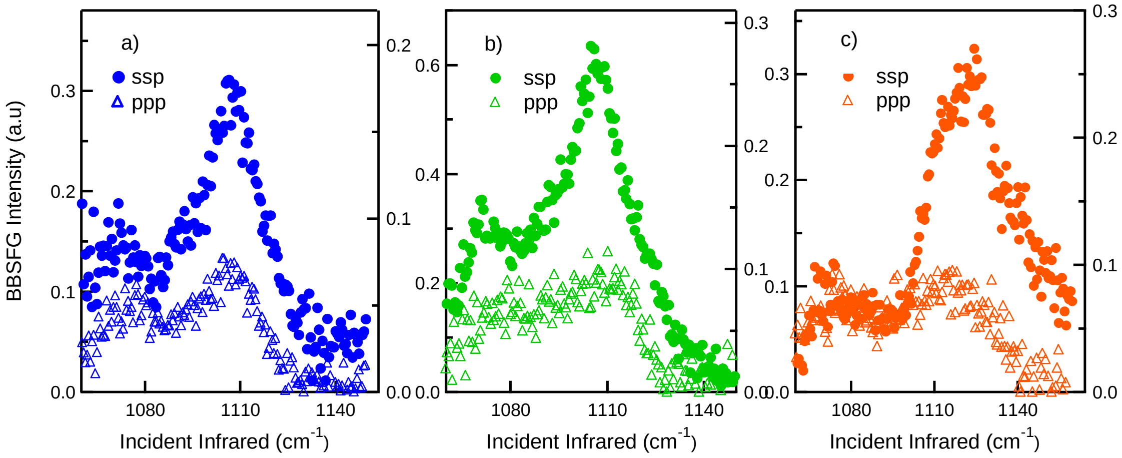

Figure 7.7. SFG spectra under ssp and ppp polarization combinations of DPPC monolayers on silica transferred from a) water, b) 0.5 M NaCl, and c) 0.4 M $CaCl_2$ at 40 mN/m transfer pressure.

		Aqueous		Silica	
Subphase	Surface Pressure mN/m	PO_2^- Peak Position cm^{-1}	PO_2^- FWHM	PO_2^- Peak Position cm^{-1}	PO_2^- FWHM
Water	4	1098	40	-	-
0.5 M NaCl	4	1100	44	-	-
0.4 M $CaCl_2$	4	1100	53	-	-
Water	12	1103	36	-	-
0.5 M NaCl	12	1103	44	-	-
0.4 M $CaCl_2$	12	1109	61	-	-
Water	40	1104	34	1106	24
0.5 M NaCl	40	1104	44	1104	17
0.4 M $CaCl_2$	40	1111	61	1120	36

Table. 7.1. Peak positions and full width half maximum of the PO_2^- peak of DPPC in the aqueous and silica supported monolayers.

Chapter 8

Surface Uptake of Alkyl Halides and Alcohols at the Air-Water Interface

The study of halogenated species is of atmospheric relevance due to the implication of these species in the destruction of ozone in the atmosphere. [2] One of the major contributors of organic chloride to the atmosphere is methyl chloride (MeCl). [239] Several sources of MeCl have been reported including, tropical plants[240], coastal marshes[241], biomass burning[242], and the ocean [243] which has also been recognized as a net sink of MeCl at high latitudes.

The main components of atmospheric secondary aerosols are water, inorganic salts and organic compounds. The uptake of oxidized organics species has been related to aerosol growth [244] and may affect the properties of atmospheric aerosols. In this chapter the organization of gas-phase alkyl halides and alcohol molecules adsorbed to the air-water interface is examined. Additionally, the bulk aqueous phase was analyzed for the uptake of gas-phase species.

This study was conducted with the collaboration of Kandice Harper and Roxana Sierra-Hernández. Some of the data presented in this chapter have been previously published in Harper's M.Sc. thesis and paper. [245, 246]In this chapter complementary SFG data under ppp and sps polarization combinations, Raman spectra of all the aqueous solutions after the flow of gas species, and IR energy test are presented. Additional studies of the IR absorption of the gas phase species were conducted and are presented in Sierra-Hernández's Ph.D dissertation. [247]

Chemical abbreviations used in this Chapter are:

MeOH (methanol); MeCl (methyl chloride); BuOH (butanol); BuCl (butyl chloride); BuBr (butyl bromide).

8.1 Materials

Methyl alcohol (CH_3OH; HPLC grade), *n*-butyl chloride (C_4H_9Cl; ACS certified), and *n*-butyl alcohol (C_4H_9OH; ACS certified) were obtained from Fisher Scientific. *n*-Butyl bromide (C_4H_9Br; 99+% purity) was obtained from Acros Organics. Methyl chloride (CH_3Cl; 99.5% purity, instrument grade) was obtained from Scott Specialty Gases, Inc. (Plumsteadville, PA). Nitrogen was obtained from Praxair, Inc. (Danbury, CT).

8.2 Experimental details

Air-water interfaces were analyzed with a broad bandwidth SFG spectrometer during the flow of gas-phase compounds into a closed chamber containing 24 mL of water in a Petri dish as shown in Figure 8.1. The SFG spectra were acquired for 1 min and continuously obtained for up to two hours. SFG spectra were background-subtracted and normalized to the nonresonant SFG signal from a GaAs crystal. The effect of evaporation was tested during these experiments to ensure proper overlap of the incident pulses. Detailed description of the chamber and flow conditions can be found elsewhere. [245] The SFG spectra were acquired under the ssp, ppp, and sps polarization combinations. Infrared energy tests to verify that there were sufficient infrared photons after flowing all the gas-phase species was performed in the scanning SFG system. Details of this spectrometer can be found in Chapter 2.

Bulk aqueous solutions were analyzed with a Raman spectrometer that uses 150 mW from 532 nm continuous wave laser. An acquisition time of 3 minutes was used for all the spectra.

8.3 Results and Discussion

The air-aqueous interfaces after 2 h of flow of alkyl halides and alcohols were analyzed by SFG spectroscopy and their spectra are shown in Figure 8.2. The polarization combinations used were ssp, ppp, and sps are shown in Figure 8.2a, 8.2b, and 8.2c, respectively. The left panels show the methyl species, while the right panels show the butyl species. The presence of CH stretching peaks at the surface of water clearly indicates the adsorption of MeOH and BuOH. In addition, this indicates that these alcohol molecules are not completely disordered but rather have a preferential orientation at the interface. Previous molecular dynamics studies of short chain alcohols at the air-aqueous interface indicate that the hydroxyl group of the alcohol hydrogen bonds to the surface water molecules. [248-250] The peak positions of MeOH and BuOH spectra are in agreement with previously reported studies of pure compounds at the interface. [251, 252]

In contrast, no CH stretching peaks were detected at the air-aqueous interface after the flow of the alkyl halide species under any polarization combinations (Figure 8.2a-c). This suggests that alkyl halide species either do not adsorb to the aqueous surface upon collision or do adsorb to the aqueous surface, but have a low number density, disordered interfacial arrangement, very short surface residence time, or some combination of these phenomena.

Raman spectra were acquired immediately after the flow of the gas-phase species of each compound and are shown in Figure 8.3 in the low frequency region (Figure 8.3a) and in the CH stretching region (Figure 8.3b). In Figure 8.3a, a broad peak is observed in all the spectra at ~800 cm^{-1} and is assigned to vibrational modes from water molecules. Additionally in this region, a peak at 710 cm^{-1} is observed and assigned to the C-Cl stretch[253] in the spectrum of MeCl. The presence of a peak attributed to MeCl in the spectrum of the bulk aqueous phase is direct evidence that MeCl is taken up into the aqueous phase from the gas-phase during the flow experiments. No peaks from the C-Cl and C-Br stretches of the butyl species are observed. This indicates that unlike MeCl, these species are not taken up into the aqueous bulk phase. This could be attributed to the low water solubility of these species. [254] A peak at ~1026 cm^{-1} is observed and assigned to the C-O symmetric stretching of MeOH. Uptake of gas-phase MeOH into the bulk aqueous phase has been reported previously.[255] In Figure 8.3b, CH stretching peaks are observed only in the Raman spectra after the flow of alcohols.

Although MeCl is not detected at the interface during the SFG experiments, the Raman bulk-phase studies indicate that some interaction of the gas-phase molecules with the aqueous interface must occur because uptake of MeCl from the gas-phase into the aqueous phase is observed (Figure 8.2). To explain these results, several reasons must be considered including orientation and number density of the molecules at the surface. In addition, absorption of the incident infrared laser beam by the gas-phase molecules before reaching the surface could lead to a lack of SFG response. To verify that there were sufficient infrared photons after flowing alkyl halides, the infrared energy coming out of the chamber was measured. This set of experiments was performed on the scanning SFG system. The infrared beam reflected from a gold mirror was monitored as the infrared beam was scanned from 2800 to 3100 cm^{-1}. A scan of the empty chamber was acquired and is shown in Figure 8.4 (initial). There is a relative constant infrared energy of ~ 180 μJ in this wavenumber range. Then the gas-phase of a compound was flowed for approximately an hour and the infrared energy was measured from 2800 to 3100 cm^{-1}. The chamber was then evacuated with pure N_2 until the initial infrared energy (~ 180 μJ) was recovered. Then the same procedure was followed for all the compounds and the results are shown in Figure 8.4.

Several dips are observed in the spectra of all compounds. These dips correspond to the absorbances (assigned to CH_3 and CH_2 symmetric stretches, CH_3 and CH_2 asymmetric stretches, and CH_3 and CH_2 Fermi resonances) of the gas-phase molecules of the alkyl halides and the alcohols. Also, it was observed that the infrared energy after MeOH flow was the lowest. From these results, it can be suggested that the infrared energy after the alkyl halide flow is sufficient to generate sum frequency signal.

Regarding the orientation of the MeCl molecules at the water surface, by comparing electronegativities the C-Cl bond in MeCl, it is expected to be slightly more polar than the C-H bonds. Therefore it is plausible that the C-Cl bond might preferentially associate with the aqueous phase compared to the more hydrophobic C-H bonds, which would then be expected to be oriented more toward the vapor phase. A low number density of interfacial MeCl could be the result of a low probability of adsorption upon collision, fast desorption from the surface for those molecules that do adsorb upon collision, or fast solvation of adsorbed molecules.

Molecular dynamic simulations of a water slab with MeCl molecules show that MeCl is present at the air-water interface and that its concentration is significantly enhanced in the interfacial region.[245] Also shown is that unlike MeOH, MeCl molecules form a rather dynamic and highly disordered surface layer on water. The most surprising finding from these simulations was that on average the MeCl molecules are oriented with the CH_3 group, rather than the halogen atom towards the water.[245] In brief, despite analogies in physical and chemical properties between alkyl halides and alcohols, MeCl interacts with the aqueous surface in a different way and adopt a different geometry at the air-water interface than MeOH. In the case of the BuCl and BuCl, these molecular dynamic studies [245] showed that similarly to the MeCl, these species are adsorbed at the surface, although no butyl halide molecule was observed to enter the bulk liquid region of the water slab. A low number density due to short residence times of butyl halides on the surface as well as the large degree of orientation disorder are likely to be the cause for the absence of the SFG signal corresponding to BuCl and BuBr.

8.4 Conclusions

Adsorption of gas-phase alkyl halides and alcohols to the air-water interface was studied using surface sensitive vibrational sum frequency spectroscopy. MeOH and BuOH are adsorbed into the aqueous solution as revealed by surface (SFG) and bulk (Raman) spectroscopies. MeCl, BuCl and BuBr were not detected at the air-water interface, although MeCl was readily observed in the bulk. Orientation (disordered molecules) and low number density have been invoked to explain the absence of the MeCl signal in the SFG spectrum. These findings are likely to have consequences for atmospheric chemistry, in particular for photodissociation of MeCl when adsorbed on an aerosol surface.

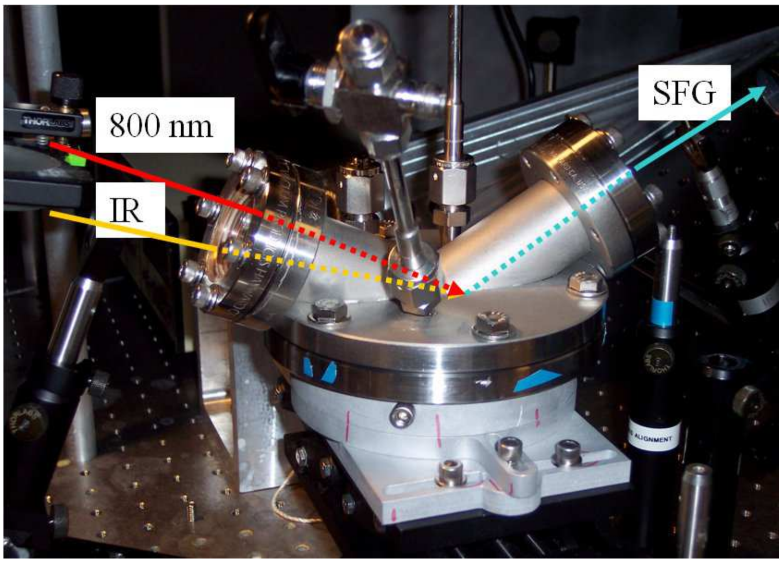

Figure 8.1. Chamber containing water in a Petri dish used during the flow of gas-phase compounds.

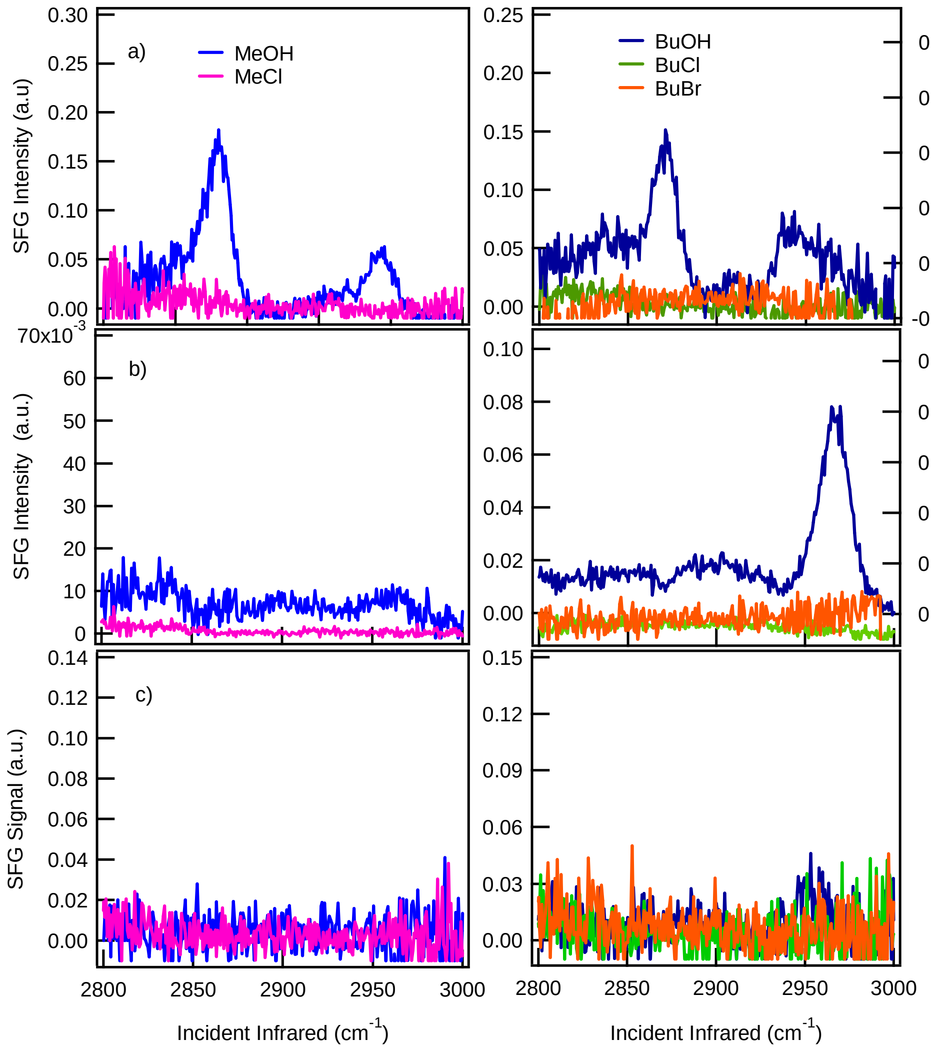

Figure 8.2. SFG spectra from flow experiments over water: methyl species (left panel) and butyl species (right panel) under a) ssp, b) ppp, and c) sps polarization combinations.

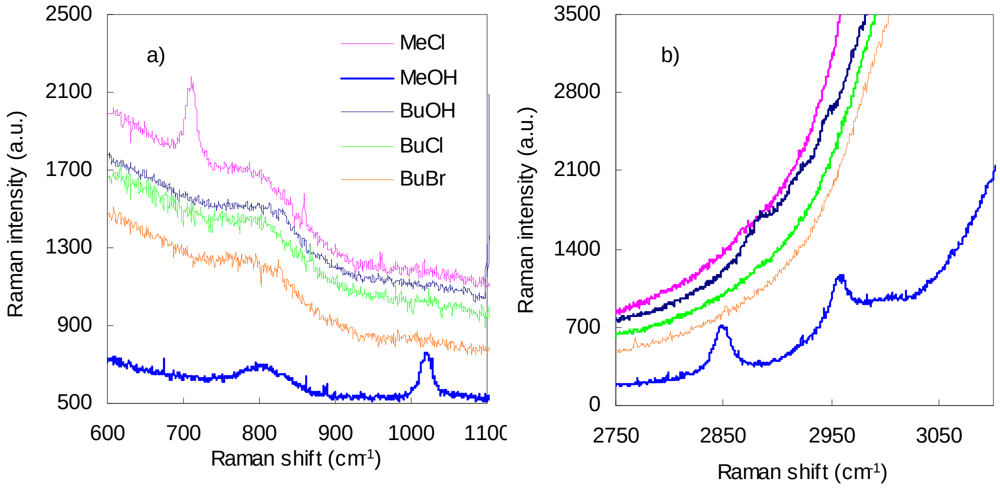

Figure 8.3. Raman spectra of bulk aqueous-phase after flow experiments in a) the low spectral region and in b) the C-H stretching region.

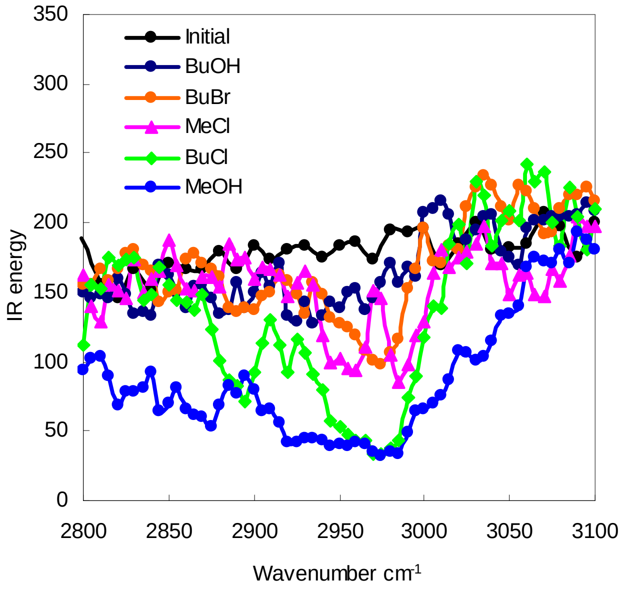

Figure 8.4. Infrared energy versus wavenumber at initial conditions (empty chamber) and during the flow of MeOH, MeCl, BuOH, BuCl, and BuBr.

Chapter 9

Environmental Implications

The research presented in this dissertation was motivated by a desire to contribute to the knowledge on interfacial water organization in atmospheric marine aerosols, and the interfacial cell membrane interactions with inhaled silica particles in the lungs. Structure and chemistry at aqueous interfaces are topics of fundamental interest, with applications ranging from heterogeneous reactions in the atmosphere to ionic transport across membranes. Given the complexity of atmospheric and biological relevant interfaces in nature, it is important to design model systems for detailed experimental investigations of fundamental interactions. With this in consideration, the work presented here seeks to advance fundamental understanding of interfacial water organization in the presence of magnesium and cation-lipid interaction at the air-water and air-silica interfaces.

The air-aqueous interface of a marine aerosol, based on the work presented here, is Cl^- and Mg^{2+} rich. Both ions will be further attracted toward the surface as the aerosol loses water during continental transit. Additionally, the water surface structure is highly influenced by the presence of the divalent magnesium cation, which does not form contact ion pairs with Cl^- even at high salt concentration. Because Cl^- is closer to the interface in the presence of Mg^{2+}, the surface reactivity of the marine boundary layer is likely enhanced when the aerosol passes over dryer continental regions as it is transported inland. Also shown is a reduced number of interfacial water molecules as the concentration of the salt increases, limiting the surface area of water for the adsorption of gas-phase species.

Water uptake by amorphous silica after the exposure to mid RH values is shown. Water adsorption modifies the optical properties of mineral aerosol particles by changing their size and index of refraction. Also the hydrated surface could act as a sink for gas-phase species (e.g. NO_2). The removal of these active gas-phase species may have an impact on the chemistry of the atmosphere.

DPPC headgroups are affected considerably at the silica surface compared to the aqueous subphase. This finding may be important with respect to the pathogenicity of silica in pulmonary diseases.

Adsorption and uptake of methanol, butanol and methyl chloride at the water surface is revealed. Once adsorbed, these compounds have the potential to participate in interfacial processes in the atmosphere. The presence of these compounds at the surface makes them susceptible to photodissociation and, as described above, will modify the physical and chemical properties of aerosols.

Appendix A: IR transmission spectra of liquid samples

In the past, [17, 125, 127, 150]the ATR-IR spectra were used in place of transmission IR because of difficulties with keeping the required short path length of the cell constant. However, a new method to circumvent this issue is by acquiring the data in transmission mode (where small path length variations are unavoidable) and then normalizing the spectra to the combination band at ~2200 cm^{-1} since this band is insensitive to addition of ions. [256-258]

The transmission spectra were obtained by using a Spectrum Spotlight 300 FT-IR Microscope (Perkin Elmer). The sample solutions were placed in-between two CaF_2 windows. A total of 124 scans were acquired for each sample. ATR-FTIR spectra were acquired in a Thermo Nicolet spectrometer (Thermo Electron Corporation, Avantar 370). 128 scans were obtained for each sample. In both type of spectra the resolution was set to be 4 cm^{-1}.

The ATR-IR spectra and IR transmission spectra of aqueous $MgCl_2$ solutions of 0.1 M, 0.3 M, 1.1 M, 2.1 M, 3.1 M and 4.7 M in the OH stretching region are shown in Figure A.1 and A.2, respectively. The ATR-IR spectra in the OH stretching region present a different shape compared to the transmission mode spectra. This is due to a change in refractive index and the inclusion of the real part of the index.

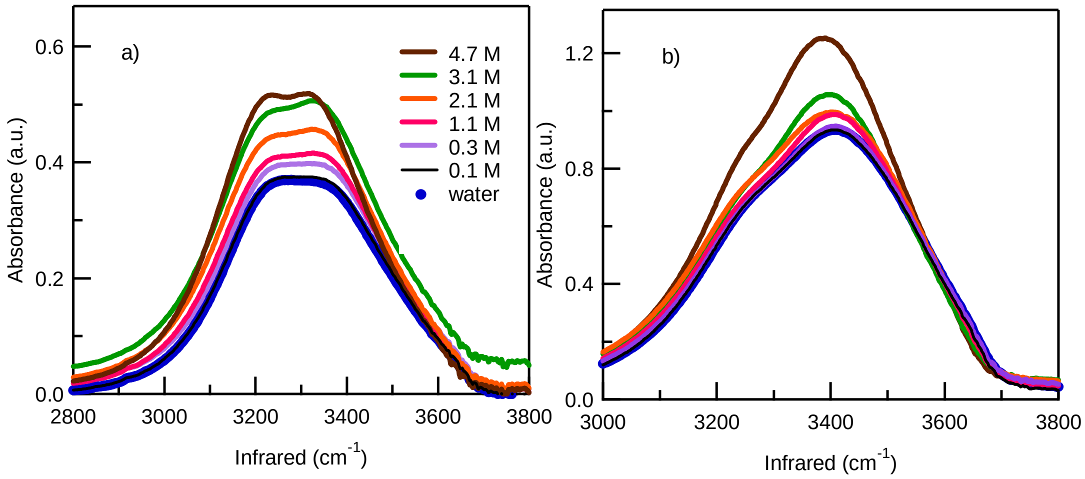

Figure A.1. a) ATR-IR and b) transmission spectra of aqueous $MgCl_2$ solutions of 0.1 M, 0.3 M, 1.1 M, 2.1 M, 3.1 M and 4.7 M in the OH stretching region. Neat water spectra are included for reference.

Appendix B: Determination of the average angle orientation of the phosphate group of DPPC

An SFG polarization study provides the average orientation of a specific moiety given certain theoretical treatments. Different components of $\chi^{(2)}$ are related to the spectroscopically active components of molecular hyperpolarizability tensor $\beta^{(2)}$ by the average orientation angle of the functional group. [117, 118, 130, 155, 259] The molecular symmetry determines the nonzero elements of $\beta^{(2}$. [259] The PO_2^- moiety on the DPPC headgroup can be treated as having C_{2v} symmetry. Mathcad software was used to determine the orientation angle of the symmetric stretch of the PO_2^- of the phosphate group of DPPC. For different chemical system the values of n1, n2, n3 and r should be modified.

Here are some definitions for some parameters used in this program:

ω=SFG; ω1=vis; ω2=IR

n1 is the refractive index of air.
n2 is the refractive index of water.
n3 is the refractive index of interfacial region

n1ω is the refractive index of air at the wavelength of SFG
n2ω is the refractive index of water at the wavelength of SFG
n3ω is the refractive index of interfacial region at the wavelength of SFG
n1ω1 is the refractive index of air at the wavelength of visible
n2ω1 is the refractive index of water at the wavelength of visible
n3ω1 is the refractive index of interfacial region at the wavelength of visible
n1ω2 is the refractive index of air at the wavelength of IR
n2ω2 is the refractive index of water at the wavelength of IR
n3ω2 is the refractive index of interfacial region at the wavelength of IR

β is the incident angle; **γ** is the refraction angle

$\beta\omega$ is the incident angle for SFG; **$\beta\omega 1$** is the Vis incident angle; **$\beta\omega 2$** is the IR incident angle

$\gamma\omega$ is the incident angle for SFG; **$\gamma\omega 1$** is the Vis incident angle; **$\gamma\omega 2$** is the IR incident angle

L is the fresnel factor

χ is the 2nd order susceptibility

βaac and **β**ccc are the molecular hyperpolarizability

$n1\omega 1 := 1$ $\quad n1\omega 2 := 1$ $\quad n1\omega := 1$

actual peak position of the 800 nm

$\omega 1 := 79$

$n2\omega 1 := 1.332$

actual peak position of the IR cm^{-1}

$\omega 2 := 110$

$n2\omega 2 := 1.2$

calculated peak position of SFG (nm)

$\omega = 731.068$

$n2\omega := 1.33$

incident angles of 800 nm and IR (degree)

$\beta\omega 1 := 53.$ $\quad \beta\omega 2 := 7$

$$\beta\omega := \frac{180 \cdot \operatorname{asin}\left(\frac{\omega}{\omega 1} \cdot \sin\left(\beta\omega 1 \cdot \frac{\pi}{180}\right) + \frac{\omega 2 \cdot \omega}{10^7} \cdot \sin\left(\beta\omega 2 \cdot \frac{\pi}{180}\right)\right)}{\pi}$$

calculated incident angle of SFG (degree)

$\beta\omega = 54.188$

calculated refractive angle of 800 nm (degree)

$$\gamma\omega 1 := 180 \cdot \frac{\operatorname{asin}\left(\frac{n1\omega 1}{n2\omega 1} \cdot \sin\left(\beta\omega 1 \cdot \frac{\pi}{180}\right)\right)}{\pi}$$

$\gamma\omega 1 = 36.961$

calculated refractive angle of IR (degree)

$$\gamma\omega2 := 180 \cdot \frac{\operatorname{asin}\left(\frac{n1\omega2}{n2\omega2} \cdot \sin\left(\beta\omega2 \cdot \frac{\pi}{180}\right)\right)}{\pi}$$

$\gamma\omega2 = 48.743$

calculated refractive angle of SFG (degree)

$$\gamma\omega := 180 \cdot \frac{\operatorname{asin}\left(\frac{n1\omega}{n2\omega} \cdot \sin\left(\beta\omega \cdot \frac{\pi}{180}\right)\right)}{\pi}$$

$\gamma\omega = 37.537$

calculated interfacial refractive index n3 of 800 nm

$$n3\omega1 := \sqrt{\frac{n2\omega1^4 + 5 \cdot n2\omega1^2}{4 \cdot n2\omega1^2 + 2}}$$

$n3\omega1 = 1.149$

calculated interfacial refractive index n3 of IR

$$n3\omega2 := \sqrt{\frac{n2\omega2^4 + 5 \cdot n2\omega2^2}{4 \cdot n2\omega2^2 + 2}}$$

$n3\omega2 = 1.115$

calculated interfacial refractive index n3 of SFG

$$n3\omega := \sqrt{\frac{n2\omega^4 + 5 \cdot n2\omega^2}{4 \cdot n2\omega^2 + 2}}$$

$n3\omega = 1.149$

Fresnel factors for SFG beam

$$Lxx\omega := \frac{2 \cdot n1\omega \cdot \cos\left(\gamma\omega \cdot \frac{\pi}{180}\right)}{n1\omega \cdot \cos\left(\gamma\omega \cdot \frac{\pi}{180}\right) + n2\omega \cdot \cos\left(\beta\omega \cdot \frac{\pi}{180}\right)} \qquad Lxx\omega = 1.009$$

$$Lyy\omega := \frac{2 \cdot n1\omega \cdot \cos\left(\beta\omega \cdot \frac{\pi}{180}\right)}{n1\omega \cdot \cos\left(\beta\omega \cdot \frac{\pi}{180}\right) + n2\omega \cdot \cos\left(\gamma\omega \cdot \frac{\pi}{180}\right)} \qquad Lyy\omega = 0.713$$

$$Lzz\omega := \frac{\left(2 \cdot n2\omega \cdot \cos\left(\beta\omega \cdot \frac{\pi}{180}\right)\right) \cdot \left(\frac{n1\omega}{n3\omega}\right)^2}{n1\omega \cdot \cos\left(\gamma\omega \cdot \frac{\pi}{180}\right) + n2\omega \cdot \cos\left(\beta\omega \cdot \frac{\pi}{180}\right)} \qquad Lzz\omega = 0.751$$

Fresnel factors for 800 nm beam

$$Lxx\omega1 := \frac{2 \cdot n1\omega1 \cdot \cos\left(\gamma\omega1 \cdot \frac{\pi}{180}\right)}{n1\omega1 \cdot \cos\left(\gamma\omega1 \cdot \frac{\pi}{180}\right) + n2\omega1 \cdot \cos\left(\beta\omega1 \cdot \frac{\pi}{180}\right)} \qquad Lxx\omega1 = 1$$

$$Lyy\omega1 := \frac{2 \cdot n1\omega1 \cdot \cos\left(\beta\omega1 \cdot \frac{\pi}{180}\right)}{n1\omega1 \cdot \cos\left(\beta\omega1 \cdot \frac{\pi}{180}\right) + n2\omega1 \cdot \cos\left(\gamma\omega1 \cdot \frac{\pi}{180}\right)} \qquad Lyy\omega1 = 0.722$$

$$Lzz\omega1 := \frac{\left(2 \cdot n2\omega1 \cdot \cos\left(\beta\omega1 \cdot \frac{\pi}{180}\right)\right) \cdot \left(\frac{n1\omega1}{n3\omega1}\right)^2}{n1\omega1 \cdot \cos\left(\gamma\omega1 \cdot \frac{\pi}{180}\right) + n2\omega1 \cdot \cos\left(\beta\omega1 \cdot \frac{\pi}{180}\right)} \qquad Lzz\omega1 = 0.758$$

Fresnel factors for IR beam

$$Lxx\omega2 := \frac{2\cdot n1\omega2\cdot \cos\left(\gamma\omega2\cdot\frac{\pi}{180}\right)}{n1\omega2\cdot\cos\left(\gamma\omega2\cdot\frac{\pi}{180}\right)+n2\omega2\cdot\cos\left(\beta\omega2\cdot\frac{\pi}{180}\right)} \qquad Lxx\omega2 = 1.213$$

$$Lyy\omega2 := \frac{2\cdot n1\omega2\cdot \cos\left(\beta\omega2\cdot\frac{\pi}{180}\right)}{n1\omega2\cdot\cos\left(\beta\omega2\cdot\frac{\pi}{180}\right)+n2\omega2\cdot\cos\left(\gamma\omega2\cdot\frac{\pi}{180}\right)} \qquad Lyy\omega2 = 0.586$$

$$Lzz\omega2 := \frac{\left(2\cdot n2\omega2\cdot \cos\left(\beta\omega2\cdot\frac{\pi}{180}\right)\right)\cdot\left(\frac{n1\omega2}{n3\omega2}\right)^2}{n1\omega2\cdot\cos\left(\gamma\omega2\cdot\frac{\pi}{180}\right)+n2\omega2\cdot\cos\left(\beta\omega2\cdot\frac{\pi}{180}\right)} \qquad Lzz\omega2 = 0.633$$

The single bond polarizability derivative ratio *r* is obtained by the Raman depolarization ratio as follows:

$$\tau := \frac{120\pi}{180} \qquad \cos(\tau) = -0.5$$

$$f(r) := \frac{3}{4+20\cdot\frac{(1+2\cdot r)^2}{\left[(1-r)^2\cdot\left(1+3\cos(\tau)^2\right)\right]}}$$

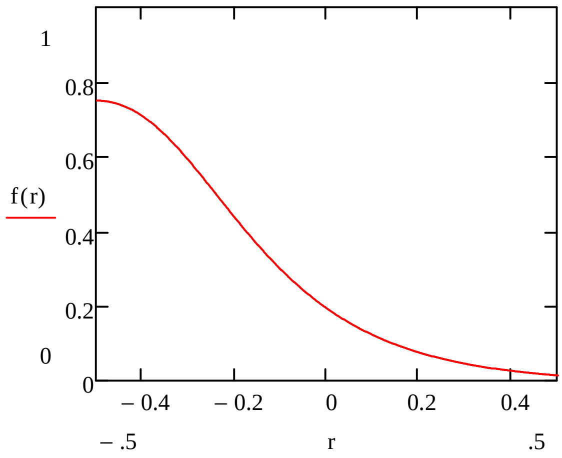

for a *f(r)* = 0.05 [217] then *r* = 0.24. If *a* = *r* then

$$Ra := \frac{(1+a)-(1-a)\cos(\tau)}{(1+a)+(1-a)\cos(\tau)} \qquad Ra = 1.884$$

$$Rb := 2\frac{a}{[(1+a)+(1-a)\cos(\tau)]} \qquad Rb = 0.558$$

$$R := \frac{[(1+3\cdot a)-(1-a)\cdot\cos(\tau)]}{2[(1+a)+(1-a)\cdot\cos(\tau)]} \qquad R = 1.221$$

orientation angle of θ of phosphate (PO_2^-) group

$\theta := 0, 1 .. 90$

$\beta ccc := 1 \qquad Ns := 1$

For PO_2^--SS, where ψ = 0, the components of χ are given by

$$\chi yyz\_SS(\theta) := \frac{1}{2}\cdot Ns\cdot\beta ccc\cdot\left[(1+Ra)\cdot\cos\left(\theta\cdot\frac{\pi}{180}\right)-(1-Rb)\cdot\cos\left(\theta\cdot\frac{\pi}{180}\right)^{3}\right]$$

$$\chi yzy\_SS(\theta) := \frac{1}{2}\cdot Ns\cdot\beta ccc\cdot(1-Rb)\cdot\left(\cos\left(\theta\cdot\frac{\pi}{180}\right)-\cos\left(\theta\cdot\frac{\pi}{180}\right)^{3}\right)$$

χxxz is equal to χyyz and χxzx is equal to χyzy and χzxx is equal to χzyy

$$\chi\text{zzz\_SS}(\theta) := \text{Ns}\cdot\beta\text{ccc}\cdot\left[\text{Rb}\cdot\cos\left(\theta\cdot\frac{\pi}{180}\right) + (1-\text{Rb})\cdot\cos\left(\theta\cdot\frac{\pi}{180}\right)^{3}\right]$$

Normalization to the Fresnel factors to estimate χeffective

$$\chi\text{effective\_ssp\_SS}(\theta) := \text{Lyy}\omega\cdot\text{Lyy}\omega1\cdot\text{Lzz}\omega2\cdot\sin\left(\beta\omega2\cdot\frac{\pi}{180}\right)\cdot\chi\text{yyz\_SS}(\theta)$$

$$\chi\text{effective\_ppp\_SS}(\theta) := -\text{Lxx}\omega\cdot\text{Lxx}\omega1\cdot\text{Lzz}\omega2\cdot\cos\left(\beta\omega\cdot\frac{\pi}{180}\right)\cdot\cos\left(\beta\omega1\cdot\frac{\pi}{180}\right)\cdot\sin\left(\beta\omega2\cdot\frac{\pi}{180}\right)\cdot\chi\text{yyz\_SS}(\theta)$$

$$-\left(\text{Lxx}\omega\cdot\text{Lzz}\omega1\cdot\text{Lxx}\omega2\cdot\cos\left(\beta\omega\cdot\frac{\pi}{180}\right)\cdot\sin\left(\beta\omega1\cdot\frac{\pi}{180}\right)\cdot\cos\left(\beta\omega2\cdot\frac{\pi}{180}\right)\cdot\chi\text{yzy\_SS}(\theta)\right)$$

$$+\text{Lzz}\omega\cdot\text{Lxx}\omega1\cdot\text{Lxx}\omega2\cdot\sin\left(\beta\omega\cdot\frac{\pi}{180}\right)\cdot\cos\left(\beta\omega1\cdot\frac{\pi}{180}\right)\cdot\cos\left(\beta\omega2\cdot\frac{\pi}{180}\right)\cdot\chi\text{yzy\_SS}(\theta)$$

$$+\text{Lzz}\omega\cdot\text{Lzz}\omega1\cdot\text{Lzz}\omega2\cdot\sin\left(\beta\omega\cdot\frac{\pi}{180}\right)\cdot\sin\left(\beta\omega1\cdot\frac{\pi}{180}\right)\cdot\sin\left(\beta\omega2\cdot\frac{\pi}{180}\right)\cdot\chi\text{zzz\_SS}(\theta)$$

$$\chi\text{effective\_sps\_SS}(\theta) := \text{Lyy}\omega\cdot\text{Lzz}\omega1\cdot\text{Lyy}\omega2\cdot\sin\left(\beta\omega1\cdot\frac{\pi}{180}\right)\cdot\chi\text{yzy\_SS}(\theta)$$

$$\chi\text{2ssp\_SS}(\theta) := \left(\left|\chi\text{effective\_ssp\_SS}(\theta)\right|\right)^{2}$$

$$\chi\text{2ppp\_SS}(\theta) := \left(\left|\chi\text{effective\_ppp\_SS}(\theta)\right|\right)^{2}$$

$$\chi\text{2sps\_SS}(\theta) := \left(\left|\chi\text{effective\_sps\_SS}(\theta)\right|\right)^{2}$$

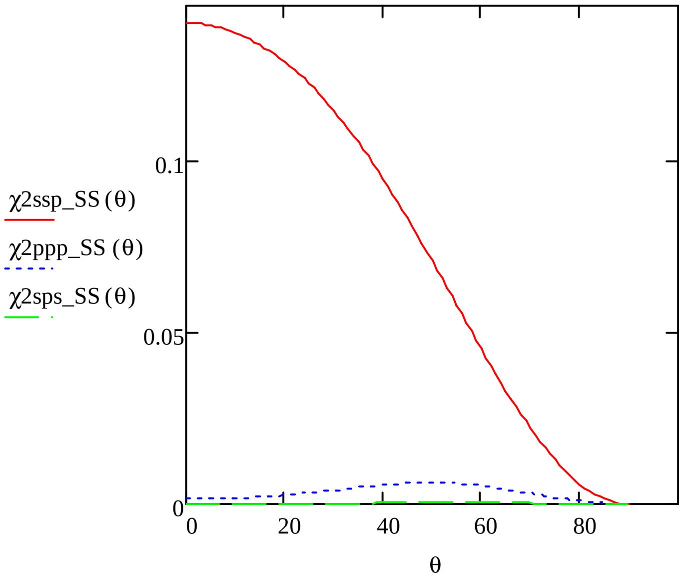
χ2ssp_SS (θ)
χ2ppp_SS (θ)
χ2sps_SS (θ)
0.1
0.05
0
0
20
40
60
80
θ

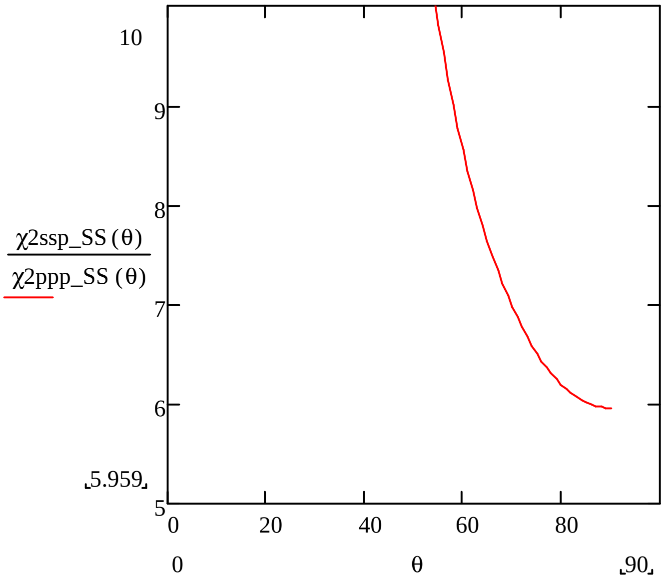
10
9
8
χ2ssp_SS (θ) / χ2ppp_SS (θ)
7
6
5.959
5
0
20
40
60
80
0
θ
90

References

1. Richens, D. T., *The chemistry of aqua ions: synthesis, structure, and reactivity: a tour through the periodic table of the elements*. Wiley: New York, 1997.

2. Finlayson-Pitts, B. J.; Pitts, J. N., *Chemistry of the upper and lower atmosphere*. Academic Press: New York, NY, 2000.

3. Foster, P.; Ramaswamy, V.; Artaxo, P.; Berntsen, T.; Betts, R.; Fahey, D. W.; Haywood, J.; Lean, J.; Lowe, D. C.; Myhre, G.; Nganga, J.; Prinn, R.; Raga, G.; Schulz, M.; Van Dorland, R., *Climate Change 2007: The physical science basis. Intergovernmental panel on climate change.* . Cambridge University Press: United Kindgdom, and New York, USA, 2007; p 129-234.

4. Prather, K. A.; Hatch, C. D.; Grassian, V. H., Analysis of atmospheric aerosols. *Ann. Rev. Anal. Chem.* 2008, 1, 485-514.

5. Textor, C.; Schulz, M.; Guibert, S.; Kinne, S.; Balkanski, Y.; Bauer, S.; Berntsen, T.; Berglen, T.; Boucher, O.; Chin, M.; Dentener, F.; Diehl, T.; Easter, R.; Feichter, H.; Fillmore, D.; Ghan, S.; Ginoux, P.; Gong, S.; Grini, A.; Hendricks, J.; Horowitz, L.; Huang, P.; Isaksen, I.; Iversen, T.; Kloster, S.; Koch, D.; Kirkevag, A.; Kristjansson, J. E.; Krol, M.; Lauer, A.; Lamarque, J. F.; Liu, X.; Montanaro, V.; Myhre, G.; Penner, J.; Pitari, G.; Reddy, S.; Seland, Ø.; Stier, P.; Takemura, T.; Tie, X., Analysis and quantification of the diversities of aerosol life cycles within AeroCom. *Atmos. Chem. Phys.* 2006, 6, 1777-1813.

6. Kester, D. R.; Duedall, I. W.; Connors, D. N.; Pytkowicz, R. M., Preparation of artificial seawater. *Limnol. Oceanogr.* 1967, 12, 176-179.

7. Allen, H. C.; Casillas-Ituarte, N. N.; Sierra-Hernández, M. R.; Chen, X.; Tang, C. Y., Shedding light on water structure at air-aqueous interfaces: ions, lipids, and hydration. *Phys. Chem. Chem. Phys.* 2009, 11, (27), 5538-5549.

8. Feng, R.-R.; Bian, H.-T.; Wang, H.-F., Spectroscopic evidence for the specific Na^+ and K^+ interactions with the hydrogen-bonded water molecules at the electrolyte aqueous solution surfaces. *J. Chem. Phys.* 2009, 130, 134710(1)-(6).

9. Ghosal, S.; Hemminger, J. C.; Bluhm, H.; Mun, B. S.; Hebenstreit, E. L. D.; Ketteler, G.; Ogletree, D. F.; Requejo, F. G.; Salmeron, M., Electron spectroscopy of aqueous solution interfaces reveals surface enhancement of halides. *Science* 2005, 307, (5709), 563-566.

10. Gopalakrishnan, S.; Liu, D.; Allen, H. C.; Kuo, M.; Shultz, M. J., Vibrational spectroscopic studies of aqueous interfaces: salts, acids, bases, and nanodrops. *Chem. Rev.* 2006, 106, (4), 1155-1175.

11. Jungwirth, P., How many waters are necessary to dissolve a rock salt molecule? . *J. Phys. Chem. A* 2000, 104, (1), 145-148.

12. Jungwirth, P.; Tobias, D. J., Surface effects on aqueous ionic solvation: a molecular dynamics simulation study of NaCl at the air/water interface from infinite dilution to saturation. *J. Phys. Chem. B* 2000, 104, (32), 7702-7706.

13. Jungwirth, P.; Tobias, D. J., Molecular structure of salt solutions: a new view of the interface with implications for heterogeneous atmospheric chemistry. *J. Phys. Chem. B* 2001, 105, (43), 10468-10472.

14. Jungwirth, P.; Tobias, D. J., Chloride anion on aqueous clusters, at the air-water interface, and in liquid water: solvent effects on Cl^- polarizability. *J. Phys. Chem. A* 2002, 106, (2), 379-383.

15. Jungwirth, P.; Tobias, D. J., Ions at the air/water interface. *J. Phys. Chem. B* 2002, 106, (25), 6361-6373.

16. Jungwirth, P.; Tobias, D. J., Specific ion effects at the air/water interface. *Chem. Rev.* 2006, 106, (4), 1259-1281.

17. Liu, D.; Ma, G.; Levering, L. M.; Allen, H. C., Vibrational spectroscopy of aqueous sodium halide solutions and air-liquid interfaces: observation of increased interfacial depth. *J. Phys. Chem. B* 2004, 108, (7), 2252-2260.

18. Mucha, M.; Frigato, T.; Levering, L. M.; Allen, H. C.; Tobias, D. J.; Dang, L. X.; Jungwirth, P., Unified molecular picture of the surfaces of aqueous acid, base, and salt solutions. *J. Phys. Chem. B* 2005, 109, (16), 7617-7623.

19. Petersen, P. B.; Johnson, J. C.; Knutsen, K. P.; Saykally, R. J., Direct experimental validation of the Jones-Ray effect. *Chem. Phys. Lett.* 2004, 397, (1-3), 46-50.

20. Petersen, P. B.; Saykally, R. J., Confirmation of enhanced anion concentration at the liquid water surface. *Chem. Phys. Lett.* 2004, 397, (1-3), 51-55.

21. Petersen, P. B.; Saykally, R. J., Adsorption of ions to the surface of dilute electrolyte solutions: the Jones-Ray effect revisited. *J. Am. Chem. Soc.* 2005, 127, (44), 15446-15452.

22. Petersen, P. B.; Saykally, R. J.; Mucha, M.; Jungwirth, P., Enhanced concentration of polarizable anions at the liquid water surface: SHG spectroscopy and MD simulations of sodium thiocyanide. *J. Phys. Chem. B* 2005, 109, (21), 10915-10921.

23. Schnitzer, C.; Baldelli, S.; Shultz, M. J., Sum frequency generation of water on NaCl, $NaNO_3$, $KHSO_4$, HCl, HNO_3, and H_2SO_4 Aqueous Solutions. *J. Phys. Chem. B* 2000, 104, (3), 585-590.

24. Tian, C.; Ji, N.; Waychunas, G. A.; Shen, Y. R., Interfacial structures of acidic and basic aqueous solutions. *J. Am. Chem. Soc.* 2008, 130, (39), 13033-13039.

25. Knipping, E. M.; Lakin, M. J.; Foster, K. L.; Jungwirth, P.; Tobias, D. J.; Gerber, R. B.; Dabdub, D.; Finlayson-Pitts, B. J., Experiments and simulations of ion-enhanced interfacial chemistry on aqueous NaCl aerosols. *Science* 2000, 288, (5464), 301-306.

26. Finlayson-Pitts, B. J.; Hemminger, J. C., Physical chemistry of airborne sea salt particles and their components. *J. Phys. Chem. A* 2000, 104, (49), 11463-11477.

27. Finlayson-Pitts, B. J., The tropospheric chemistry of sea salt: a molecular-level view of the chemistry of NaCl and NaBr. *Chem. Rev.* 2003, 103, (12), 4801-4822.

28. Hatch, C. D.; Grassian, V. H., 10th anniversary review: application of analytical techniques in laboratory studies of chemical and climatic impats of mineral dust aerosol in the Earth's atmosphere. *J. Environ. Monit.* 2008, 10, 919-934.
29. Sokolik, I. N.; Toon, O. B., Direct radiative forcing by anthropogenic airbone mineral aerosols. *Nature* 1996, 381, 681-683.
30. Lohmann, U.; Feichter, J., Global indirect aerosol effects: a review. *Atmos. Chem. Phys.* 2005, 5, 715-737.
31. Goodman, A. L.; Bernard, E. T.; Grassian, V. H., Spectroscopy study of nitric acid and water adsorption on oxide particles: Enhanced nitric acid uptake kinetics in the presence of adsorbed water. *J. Phys. Chem. A* 2001, 105, 6443-6457.
32. Claquin, T.; Schulz, M.; Balkanski, Y. J., Modeling the mineralogy of atmospheric dust sources. *J. Geophys. Res.* 1999, 104, 22243-22256.
33. Fubini, B.; Fenoglio, I., Toxic potential of mineral dust. *Elements* 2007, 3, 407-414.
34. NIOSH. Hazard Review: Health effects of occupational exposure to respirable crystalline silica. In (NIOSH), D., Ed. 2002; Vol. Publication No. 2002-129.
35. Roark, M.; Feller, S. E., Structure and dynamics of a fluid phase bilayer on a solid support as observed by a molecular dynamics computer simulation. *Langmuir* 2008, 24, 12469-12473.
36. Roke, S.; Schins, J.; Müller, M.; Bonn, M., Vibrational spectroscopic investigation of the phase diagram of a biomimetic lipid monolayer. *Phys. Rev. Lett.* 2003, 90, 128101(1)-(4).
37. Sackmann, E., Supported membranes: scientific and practical applications. *Science* 1996, 271, 43-48.
38. Watry, M. R.; Tarbuck, T. L.; Richmond, G. L., Vibrational sum-frequency studies of a series of phospholipid monolayers and the associated water structure at the vapor/water interface. *J. Phys. Chem. B* 2003, 107, 512-518.
39. Ma, G.; Allen, H. C., DPPC Langmuir monolayer at the air-water interface: probing tail and head groups by vibrational sum frequency generation spectroscopy. *Langmuir* 2006, 22, (2), 5341-5349.
40. Zhu, X. D.; Suhr, H.; Shen, Y. R., Surface vibrational spectroscopy by infrared-visible sum frequency generation. *Phys. Rev. B* 1987, 35, 3047-3050.
41. Du, Q.; Freysz, E.; Shen, Y. R., Vibrational spectra of water molecules at the quartz/water interfaces. *Physical Review Letters* 1994, 72, (2), 238-241.
42. Casillas-Ituarte, N. N.; Callahan, K. M.; Tang, C. Y.; Chen, X.; Roeselová, M.; Tobias, D. J.; Allen, H. C., Surface organization of aqueous $MgCl_2$ and application to atmospheric marine aerosol chemistry. *Proc. Natl. Acad. Sci.* 2010.
43. Li, I.; Bandara, J.; Shultz, M. J., Time evolution studies of the water/quartz interface using sum frequency generation, atomic force microscopy, and molecular dynamics. *Langmuir* 2004, 20, 10474-10480.
44. Ostroverkov, V.; Waychunas, G. A.; Shen, Y. R., Vibrational spectra of water at water/alpha-quartz (0001) interface. *Chem. Phys. Lett.* 2004, 386, 144-148.
45. Tao, W.; Shen, Y. R., Surface vibrational modes of alpha-quartz (0001) probed by sum frequency spectroscopy. *Phys. Rev. Lett.* 2008, 016101(1)-(4).

46. Shen, Y. R., *The principles of nonlinear optics*. John Wiley and Sons: New York, 1984.

47. Lambert, A. G.; Davies, P. B., Implementing the theory of sum frequency generation vibrational spectroscopy: a tutorial review. *Appl. Spectrosc. Rev.* 2005, 40, 103-145.

48. Tang, C. Y.; Allen, H. C., Ionic binding of K^+ and Na^+ to the carboxylic acid head group of palmitic acid in monolayers using vibrational sum frequency generation spectroscopy. *J. Phys. Chem. A* 2009, 113, (26), 7383-7393.

49. Langmuir, I., The mechanism of the surface phenomena of flotation. *Trans. Faraday Soc.* 1920, 15, 62-74.

50. Blodgett, K. B., Films built by deposition successive monomolecular layers on a solid surface. *J. Am. Chem. Soc.* 1935, 57, 1007-1022.

51. Collins, K. D., Charge density-dependent strength of hydration and biological structure. *Biophys. J.* 1997, 72, 65-76.

52. Lewis, E. R.; Schwartz, S. E., *Sea salt aerosol production: mechanisms, methods, measurements, and models*. American Geophysical Union: Washington, DC., 2005.

53. Marcus, Y., Effect of ions on the structure of water: structure making and breaking *Chem. Rev.* 2009, 109, 1346-1370.

54. Marcus, Y.; Hefter, G., Ion pairing. *Chem. Rev.* 2006, 106, 4585-4621.

55. Dixon, J. B.; Weed, S. B., *Minerals in soil environments*. 2nd ed.; Soil Science Society of America: Madison, WI, 1989.

56. Bernasconi, L.; Baerends, E. J.; Sprik, M., Long-range solvent effects on the orbital interaction mechanism of water acidity enhancement in metal ion solutions: a comparative study of the electronic structure of aqueous Mg and Zn dications. *J. Phys. Chem. B* 2006, 110, (23), 11444-11453.

57. Cowan, J. A., Structural and catalytic chemistry of magnesium-dependent enzymes. *Biometals* 2002, 15, 225-235.

58. Gong, B.; Chen, Y.; Christian, E. L.; Chen, J.-H.; Chase, E.; Chadalavada, D. M.; Yajima, R.; Golden, B. L.; Bevilacqua, P. C.; Carey, P. R., Detection of innersphere interactions between magnesium hydrate and the phosphate backbone of the HDV ribozyme using Raman crystallography. *J. Am. Chem. Soc.* 2008, 130, (30), 9670-9672.

59. Jiao, D.; King, C.; Grossfield, A.; Darden, T. A.; Ren, P., Simulation of Ca^{2+} and Mg^{2+} solvation using polarizable atomic multipole potential. *J. Phys. Chem. B* 2006, 110, (37), 18553-18559.

60. Caminiti, R.; Licheri, G.; Piccaluga, G.; Pinna, G., X-ray diffraction study of a "three-ion" aqueous solution. *Chem. Phys. Lett.* 1977, 47, (2), 275-278.

61. Caminiti, R.; Licheri, G.; Piccaluga, G.; Pinna, G., X-ray diffraction study of $MgCl_2$ aqueous solutions. *J. Appl. Cryst.* 1979, 12, 34.

62. Dorosh, A. K.; Skryshevskii, A. F., The structural characteristics of the immediate environment of cations in aqueous solutions. *Z. Strukturnoi Khimii* 1964, 5, 911.

63. Pálinkás, G.; Radnai, T.; Dietz, W.; Szász, G. I.; Heinzinger, K., Hydration shell structures in an $MgCl_2$ solution from X-ray and MD studies. *Z. Naturforsch.* 1982, 37a, 1049-1060.

64. Waizumi, K.; Masuda, I.; Fukushima, N., A molecular approach to the formation of KCl and $MgCl^+$ ion-pairs in Aqueous solution by density functional calculations. *Chem. Phys. Lett.* 1993, 205, (2,3), 317-323.

65. Zapalowski, M.; Bartczak, W. M., Concentrated aqueous $MgCl_2$ solutions. A computer simulation study of the solution structure and excess electron localisation. *Res. Chem. Intermed.* 2001, 27, 855-866.

66. Doughty, H. W., Mohr's method for determination of silver and halogens in other than neutral solutions. *J. Am. Chem. Soc.* 1924, 46, (12), 2707-2709.

67. Phang, S.; Stokes, R. H., Density, Viscosity, Conductance, and Transference Number of Concentrated Aqueous Magnesium Chloride at 25°C. *J. Solution Chem.* 1980, 9, (7), 497-505.

68. Adrian-Scotto, M.; Mallet, G.; Vasilescu, D., Hydration of Mg^{2+}: a quantum DFT and an initio HF study. *J. Mol. Struct.* 2005, 728, 231-242.

69. Bock, C.; Kaufman, A.; Glusker, J., Coordination of water to magnesium cations. *Inorg. Chem.* 1994, 33, 419-427.

70. Bock, C.; Markham, G.; Katz, A.; Glusker, J., The arrangement of first- and second-shell water molecules around metal ions: effects of charge and size. *Theor. Chem. Acc.* 2006, 115, (2), 100-112.

71. Jagoda-Cwiklik, B.; Jungwirth, P.; Rulísek, L.; Milko, P.; Roithová, J.; Lemaire, J.; Maitre, P.; Ortega, J. M.; Schröder, D., Micro-hydration of the $MgNO_3^+$ cation in the gas phase. *ChemPhysChem* 2007, 8, 1629-1639.

72. Markham, G.; Glusker, J.; Bock, C., The arrangement of first- and second-sphere water molecules in divalent magnesium complexes: results from molecular orbital and density functional theory and from structural crystallography. *J. of Phys. Chem. B* 2002, 106, 5118-5134.

73. Markham, G. D.; Glusker, J. P.; Bock, C. L.; Trachtman, M.; Bock, C. W., Hydration energies of divalent beryllium and magnesium ions: an ab initio molecular orbital study. *J. of Phys. Chem.* 1996, 100, 3488-3497.

74. Martínez, J. M.; Pappalardo, R. R.; Marcos, E. S., First-principles ion-water interaction potentials for highly charged monatomic cations. Computer simulations of Al^{3+}, Mg^{2+}, and Be^{2+} in water. *J. Am. Chem. Soc.* 1999, 121, 3175-3184.

75. Spångberg, D.; Hermansson, K., Effective three-body potential for Li^+*(aq)* and Mg^{2+}*(aq)*. *J. Chem. Phys.* 2003, 119, (14), 7263-7281.

76. Mink, J.; Németh, C.; Hajba, L.; Sandström, D. R.; Goggin, P. L., Infrared and Raman spectroscopic and theoretical studies of hexaaqua metal ions in aqueous solution. *J. Mol. Struct.* 2003, 661-662, 141-151.

77. Pye, C. C.; Rudolph, W. W., An ab initio and Raman investigation of magnesium (II) hydration. *J. Phys. Chem. A* 1998, 102, 9933-9943.

78. Rudolph, W. W.; Irmer, G.; Hefter, G. T., Raman spectroscopic investigation of speciation in $MgSO_4$(aq). *Phys. Chem. and Chem. Phys.* 2003, 5, 5253-5261.

79. Capwell, R. J., Raman spectra of crystalline and molten $MgCl_2$. *Chem. Phys. Lett.* 1972, 12, 443-446.

80. Huang, C.-H.; Brooker, M. H., Raman spectrum of molten $MgCl_2$. *Chem. Phys. Lett.* 1976, 43, 180-182.

81. Tepavitcharova, S.; Balarew, C.; Rull, F.; Rabadjieva, D.; Iliev, A., Raman spectroscopic studies of ion association in the Na+, Mg2+/Cl-, SO42-/H2O system. *J. Raman Spectrosc.* 2005, 36, (9), 891-897.

82. Sano, H.; Miyaoka, H.; Kuze, T.; Mori, H.; Mizutani, G.; Otsuka, N.; Terano, M., Raman spectra of magnesium chloride thin films *Surf. Sci.* 2002, 502-503, 70-74.

83. Sugimoto, K.; Dinnebier, R. E.; Hanson, J. C., Structures of three dehydration products of bischofite from *in situ* synchrotron powder diffraction data ($MgCl_2 \cdot n$H2O; n = 1, 2, 4). *Acta Cryst. B* 2007, 63, 235-242.

84. Bernal-Uruchurtu, M. I.; Ortega-Blake, I., A refined Monte Carlo study of Mg^{2+} and Ca^{2+} hydration. *J. Chem. Phys.* 1995, 103, (4), 1588-1598.

85. Smirnov, P. R.; Trostin, V. N., Structural parameters of hydration of Be^{2+} and Mg^{2+} ions in aqueous solutions of their salts. *Russ. J. Gen. Chem.* 2008, 78, (9), 1643-1649.

86. Cappa, C. D.; Smith, J. D.; Messer, B. M.; Cohen, R. C.; Saykally, R. J., Effects of cations on the hydrogen bond network of liquid water: new results from X-ray absorption spectroscopy of liquid microjets. *J. Phys. Chem. B* 2006, 110, (11), 5301-5309.

87. Lightstone, F. C.; Schwegler, E.; Hood, R. Q.; Gygi, F.; Galli, G., A first principles molecular dynamics simulation of the hydrated magnesium ion. *Chem. Phys. Lett.* 2001, 343, (5-6), 549-555.

88. Struis, R. P. W. J.; De Bleijser, J.; Leyte, J. C., Magnesium-25(2+) and chloride-35 quadrupolar relaxation in aqueous magnesium chloride solutions at 25ºC. 2. Relaxation at finite magnesium chloride concentrations. *J. of Phys. Chem.* 1989, 93, (23), 7943-7952.

89. Tongraar, A.; Rode, B. M., Structural arrangement and dynamics of the hydrated Mg^{2+}: an ab initio QM/MM molecular dynamics simulation. *Chem. Phys. Lett.* 2005, 409, 304-309.

90. Callahan, K. M.; Casillas-Ituarte, N. N.; Roeselová, M.; Allen, H. C.; Tobias, D. J., Solvation of magnesium dication: molecular dynamics simulation and vibrational spectroscopic study of magnesium chloride in aqueous solutions. *J. Phys. Chem. B in press* 2009.

91. Blanchard, D., The oceanic production of atmospheric sea salt. *J. Geophys. Res.* 1985, 90, (C1), 961-963.

92. Shaw, G., Aerosol chemical components in Alaska air masses 2. Sea salt and marine product. *J. Geophys. Res.* 1991, 96, (D12), 22369-22372.

93. Rosenfeld, D.; Dai, J.; Yu, X.; Yao, Z.; Xu, X.; Yang, X.; Du, C., Inverse relations between amounts of air pollution and orographic precipitation. *Science* 2007, 315, (5817), 1396-1398.

94. Rosenfeld, D.; Lohmann, U.; Raga, G. B.; O'Dowd, C. D.; Kulmala, M.; Fuzzi, S.; Reissell, A.; Andreae, M. O., Flood or drought: How do aerosols affect precipitation? *Science* 2008, 321, (5894), 1309-1313.

95. Lihavainen, H.; Kerminen, V. M.; Komppula, M.; Hyvarinen, A. P.; Laakia, J.; Saarikoski, S.; Makkonen, U.; Kivekas, N.; Hillamo, R.; Kulmala, M.; Viisanen, Y., Measurements of the relation between aerosol properties and microphysics and

chemistry of low level liquid water clouds in Northern Finland. *Atmos. Chem. Phys.* 2008, 8, (23), 6925-6938.

96. Carpenter, L. J., Iodine in the marine boundary layer. *Chem. Rev.* 2003, 103, 4953-4962.

97. Li, X.-H.; Wang, F.; Lu, P.-D.; Dong, J.-L.; Wang, L.-Y.; Zhang, Y.-H., Confocal Raman observation of the efflorescence/deliquescence processes of individual $NaNO_3$ particles on quartz. *J. Phys. Chem. B* 2006, 110, 24993-24998.

98. Xu, M.; Tang, C. Y.; Jubb, A. M.; Chen, X.; Allen, H. C., Nitrate anions and ion pairing at the air-aqueous interface. *J. Phys. Chem. C* 2009, 113, (6), 2082-2087.

99. Finlayson-Pitts, B. J., Chlorine atoms as a potential tropospheric oxidant in the marine boundary layer. *Res. Chem. Intermediat.* 1993, 19, (3), 235-249.

100. Auer, B. M.; Skinner, J. L., Water: Hydrogen bonding and vibrational spectroscopy, in the bulk liquid and the liquid/vapor interface. *Chem. Phys. Lett.* 2009, 470, 13-20.

101. Noah-Vanhoucke, J.; Smith, J. D.; Geissler, P. L., Statistical mechanics of sum frequency generation spectroscopy for the liquid-vapor interface of dilute aqueous salt solutions. *Chem. Phys. Lett.* 2009, 470, (1-3), 21-27.

102. Richmond, G. L., Molecular bonding and interactions at aqueous surfaces as probed by vibrational sum frequency spectroscopy. *Chem. Rev.* 2002, 102, (8), 2693-2724.

103. Shen, Y. R.; Ostroverkhov, V., Sum-frequency vibrational spectroscopy on water interfaces: polar orientation of water molecules at interfaces. *Chem. Rev.* 2006, 106, (4), 1140-1154.

104. Shultz, M. J.; Baldelli, S.; Schnitzer, C.; Simonelli, D., Aqueous solution/air interfaces probed with sum frequency generation spectroscopy. *J. Phys. Chem. B* 2002, 106, 5313-5324.

105. Smith, J. D.; Cappa, C. D.; Wilson, K. R.; Cohen, R. C.; Geissler, P. L.; Saykally, R. J., Unified description of temperature-dependent hydrogen-bond rearrangements in liquid water. *Proc. Natl. Acad. Sci.* 2005, 102, (40), 14171-14174.

106. Sovago, M.; Campen, R. K.; Wurpel, G. W. H.; Müller, M.; Bakker, H. J.; Bonn, M., Vibrational response of hydrogen-bonded interfacial water is dominated by intramolecular coupling. *Phys. Rev. Lett.* 2008, 100, (17), 173901(1)-(4).

107. Du, Q.; Superfine, R.; Freysz, E.; Shen, Y. R., Vibrational spectroscopy of water at the vapor/water interface. *Phys. Rev. Lett.* 1993, 70, (15), 2313-2316.

108. Ji, N.; Ostroverkhov, V.; Tian, C. S.; Shen, Y. R., Characterization of vibrational resonances of water-vapor interfaces by phase-sensitive sum-frequency spectroscopy. *Phys. Rev. Lett.* 2008, 100, 096102/1-096102/4.

109. Raymond, E. A.; Richmond, G. L., Probing the molecular structure and bonding of the surface of aqueous salt solutions. *J. Phys. Chem. B* 2004, 108, (16), 5051-5059.

110. Raymond, E. A.; Tarbuck, T. L.; Brown, M. G.; Richmond, G. L., Hydrogen-bonding interactions at the vapor/water interface investigated by vibrational sum-frequency spectroscopy of HOD/HO/DO mixtures and molecular dynamics simulations. *J. Phys. Chem. B* 2003, 107, 546-556.

111. Bush, M. F.; O'Brien, J. T.; Prell, J., S.; Wu, C.-C.; Saykally, R. J.; Williams, E. R., Hydrations of alkaline earth metal dications: Effects of metal ion size determined using infrared action spectroscopy. *JACS* 2009, 131, (37), 13270-13277.

112. Auer, B. M.; Skinner, J. L., IR and Raman spectra of liquid water: Theory and interpretation. *J. Chem. Phys.* 2008, 128, 224511(1)-(12).

113. Auer, B. M.; Skinner, J. L., Vibrational sum-frequency spectroscopy of the liquid/vapor interface for dilute HOD in D_2O. *J. Chem. Phys.* 2008, 129, 214705(1)-(14).

114. Corcelli, S. A.; Lawrence, C. P.; Skinner, J. L., Combined electronic structure/molecular dynamics approach for ultrafast infrared spectroscopy of dilute HOD in liquid H_2O and D_2O. *J. Chem. Phys.* 2004, 120, (17), 8107-8117.

115. Chaban, G. M.; Jung, J. O.; Gerber, R. B., Anharmonic vibrational spectroscopy of hydrogen-bonded systems directly computed from ab initio potential surfaces: $(H_2O)n$, n=2,3; $Cl^-(H_2O)n$, n=1,2; $H^+(H_2O)n$, n=1,2; H_2O-CH_3OH. *J. Phys. Chem. A* 2000, 104, 2772-2779.

116. Smith, J. D.; Saykally, R. J.; Geissler, P. L., The effects of dissolved halide anions on hydrogen bonding in liquid water. *J. Am. Chem. Soc.* 2007, 129, 13847-13856.

117. Gan, W.; Wu, D.; Zhang, Z.; Feng, R. R.; Wang, H. F., Polarization and experimental configuration analyses of sum frequency generation vibrational spectra, structure, and orientational motion of the air/water interface. *J. Chem. Phys.* 2006, 124, 114705(1)-(15).

118. Wei, X.; Shen, Y. R., Motional effect in surface sum-frequency vibrational spectroscopy. *Phys. Rev. Lett.* 2001, 86, 4799-4802.

119. Miller, D. J.; Lisy, J. M., Hydrated alkali-metal cations: Infrared spectroscopy and ab Initio calculations of $M^+(H_2O)_{x=2-5}Ar$ cluster ions for M = Li, Na, K, and Cs. *J. Am. Chem. Soc.* 2008, 130, 15381-15392.

120. Probst, M. M.; Hermansson, K., On frequency shifts in OH stretching vibrations of hydrated cations. *J. Chem. Phys.* 1991, 96, (12), 8995-9004.

121. Jungwirth, P.; Finlayson-Pitts, B. J.; Tobias, D. J., Introduction: structure and chemistry at aqueous interfaces. *Chem. Rev.* 2006, 106, (4), 1137-1139.

122. Minofar, B.; Vácha, R.; Wahab, A.; Mahiuddin, S.; Kunz, W.; Jungwirth, P., Propensity for the air/water interface and ion pairing in magnesium acetate vs magnesium nitrate solutions: Molecular dynamics simulations and surface tension measurements. *J. Phys. Chem. B* 2006, 110, (32), 15939-15944.

123. Burikov, S. A.; Dolenko, T. A.; Fadeev, V. V.; Vlasov, I. I., Revelation of ion hydration in Raman scattering spectral bands of water. *Laser Phys.* 2007, 17, (10), 1255-1261.

124. Burikov, S. A.; Dolenko, T. A.; Velikotnyi, P. A.; Sugonyaev, A. V.; Fadeev, V. V., The effect of hydration of ions of inorganic salts on the shape of the Raman stretching band of water. *Opt. Spectrosc.* 2005, 98, (2), 235-239.

125. Gopalakrishnan, S.; Jungwirth, P.; Tobias, D. J.; Allen, H. C., Air-liquid interfaces of aqueous solutions containing ammonium and sulfate: spectroscopic and molecular dynamics studies. *J. Phys. Chem. B* 2005, 109, (18), 8861-8872.

126. Terpstra, P.; Combes, D.; Zwick, A., Effects of salts on dynamics of water: a Raman spectroscopy study. *J. Chem. Phys.* 1990, 92, 65-70.

127. Xu, M.; Spinney, R.; Allen, H. C., Water structure at the air-aqueous interface of divalent cation and nitrate solutions. *J. Phys. Chem. B* 2008, 113, (13), 4102-4110.
128. Shultz, M. J.; Schnitzer, C.; Simonelli, D.; Baldelli, S., Sum frequency generation spectroscopy of the aqueous interface: ionic and soluble molecular solutions. *Int. Rev. Phys. Chem.* 2000, 19, (1), 123 - 153.
129. Xu, M.; Larentzos, J. P.; Roshdy, M.; Criscenti, L. J.; Allen, H. C., Aqueous divalent metal-nitrate interactions: hydration versus ion pairing. *Phys. Chem. Chem. Phys.* 2008, 10, (32), 4793-4801.
130. Wang, H.-F.; Gan, W.; Lu, R.; Rao, Y.; Wu, B.-H., Quantitative spectral and orientational analysis in surface sum frequency generation vibrational spectroscopy (SFG-VS). *Int. Rev. Phys. Chem.* 2005, 24, 191-256.
131. Zhuang, X.; Miranda, P. B.; Kim, D.; Shen, Y. R., Mapping molecular orienation and conformation at interfaces by surface nonlinear optics. *Phys. Rev. B* 1999, 59, (19), 12632-12640.
132. Krekeler, C.; Delle Site, L., Lone pair versus bonding pair electrons: the mechanism of electronic polarization of water in the presence of positive ions. *J. Chem. Phys.* 2008, 128, 134515.
133. Headrick, J. M.; Diken, E. G.; Walters, R. S.; Hammer, N. I.; Christie, R. A.; Cui, J.; Myshakin, E. M.; Duncan, M. A.; Johnson, M. A.; Jordan, K. D., Spectral signatures of hydrated proton vibrations in water clusters. *Science* 2005, 308, 1765-1769.
134. Buch, V.; Devlin, J. P., Spectra of dangling OH bonds in amrphous ice: assignment to 2- to 3-coordinated surface molecules. *J. Chem. Phys.* 1991, 94, (5), 4091-4092.
135. Herich, H.; Tritscher, T.; Wiacek, A.; Gysel, M.; Weingartner, E.; Lohmann, U.; Baltensperger, U.; Cziczo, D. J., Water uptake of clay and desert dust aerosol particles at sub- and supersaturated water vapor conditions. *Phys. Chem. and Chem. Phys.* 2009, 11, 7804-7809.
136. Bergna, H. E.; Roberts, W. O., *Colloidal silica: Fundamentals and applications*. CRC Taylor & Francis: Boca Raton, FL, 2006; Vol. 131, p 267.
137. Iler, R. K., *The chemistry of silica: solubility, polimerization, colloid and surface properties, and biochemistry*. John Wiley and Sons. Willey-Interscience Publication: New York, 1979.
138. Konek, C. T.; Musorrafiti, M. J.; Al-Abadleh, H. A.; Bertin, P. A.; Nguyen, S. T.; Geiger, F. M., Interfacial acidities, charge densities, potentials, and energies of carboxylic acid-functionalized silica/water interfaces determined by second harmonic generation. *J. Am. Chem. Soc.* 2004, 126, 11754-11755.
139. Mifflin, A. L.; Gerth, K. A.; Weiss, B. M.; Geiger, F. M., Surface studies of Chromate binding to fused quartz/water interfaces. *J. Phys. Chem. A* 2003, 6212-6217.
140. Ong, S.; Zhao, X.; Eisenthal, K. B., Polarization of water molecules at a charged interface: second hamonic studies of the silica/water interface. *Chem. Phys. Lett.* 1992, 191, (3-4), 327-335.
141. Zhao, X.; Ong, S.; Wang, H.-F.; Eisenthal, K. B., New method for determination of surface pKa using second harmonic generation. *Chem. Phys. Lett.* 1993, 214, 203-207.

142. Langmuir, D., *Aqueous Environmental Geochemistry*. 1st ed.; Pearson Education: Upper Saddle River, New Jersey, 1997.
143. Zhuravlev, L. T., The surface chemistry of amorphous silica. Zhuravlev model. *Colloids Surf. A* 2000, 173, 1-45.
144. Duval, Y.; Mielczarski, J. A.; Pokrovsky, O. S.; Mielczarski, E.; Ehrhardt, J. J., Evidence of the Existence of Three Types of Species at the Quartz-Aqueous Solution Interface at pH 0-10: XPS Surface Group Quantification and Surface Complexation Modeling. *J. Phys. Chem. B.* 2002, 106, (11), 2937-2945.
145. Sahai, N.; Sverjensky, D. A., Evaluation of internally consistent papramenters for the triple-layer model by the systematic analysis of oxide surface titration data. *Geochim. Cosmochin. Acta* 1997, 61, (14), 2801-2826.
146. Stumm, W.; Morgan, J. J., *Aquatic Chemistry: An introduction emphasizing chemical equilibria in natural waters* 3rd ed.; John Wiley and Sons: New York, 1981.
147. McDonald, R. S., Study of the interaction between hydroxyl groups of aerosil silica and adsorbed nonpolar molecules by infrared spectrometry. *J. Am. Chem. Soc.* 1957, 79, 850-854.
148. Lygin, V. I., IR-spectroscopy study of changes in silica surface structure on thermal dehydroxylation and rehydroxilation in water vapors. *Russ. J. Gen. Chem.* 2001, 71, 1368-1372.
149. Vigil, G.; Xu, Z.; Steinberg, S.; Israelachvili, J., Interaction of silica surfaces. *J. Colloid Interface Sci.* 1994, 165, 367-385.
150. Levering, L. M.; Sierra-Hernandez, M. R.; Allen, H. C., Observation of hydronium ions at the air-aqueous acid interface: vibrational spectroscopic studies of aqueous HCl, HBr, and HI. *J. Phys. Chem. C* 2007, 111, (25), 8814-8826.
151. Asay, D. B.; Kim, S. H., Evolution of the adsorbed water layer structure on silicon dioxide at room temperature. *J. Phys. Chem. B.* 2005, 109, 16760-16763.
152. Bogdan, A.; Kulmala, M., Effects of acids on water vapor uptake by pyrogenic silica. *J. Colloid Interface Sci.* 1997, 191, 95-101.
153. Klier, K.; Shen, J. H.; Zettlemoyer, A. C., Water on silica and silicates surfaces. I. Partially hyhdrophobic silicas. *J. Phys. Chem.* 1973, 77, 1458-1465.
154. Wendt, S.; Frerichs, M.; Wei, T.; Chen, M. S.; Kempter, V.; Goodman, D. W., The interaction of water with silica thin films grown on Mo(112). *Surf. Sci.* 2004, 107-120.
155. Hirose, C.; Akamatsu, N.; Domen, K., Formulas for the analysis of the surface SFG spectrum and transformation coefficients of cartesian SFG components. *Appl. Spectrosc.* 1992, 42, (6), 1051-1072.
156. Sindorf, D. W.; Maciel, G. E., Silicon-29 NMR study of dehydrated/rehydrated silica gel using cross polarization and magic angle spinning. *J. Am. Chem. Soc.* 1983, 105, (6), 1487-1493.
157. Morrow, B. A.; McFarlan, A. J., Infrared and gravimetric study of Aerosil and a precipitated silica using chemical and H/D exchange probes. *Langmuir* 1991, 7, 1695-1701.

158. Tyrode, E.; Johnson, M.; Baldelli, S.; Leygraf, C.; Rutland, M. W., A vibrational sum frequency spectroscopy study of the liquid-gas interface of acetic acid-water mixtures: 2. Orientation analysis. *J. Phys. Chem. B* 2005, 109, 329-341.

159. Gennis, R. B., *Biomembranes*. Springer: New York, 1989.

160. Knepp, V.; Guy, R. H., Transport of steroids at model biomembrane surfaces and across organic liquid-aqueous phase interfaces. *J. Phys. Chem. B* 1989, 93, 6817-6823.

161. Alberts, B.; Johnson, A.; Lewis, J.; Roberts, K.; P., W., *Molecular biology of the cell*. Garland Science: New York, 2002.

162. Szule, J. A.; Jarvis, S. E.; Hibbert, J. E.; Spafford, J. D.; Braun, J. E. A.; Zamponni, G. W.; Wessel, G. M.; R., C. J., Calcium-triggered membrane fusion proceeds independently of specific presynaptic proteins. *J. Biol. Chem.* 2003, 278, 24251-24254.

163. Altenbach, C.; Seelig, J., Ca^{2+} binding to phosphatidylcholine bilayers as studied by Deuterium magnetic resonance. Evidence for the formation of a Ca^{2+} complex with two phospholipid molecules. *Biochem.* 1984, 23, 3913-3920.

164. Binder, H.; Zschörnig, O., The effect of metal cations on the phase behavior and hydration characteristics of phospholipid membranes. *Chem. Phys. Lipids.* 2002, 115, 39-61.

165. Herbette, L.; Napolitano, C. A.; McDaniel, R. V., Direct determination of the calcium profile structure for dipalmitoyllecithin multilayers using neutron diffraction. *Biophys. J.* 1984, 46, 677-685.

166. Lopez, C. F.; Nielsen, S. O.; Klein, M. L.; Moore, P. B., Hydrogen bonding structure and dynamics of water at the dimyristoylphosphatidylcholine lipid bilayer surface from a molecular dynamics simulation. *J. Phys. Chem. B* 2004, 108, 6603-6610.

167. Vernier, P. T.; Ziegler, M. J.; Dimova, R., Calcium-binding and head group dipole angle in phosphatidylserine-phosphatidylcholinebilayers. *Langmuir* 2009, 25, 1020-1027.

168. McLaughlin, S.; Mulrine, N.; Gresalfi, T.; Vaio, G.; McLaughlin, A., Adsorption of divalent cations to bilayer membranes containing phosphatidylserine. *J. Gen. Physiol.* 1981, 77, 445-473.

169. Seelig, J., Interaction of phospholipids with Ca^{2+} ions. On the role of the phospholipid head groups. *Cell. Biol. Int. Rep.* 1990, 14, 353-360.

170. Akutsu, H.; Seelig, J., Interaction of metal ions with phosphatidylcholine bilayer membranes. *Biochem.* 1981, 20, 7366-7373.

171. Seelig, J.; Macdonald, P. M.; Scherer, P. G., Phospholipid head group as sensors of electric charge in membranes. *Biochem.* 1987, 26, 7535-7541.

172. Böckmann, R. A.; Hac, A.; Heimburg, T.; Grubmüller, H., Effect of sodium chloride on a lipid bilayer. *Biophys. J.* 2003, 85, 1647-1655.

173. Berkowitz, M. L.; Bostick, D. L.; Pandit, S., Aqueous solutions next to phospholipid membrane surfaces: insights from simulations. *Chem. Rev.* 2006, 106, 1527-1539.

174. Pandit, S. A.; Bostick, D.; Berkowitz, M. L., Molecular dynamics simulation of a Dipalmitoylphosphatidylcholine bilayer with NaCl. *Biophys. J.* 2003, 84, 3743-3750.

175. Pandit, S. A.; Bostick, D.; Berkowitz, M. L., Mixed bilayer containing dipalmitoylphosphatidylcholine and dipalmitoylphosphatidylserine: lipid complexation, ion binding, and electrostatics. *Biophys. J.* 2003, 85, 3120-3131.
176. Sachs, J. N.; Nanda, H.; Petrache, H. I.; Woolf, T. B., Changes in phosphatidylcholine headgroup tilt and water order induced by monovalent salts: molecular dynamics simulations. *Biophys. J.* 2004, 86, 3772-3782.
177. Cevc, G., *Phospholipids handbook*. Marcel Dekker, Inc: New York, 1993.
178. Mattai, J.; Hauser, H.; Demel, R. A.; Shipley, G. G., Interactions of metal ions with phosphatidylserine bilayer membranes: effect of hydrocarbon chain unsaturation. *Biochem.* 1989, 2322-2330.
179. Uhríková, D.; Kucerka, N.; Teixeira, J.; Gordeliy, V.; Balgavy, P., Structural changes in dipalmitoylphosphatidylcholine bilayer promoted by Ca^{2+} ions: a small angle neutron scattering study. *Chem. Phys. Lipids* 2008, 155, 80-89.
180. Zhang, X.; Borda, M. J.; Schiinen, M. A. A.; Strongin, D. R., Adsorption of phospholipids on pyrite and their effect on surface oxidation. *Langmuir* 2003, 19, 8787-8792.
181. Lin, K.-C.; Weis, R. M.; McConnell, H. M., Induction of helical liposomes by Ca2+ mediated intermembrane binding. *Nature* 1982, 296, 164-165.
182. Murashov, V. V.; Harper, M.; Demchuk, E., Impact of silanol surface density on the toxicity of silica aerosols measured by erythrocyte haemolysis. *J. Occ. Environ. Hyg* 2006, 3, 718-723.
183. Nash, T.; Allison, A. C.; Harington, J. S., Physico-chemical properties of silica in relation to its toxicity. *Nature* 1966, 210, 259-261.
184. Creuwels, L. A. J. M.; van Golde, L. M. G.; Haagsman, H. P., The pulmonary surfactant system: biochemical and clinical aspects. *Lung* 1997, 175, 1-39.
185. Stevens, M. J.; Donato, L. J.; Lower, S. K.; Sahai, N., Oxide-dependent adhesion of the jurkat Line of T Lymphocytes *Langmuir* 2009, 25, (11), 6270-6278.
186. Gaines, G. L., *Insoluble monolayers at lliquid-gas interfaces*. Interscience: New York, 1966.
187. Aroti, A.; Leontidis, E.; Maltseva, E.; G., B., Effect of Hofmeister anions on DPPC Langmiur monolayers at the air-water interface. *J. Phys. Chem. B* 2004, 108, 15238-15245.
188. Sovago, M.; Wurpel, G. H.; Smits, M.; Mller, M.; Bonn, M., Calcium-induced phospholipid ordering depends on surface pressure. *J. Am. Chem. Soc* 2007, 129, 11079-11084.
189. Leontidis, E.; Aroti, A., Liquid expanded monolayers of lipids as model systems to understand the anionic Hofmeister series:2. ion partitioning is mostly a matter of size. *J. Phys. Chem. B* 2009, 113, 1460-1467.
190. Böckmann, R. A.; Grubmüller, H., Multistep binding of divalent cations to phospholipid bilayers: a molecular dynamics study. *Angew. Chem. Int. Ed.* 2004, 43, 1021-1024.
191. Marcus, Y., Thermodynamics of solvation of ions. Part 5. Gibbs free energy of hydration at 298.15. *J. Chem. Soc. Faraday Trans.* 1991, 87, 2995-2999.

192. Jacobs, R. E.; White, S. H., The nature of the hydrophobic binding of small peptides at the bilayer interface: Implications for the insertion of transbilayer helices. *Biochem.* 1989, 28, 3421-3437.
193. Merz, K. M. J.; Roux, B., *Biological membranes: a molecular perspective from computation and experiment*. Birkhauser: Boston, 1996.
194. Zhou, Z.; Sayer, B. G.; Hughes, D. W.; Stark, R. E.; Epand, R. M., Studies of phospholipid hydration by high-resolution magic angle spinning nuclear magnetic resonance. *Biophys. J.* 1999, 76, 387-399.
195. Volkov, V. V.; Takaoka, Y.; Righini, R., What are the sites water occupies at the interface of a phospholipid membrane. *J. Phys. Chem. B* 2009, 113, 4119-4124.
196. Yin, J.; Zhao, Y.-P., Hydrid QM/MM simulation of the hydration phenomena of dipalmitoylphosphatidylcholine headgroup. *J. Colloid Interface Sci.* 2009, 329, 410-415.
197. Zhao, W.; Moilanen, D. E.; Fenn, E. E.; Fayer, M. D., Water at the surfaces of aligned phospholipid multibilayer model membranes probed with ultrafast vibrational spectroscopy. *J. Am. Chem. Soc* 2008, 130, 13927-13937.
198. Casal, H. L.; Mantsch, H. H.; Paltauf, F.; Hauser, H., Infrared and 31P-NMR studies of the effect if Li^+ and Ca^{2+} on phosphatidylserines. *Biochim. Biophys. Acta* 1987, 919, 275-286.
199. Hübner, W.; Mantsch, H. H., Orientation of specifically $^{13}C=O$ labeled phosphatidylcholine multilayers from polarized attenuated total reflection FT-IR spectroscopy. *Biophys. J.* 1991, 59, 1261-1272.
200. Arrondo, J. L. R.; Goñi, F. M.; Macarulla, J. M., Infrared spectroscopy of phosphatidylcholines in aqueous suspension a study of the phosphate group vibrations. *Biochim. Biophys. Acta* 1984, 794, 165-168.
201. Binder, H.; Anikin, A.; Kohlstrunk, B.; Klose, G., Hydration-induced gel stated of dienic lipid 1,2-bis(2,4-octadecadienoyl)-sn-glycero-3-phosphorylcholine and their characterization using infrared spectroscopy. *J. Phys. Chem. B* 1997, 101, 6618-6628.
202. Gauger, D. R.; Selle, C.; Fritzsche, H.; Pohle, W., Chain-length dependence of the hydration properties of saturated phosphatidylcholines as revealed by FTIR spectroscopy. *J. Mol. Struct.* 2001, 565/566, 25-29.
203. Pohle, W.; Selle, C.; Fritzsche, H.; Bohl, M., Comparative FTIR spectroscopic study upon the hydration of lecithins and cephalins. *J. Mol. Struct.* 1997, 408/409, 273-277.
204. Mrázková, E.; Hobza, P.; Bohl, M.; Gauger, D. R.; Pohle, W., Hydration-induced changes of structure and vibrational frequencies of methylphosphocholine studied as a model of biomembrane lipids. *J. Phys. Chem. B* 2005, 109, 15126-15134.
205. Essmann, U.; Berkowitz, M., Dynamical properties of phospholipid bilayers from computer simulation. *Biophys. J.* 1999, 76, 2081-2089.
206. Satoh, K., Determination of binding constants of Ca^{2+}, Na^+, and Cl^- ions to liposomal membranes of dipalmitoylphosphatidylcholine at gel phase by particle electrophoresis. *Biochim. Biophys. Acta* 1995, 1239, 239-248.
207. Tatulian, S. A., Binding of alkaline-earth metal cations and some anions to phosphatidylcholine liposomes. *Eur. J. Biochem.* 1987, 170, 413-420.

208. Marra, J.; Israelachvili, J., Direct measurement of forces between phosphatidylcholine and phosphatidylethanolamine bilayers in aqueous electrolyte solutions. *Biochem.* 1985, 24, 4608-4618.

209. Petrov, A. S.; Funseth-Smotzer, J.; Pack, G. R., Computational study of dimethyl phosphate anion and its complexes with water, magnesium and calcium. *Int. J. Quant. Chem.* 2004, 102, 645-655.

210. Schneider, B.; Kabelác, M.; Hobza, P., Geometry of the phosphate group and its interactions with metal cations in crystals and *ab initio* calculations. *J. Am. Chem. Soc* 1996, 1996, 12207-12217.

211. Brumm, T.; Naumann, C.; Sackmann, E.; Rennie, A. R.; Thomas, R. K.; Kanellas, D.; Penfold, J.; Bayerl, T. M., Conformational changes of the lecithin headgroup in monolayers at the air/water interface. *Eur. Biophys. J.* 1994, 23, 289-295.

212. Dominguez, H.; Smondyrev, A. M.; Berkowitz, M. L., Computer simulations of phosphatidylcholine monolayers at air/water and CCl_4/water interfaces. *J. Phys. Chem. B.* 1999, 103, 9582-9588.

213. Griffin, R. G.; Powers, L.; Pershan, P. S., Head-group conformation in phospholipids: A phosphorus-31 nuclear magnetic resonance study of oriented monodomain dipalmitoylphosphatidylcholine bilayers. *Biochem.* 1978, 17, 2718-2722.

214. Högberg, C.-J.; Lyubartsev, A. P., Effect of local anesthetic Lidocaine on electrostatic properties of a lipid bilayer. *Biophys. J.* 2008, 94, 525-531.

215. Smondyrev, A. M.; Berkowitz, M. l., Phospholipid membranes: constant pressure molecular dynamics simulations of dipalmitoylphosphatidicholine/water system. *J. Comput. Chem.* 1999, 20, 531-545.

216. Vácha, R.; Siu, S. W. I.; Petrov, M.; Böckmann, R. A.; Barucha-Kraszewska, J.; Jurkiewicz, P.; Hof, M.; Berkowitz, M. L.; Jungwirth, P., Effects of alkali cations and halide anions on the DOPC lipid membrane. *J. Phys. Chem. A* 2009, 113, 7235-7243.

217. Guan, Y.; Wurrey, C. j.; Thomas, G. J., Vibrational analysis of nucleic acids. I. The phosphodiester group in dimethyl phosphate model compounds: $(CH_3O)_2PO_2^-$, $(CD_3O)_2PO_2^-$, and $(^{13}CH_3O)_2PO_2^{-*}$. *Biophys. J.* 1994, 66, 225-235.

218. Tu, K.; Tobias, D. J.; Blasie, J. K.; Klein, M. L., Molecular dynamics investigation of the structure of a fully hydrated gel-phase Dipalmitoylphosphatidylcholine bilayer. *Biophys. J.* 1996, 70, 595-608.

219. Liu, J.; Conboy, J. C., Structure of a gel phase lipid bilayers prepared by the Langmuir-Blodgett/Langmuir-Schaefer method characterized by sum-frequency vibrational spectroscopy. *Langmuir* 2005, 21, 9091-9097.

220. Cordomí, A.; Edholm, O.; Perez, J. J., Effect of ions on a dipalmitoylphosphatidylcholine bilayer. A molecular dynamics simulation study. *J. Phys. Chem. B.* 2008, 112, 1397-1408.

221. Bickmore, B.; Tadanier, C. J.; Rosso, K. M.; Monn, W. D.; Eggett, D. L., Bond-Valence methods for pKa prediction: critical reanalysis and a new approach. *Geochim. Cosmochi. Acta.* 2004, 68, (9), 2025-2042.

222. Chunbo, Y.; Daqing, Z.; Aizhuo, L.; Jiazuan, N., A NMR study of the interaction of silica with dipalmitoylphosphatidylcholine liposomes. *J. Colloid Interface Sci.* 1995, 172, 536-538.

223. Johnson, S. A.; Bayerl, T. M.; McDermott, D. C.; Adam, G. W.; Rennie, A. R.; Thomas, R. K.; Sackmann, E., Structure of an adsorbed dimyristoylphosphatidylcholine bilayer measured with specular reflection of neutrons. *Biophys. J.* 1991, 59, 289-294.
224. Tamm, L. K.; McConnell, H. M., Supported phospholipid bilayers. *Biophys. J.* 1985, 47, 105-113.
225. Castellana, E. T.; Cremer, P. S., Solid supported lipid bilayers: from biophysical studies to sensor design. *Surf. Sci. Rep.* 2006, 61, 429-444.
226. Casillas-Ituarte, N. N.; Allen, H. C., Water, chloroform, acetonitrile, and atrazine adsorption to the amorphous silica surface studied by vibrational sum frequency generation spectroscopy. *Chem. Phys. Lett.* 2009, 483, 84-89.
227. Naumann, C.; Brumm, T.; Bayerl, T. M., Phase transition behavior of single phosphatidylcholine bilayers on a solid spherical support studied by DSC, NMR, and FT-IR. *Biophys. J.* 1992, 63, 1314-1319.
228. Oleson, T. A.; Sahai, N., Oxide-dependent adsorption of a model membrane phospholipid, Dipalmitoylphosphatidylcholine: bulk adsorption isotherms. *Langmuir* 2008, 24, 4865-4873.
229. Xu, J.; Stevens, M. J.; Oleson, T. A.; Last, J. A.; Sahai, N., Role of oxide surface chemistry and phospholipid phase on adsorption and self-assembly: Isotherms and atomic force microscopy. *J. Phys. Chem. C* 2009, 113, 2187-2196.
230. Murray, D. K.; Harrrison, J. C.; E., W. W., A ^{13}C CP/MAS and ^{31} P NMR study of the interactions of dipalmitoylphosphatidylcholine with respirable silica and kaolin. *J. Colloid Interface Sci.* 2005, 288, 166-170.
231. Sahai, N.; Sverjensky, D. A., Solvation and electrostatic model for specific electrolyte adsorption. *Geochim. Cosmochi. Acta.* 1997, 61, 2827-2848.
232. Dove, P. M.; Craven, C. M., Surface charge density on silica in alkali and alkaline earth chloride electrolyte solutions. *Geochim. Cosmochi. Acta.* 2005, 69, 4963-4970.
233. Jena, K. C.; K., H. D., Variation of ionic strength reveals the interfacial water structure at a charged mineral surface. *J. Phys. Chem. C* 2009, 113, 15364-15372.
234. Yang, Z.; Li, Q.; Chou, K. C., Structure of water molecules at the interfaces of aqueous salt solutions and silica: cation effects. *J. Phys. Chem. C* 2009, 113, 8201-8205.
235. Karlsson, M.; Craven, C.; Dove, P. M.; Casey, W. H., Surface charge concentrations on silica in different 1.0 M metal-chloriden background electrolytes and implications for dissolution rates. *Aquat. Geochem.* 2001, 7, 13-32.
236. Palik, E. D., *Handbook of optical constants of solids*. Elsevier: 1998.
237. Murashov, V. V.; Leszczynski, J., Adsorption of the phosphate groups on silica hydroxyls; an ab initio study. *J. Phys. Chem. A* 1999, 103, 1228-1238.
238. Hetzer, M.; Heinz, S.; Grage, S.; Bayerl, T. M., Asymmetric molecular friction in supported phospholipid bilayers revealed by NMR measurements of lipid diffusion. *Langmuir* 1998, 14, 982-984.
239. Graedel, T. E.; Keene, W. C., Tropospheric budget of reactive chlorine. *Global Biogeochem. Cy.* 1995, 9, (1), 47-77.
240. Yokouchi, Y.; Ikeda, M.; Inuzuka, Y.; Yukawa, T., Strong emission of methyl chloride from tropical plants. *Nature (London)* 2002, 416, (6877), 163-165.

241. Rhew, R. C.; Miller, B. R.; Weiss, R. F., Natural methyl bromide and methyl chloride emissions from coastal salt marshes. *Nature (London)* 2000, 403, (6767), 292-295.

242. Lobert, J. M.; Keene, W. C.; Logan, J. A.; Yevich, R., Global chlorine emissions from biomass burning: Reactive Chlorine Emissions Inventory. *J. Geophys. Res., [Atmos.]* 1999, 104, (D7), 8373-8389.

243. Rasmussen, R. A.; Rasmussen, L. E.; Khalil, M. A. K.; Dalluge, R. W., Concentration distribution of methyl chloride in the atmosphere. *J. Geophys. Res., C: Oc. Atmos.* 1980, 85, (C12), 7350-7356.

244. Kerminen, V.-M.; Anttila, T.; Lehtinen, K.; Kulmala, M., Parameterization for atmospheric new-particle formation: Application to a system involving sulfuric acid and condensable water-soluble organic vapors. *Aerosol Sci. Tech.* 2004, 38, 1001-1008.

245. Harper, K.; Minofar, B.; Sierra-Hernandez, M. R.; Casillas-Ituarte, N. N.; Roeselová, M.; Allen, H. C., Surface residence and uptake of methyl chloride and methyl alcohol at the air/water interface studied by vibrational sum frequency generation spectroscopy and molecular dynamics. *J. Phys. Chem. A* 2009, 113, (10), 2015-2024.

246. Harper, K. Interfacial vibrational chemistry of I. Mixed surfactant systems and II. Alkyl halide uptake and atmospheric implications. The Ohio State University, Columbus, 2007.

247. Sierra-Hernández, M. R. The Ohio State University, Columbus, 2010.

248. Stewart, E.; Shields, R. L.; Taylor, R. S., Molecular Dynamics Simulations of the Liquid/Vapor Interface of Aqueous Ethanol Solutions as a Function of Concentration. *J. Phys. Chem. B* 2003, 107, (10), 2333-2343.

249. Tarek, M.; Tobias, D. J.; Klein, M. L., Molecular dynamics investigation of an ethanol-water solution. *Physica A: Statistical and Theoretical Physics* 1996, 231, (1-3), 117-122.

250. Taylor, R. S.; Ray, D.; Garrett, B. C., Understanding the mechanism for the mass accommodation of ethanol by a water droplet. *J. Phys. Chem. B* 1997, 101, (28), 5473-5476.

251. Ma, G.; Allen, H. C., Surface Studies of Aqueous Methanol Solutions by Vibrational Broad Bandwidth Sum Frequency Generation Spectroscopy. *J. Phys. Chem. B* 2003, 107, (26), 6343-6349.

252. Van Loon, L. L.; Minor, R. N.; Allen, H. C., Structure og butanol and hexanol at aqueous, ammonium bisulfate, and sulfuric acid solution surfaces investigated by vibrational sum frequency generation spectroscopy. *J. Phys. Chem. A* 2007, 111, 7338-7346.

253. Socrates, G., *Infrared and Raman Characteristic Group Frequencies-Tables and Charts*. 3rd ed.; John Wiley & Sons: New York, NY, 2001.

254. Lide, D. R., *Physical Constants of Organic Compounds*. 87th ed.; Taylor and Francis: Boca Raton, FL, 2007.

255. Jayne, J. T.; Duan, S. X.; Davidovits, P.; Worsnop, D. R.; Zahniser, M. S.; Kolb, C. E., Uptake of gas-phase alcohol and organic acid molecules by water surfaces. *J. Phys. Chem.* 1991, 95, (16), 6329-6336.

256. Max, J. J.; Blois de, S.; Veilleux, A.; Chapados, C., IR spectroscopy of aqueous alkali halides. Factor analysis. *Can. J. Chem.* 2001, 79, 13-21.
257. Max, J. J.; Chapados, C., Interpolation and extrapolation of infrared spectra of binary ionic aqueous solutions. *Appl. Spectrosc.* 1999, 53, (12), 1601-1609.
258. Max, J. J.; Chapados, C., Influence of anomalous dispersion on the ATR spectra of aqueous solutions. *Appl. Spectrosc.* 1999, 53, (9), 1045-1053.
259. Lu, R.; Gan, W.; Wu, B.; Chen, H.; Wang, H.-F., Vibrational polarization spectroscopy of CH stretching modes of the Methylene group at the vapor/liquid interfaces with Sum Frequency Generation. *J. Phys. Chem. B.* 2004, 108, 7297.